Connections between structure and dynamics in model supercooled liquids

Glen M. Hocky

Submitted in partial fulfillment of the
requirements for the degree of
Doctor of Philosophy
under the Executive Committee
of the Graduate School of Arts and Sciences

COLUMBIA UNIVERSITY

2014

ABSTRACT

Connections between structure and dynamics in model supercooled liquids

Glen M. Hocky

In this thesis, we examine the relationship between structure and dynamics in supercooled liquids from five unique perspectives. We first study a static length scale in the liquid and compare its growth on decreasing temperature with the growth of the logarithm of relaxation times, and find them to be almost strongly correlated. We find that this length scale can distinguish between several specially chosen model liquids whose structure at the level of two-body correlations are identical but whose dynamics at a given temperature are quite different. We then study the number of normal modes necessary to capture the rearrangements in a two-dimensional supercooled liquid as it moves between inherent structures. We find that the number of modes is quite small and decreases as the system is further cooled. After that, we study the effect of a frozen amorphous boundary on the dynamics of supercooled liquids and find that the range of the effect plateaus near that system's mode coupling temperature. We also identify a dynamical crossover at a higher temperature from these data by contrasting the relaxation behavior in the directions perpendicular and parallel to the boundary. After this work, we compare particle mobility with the position of particles deemed to be in preferred local packing arrangements. We find that the correlation between slow dynamics and the location of these locally preferred structures is highly dependent on the model investigated. Finally, we study supercooled liquids that have a fraction of particles randomly fixed in equilibrium positions. We find from annealing and rapid heating experiments on these samples behavior reminiscent of experimentally produced ultrastable glasses.

Table of Contents

List of Figures

List of Tables

Acknowledgments

First and foremost I would like to thank my family, especially my parents, grandparents, and brother. I've had nothing but unconditional support and encouragement from them for all of my academic choices and none of this would have been possible without them. There is no one else to whom I would consider dedicating this thesis.

David Reichman has been a stellar advisor. Dave is better than anyone at making connections between disparate areas within a field or even spanning wide disciplines to surface deep interesting problems for us. Always available for advice, you also gave me freedom to follow problems in any direction and to seek out help and collaborations on my own. Your high standards ensured that all of the work in this thesis is of top quality, and presented in a clear and concise way. I have no doubt that your scientific style will have a great influence on the way that I will choose and attack problems for the rest of my career.

I would like to thank the rest of my thesis committee: Bruce J. Berne, Angelo Cacciuto, Laura J. Kaufman, and Andrea Cavagna. I feel uniquely lucky to have benefited greatly from all of the members of my committee during the course of my time at Columbia. Bruce was an excellent teacher of statistical mechanics and I think you made accessible topics that are at the same time, extremely important, difficult to teach, and not often covered. All the physical chemistry students in the department are very fortunate to have that resource. I have learned greatly from each of our subsequent conversations. Angelo has always been open with his enthusiasm for soft matter research and for espresso, and I have many fond memories of spending time down in his basement lair. Laura has always been a good friend in the department and I was fortunate to spend one semester working directly with you as a teaching assistant. I always knew if I needed anything that you were there just one flight up. Finally, Andrea has had a great impact on my Ph.D., as it was his work that directly

inspired my first real project in graduate school. He visited New York when I was starting out and helped shape my understanding of the problem. He then was generous enough to host me in Rome during my second year, which is certainly one of my most memorable times in graduate school. I am fortunate that you were visiting CUNY this semester and agreed to serve as my external committee member. I cannot think of a more fitting and symbolic way to close this chapter of my academic life.

I would never have reached this point without a long line of fortuitous academic experiences. I would almost certainly not been a chemist and perhaps not a scientist without the 10th grade and AP Chemistry class of Lawrence McAfoos who made chemistry exciting for (almost) everyone. I am especially grateful to Aaron Dinner for teaching some real stat mech and thermodynamics in honors general chemistry. I also benefited greatly from his graduate thermodynamics class, as well as his advice about choosing graduate schools, which eventually led to my coming to Columbia to work with Dave. I look forward to our work together next year. Laurie Butler secured from the Dreyfus foundation funding for a dozen or so chemistry undergraduates to perform two summers of summer research starting after first year. The offer to stay and do research probably more than anything put me irreversibly on the path to where I am today. It was my outstanding TAs Eugene and Eugene, both quantum chemists, who suggested I work with Karl Freed which is some of the best advice I have ever received.

I can't thank Karl enough for being an outstanding research mentor and really treating me as another member of the group, well before I'd studied physical chemistry. A short time later, I also began working with Tobin Sosnick, who also was eager to take input from anyone. Tobin's enthusiasm for all of his work was infectious. The combination of Tobin and Karl was perfect, and I never thought twice about spending almost all of my free time in the lab. My experience would have been nothing, however, without the other members of both groups who were all amazing people and from whom I learned so much. My first real project was done with Haipeng Gong and I certainly learned a lot on that project about being careful and precise. I would also like to thank in particular James Fitzgerald and

Aashish Adhikari for advice and friendship throughout the years. Andrés Colubri taught me quite a lot about being a scientific programmer and having fun as a post doc (which I'll be putting to good use soon). I cannot move on without highlighting my research mentors and close friends Abhishek Jha and Joseph DeBartolo. They were both, in their own ways, perfect examples of how to be successful graduate students, balancing friends and family with hard work and long hours when needed. Their inclusion of me in their activities as if I were another graduate student in the group (and not just a pipsqueak) set the tone for how I think all research groups should run.

I must give especially large gratitude to my Montpellier collaborators, Ludovic Berthier, Daniele Coslovich, and Walter Kob. The majority of the research in this thesis was performed directly with them. There is no substitute for having experts of that caliber telling you what you are doing wrong (and occasionally right)! They also very generously played host during my two week-long visits to Montpellier, during which each day I worked very hard and then ate very well. I certainly hope I can make an excuse to visit again. I would also like to thank the postdocs and students there for spending time with me, especially Atsushi Ikeda with whom I was also fortunate to do some research.

I must also thank Giulio Biroli for deep advice on all of the work in this thesis, and for spending some time in collaboration on each of his visits to New York. Perhaps one day I will finally finish one of our projects! I would also like to acknowledge the many other experts in the field with whom I discussed some of this work and who have greatly added to my understanding. These include especially Mark Ediger, Robert L. Jack, and Grzegorz Szamel. I have also enjoyed my continued collaboration and discussions with Mike Wilde throughout my Ph.D. and I look forward to that continuing next year and beyond.

My work was funded throughout by an NSF Graduate Research Fellowship. This was very significant both for allowing me to work in the Reichman group unconstrained but also because the previous inclusion of a one-time international travel stipend provided the impetus for my initial Montpellier collaboration and funded in part my first travel there and to La Sapienza in Rome. I do hope that the NSF (and other agencies) continue to generously

support graduate student research, as I have seen how big of an impact it has had for my research and for that of many of my friends.

Speaking of friends, I have built up so many wonderful relationships over the last few years and I think the worst part of graduate school is saying goodbye as we all go our separate directions.

The Reichman group has been a wonderful place to do research over the last five years. Everyone's diverse experiences and research interests have made for a fruitful and stimulating place to learn and work. I would like to thank everyone in the group, especially Richard and Brenda for welcoming new people into the group and advice on Columbia and getting started in graduate school.

I have also benefited from the friendship and advice of many postdoctoral scholars in the department. First, I would like to thank Tom Markland for his working with me on my first project. In addition to mentorship and advice, he has also served as a wonderful host during several trips to California. Additionally, I must highlight Kateri DuBay, Liesbeth Janssen, Joseph Morrone, Razvan Nistor, and Guillaume Stirnemann.

My time in graduate school would have been completely different without Tim as a labmate. I can't think of many other people with whom I'd be happy to spend 40-80 hours a week in the office, and then go hang out with afterwards. During our five years it seems Tim did at least twice as much research and learned three times as much as I did, and that will serve forever as a lesson in the power of combining really hard work and dedication with being really awesome. He also served as an outstanding arbiter of taste in figures and presentations, so please enjoy his many aesthetic suggestions throughout the figures in this thesis.

The other members of my cohort have been outstanding friends and colleagues. I've had uncountably many awesome experiences throughout the city and right here in Morningside Heights, most especially with Nick, Jeff, Neena, and Lindsay. I have always had a blast throughout with Sy, from when we were first here doing homework late into the night until this year when we got a chance to work together. Work here would have been much less

pleasant without frequent hallway chats with Nate, and I already miss our our occasional bouts of catch. The older students in the department made Columbia chemistry the kind of place we wanted to be for five years. This especially goes for my good friends (and former social chairs) Anđela and Dani. I like to think we carried on their legacy, and evidence for that is in all of the great friends I have made of the people that have come to Columbia since I got started, including especially Allison, Mark, Colin, Colleen, Nathan, Clarion, Dat, Joseph, and Stewart.

When people ask me for advice about graduate school, I often say that I was fortunate to have several good friends outside of the department. This gave me frequent excuse to get out of the Columbia bubble and see other parts of the city. I have to thank especially Adam for being a great friend throughout, with whom I once visited all five boroughs in one day, had many culinary adventures, and attended many baseball games. I would also like to thank Katie and Jonah for sharing in many other fun evening and weekend excursions. I also want to thank Elan, one of my oldest friends, who is certainly going to be a much better doctor than I will.

I had many great friends prior to graduate school. In particular I want to thank Ben, Matthew, Alex, Rachel, and Kailing for coming to visit me here, but more importantly for frequently letting me crash on your couch whenever I wanted to visit.

Some of those visits were for conferences, and I would be remiss if I did not thank some of my friends who I've met and spent time with because of science, including Shakeel, James, Todd, Elijah, Aaron, Katie, David, Pat, Dayton, Suri, and Asaph.

Finally, I would like to thank Martha for sharing these last five years with me, especially for your patience and understanding with being a plane ride apart. I can't imagine what my time in graduate school would have been like without the anticipation and great joy of our trips back and forth, as well as to other remote places for holidays, weddings, and vacations. I would also like to thank your family for welcoming me to your home and for celebrations, as well as for their understanding whenever you were spending time with me that you might otherwise be spending with them! I can't thank you enough.

For my family

Chapter 1

Introduction

1.1 Motivation

If you take nearly any liquid and cool it below that substance's melting temperature with sufficient rapidity, crystallization is avoided and the liquid then enters a "supercooled" state. As the liquid is further cooled, its viscosity (the material's resistance to deformation) will increase extremely rapidly [1]. When the characteristic relaxation time of the liquid reaches 1000 seconds (and the viscosity reaches 10^{13} poise), flow becomes so slow that the material is, in effect, solid. This solid is termed a "glass."

What, then, distinguishes a glass from a crystal? At the molecular level, a glass retains the disordered structure of the liquid from which it was formed. Liquids and glasses are amorphous materials, which have no periodic *long ranged* order [1]. In a pure crystal, units of structure repeat such that if the positions of the atoms are know in one unit cell, one can predict the position of atoms anywhere else in the bulk of the material. The length over which structure is correlated is effectively infinite compared to molecular dimensions. In a liquid or glass, knowing the position of one molecule in the system does convey information about where *nearby* molecules are likely to be found, but this information decays rapidly with distance. This distinction between ordered and amorphous materials can be measured

through scattering experiments (see Sec. 1.3).[1] If the structure of a glass is not distinct from the liquid from which it was formed, what then is the origin of the steep viscosity increase that is the central characteristic of glassy systems? The answer is that the structure of the supercooled liquid *is* changing, but in subtle ways. The ways in which small changes in amorphous structure translates to dramatic changes in relaxation times remains unsolved to this day, despite decades of intense scrutiny [2]. While the mystery has not yet been cracked, there are many theories of the glass transition that *do* explain some of the phenomenology associated with supercooled liquids, although most of these theories are not grounded directly in molecular structure [2]. In my thesis research, I have used computer simulations of model glass-forming systems to provide evidence which can help support or distinguish between various theories of the glass transition. In particular, each chapter herein pertains in some regard to the connection between local structural order and glassy dynamics.

The study of glasses and supercooled liquids is important for several reasons. First, glasses are an extremely important class of materials for commercial applications. These include their age-old use in window panes, as protective materials for modern electronic devices, and for applications in the pharmaceutical industry, where the amorphous packing of drug molecules can result in enhanced solubility and other desirable properties for drug delivery [1, 2]. Secondly, the physical nature of the glass transition is a deep fundamental problem, with connections to problems in many other areas of science [2]. The ideas and techniques developed in the study of the glass transition have many parallels and applications in other fields such as in the study of biology (e.g. in the folding of proteins and biological networks) and "hard" (in the technical sense) computer science problems.

[1] Quasicrystals are a third class of materials. They are fully ordered without being crystalline, in that their structure does not have repeating units. The 2011 Nobel Prize in chemistry was awarded to Dan Shechtman for his discovery that quasicrystals can be formed from natural materials.

1.2 A brief summary of some theories of the glass transition

The literature on the glass transition is fairly vast and proves daunting both to newcomers as well as to experts. Fortunately, many excellent works exist which can serve to provide an overview of the field and nuanced discussions of subtle physical points and disputes. Some good examples are to be found in Refs. [1–7] and the books [8–10]. My understanding of these topics has *particularly* benefited from reviews by (alphabetically) Berthier and Biroli [2], Cavagna [6], Ediger [1, 4], and Kob [3, 5, 9]. I have been fortunate to have learned directly from discussions and collaboration with these authors. Here I will *very* briefly summarize important aspects of the problem to prepare the reader for their appearance in subsequent chapters.

There are many aspects of the dynamics of supercooled liquids that do not occur in liquids under normal conditions and that are quasi-universal in all glass-forming materials. For the purpose of the chapters in this thesis, there are two behaviors that have primacy. The first is the dramatic slowing down of the liquid (increase in viscosity, or characteristic relaxation times) and the second is the presence of dynamical heterogeneity. Dynamical heterogeneity is the name for the experimental fact that when the dynamics of a supercooled liquid are measured and spatially resolved, some regions will be found to be much less "mobile" or "active" than others. We say these regions have lower *propensity* for motion or a lower *mobility*.

Kauzmann noticed in the study of supercooled liquids that if he extrapolated his measurement for the entropy of the liquid as it is cooled and the entropy of a crystal of the same material as it is cooled, that those values would eventually cross at a temperature below the glass transition temperature T_g (defined as the temperature where the liquid viscosity reaches 10^{13} poise). Scientists studying the glass transition usually speak of the "configurational entropy," that is, the component of the entropy that comes from distinct ways to arrange molecules but not from vibrational motion. This putative "entropy crisis" or Kauz-

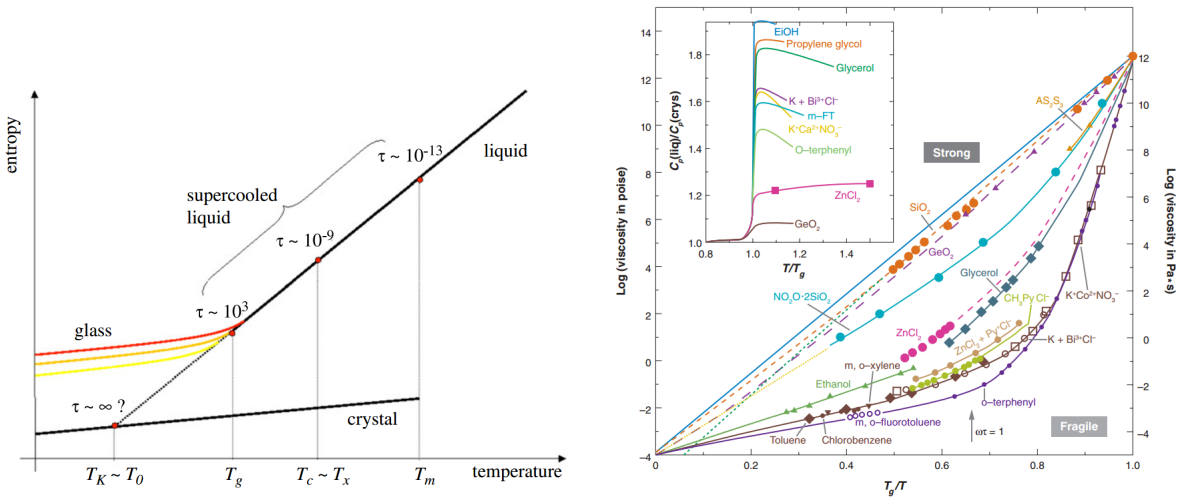

Figure 1.1: (Left) Schematic of cooling a liquid to form a glass from Ref. [6]. Some important temperatures described in Sec. 1.2 are the melting temperature of the solid, T_m, the mode coupling temperature, T_c, and the Kauzmann temperature T_K. The conventionally defined glass transition temperature T_g is also shown as the place where the liquid falls out of equilibrium, and the behavior after that point depends on the cooling rate (shown in different colors). Another line shows the result of extrapolating the entropy of the liquid down until it intercepts that of the crystal, illustrating the Kauzmann's result. (Right) Plot of the logarithm of viscosity versus inverse temperature scaled to the glass transition temperature, also known as an Angell plot, from [7] which adapted a figure from Ref. [11]. This plot shows that the behavior of many different glass forming substances is quasi-universal and can be classified as going from fragile to strong depending on the convexity the data represented in this way. The inset also shows that the heat capacity of the glass quickly approaches that of the solid at T_g, not otherwise discussed here.

mann paradox[2] led to the suggestion that there may be a phase transition at a temperature T_K, the "Kauzmann" temperature, to an "ideal glass" state that, like a crystal, has (almost) no configurational entropy[3] [1].

It had been observed that the viscosity of supercooled liquids when cooled could be fit to a Vogel-Fulcher (VF) form [1],

$$\eta \propto e^{\frac{A}{T-T_{VF}}}. \tag{1.1}$$

From the theory of Adam and Gibbs and DiMarzio [12, 13], the idea emerged that for particles to rearrange when they are stuck in a glassy state, there must be some "Cooperatively Rearranging Regions", i.e. groups of particles that move in a concerted manner. They suggested that the barrier to relaxation was proportional to the number of particles in these regions and that this number of particles is inversely proportional to the configurational entropy. They moreover proposed that the configurational entropy vanishes with $s_c(T) \propto (T - T_K)/T_K$ and hence by the Arrhenius relationship relaxation in the system should occur on time scales which grow with decreasing temperature as $\tau \propto \exp(AT_K/T(T - T_K))$. Since T_K is typically very far from absolute zero, as $T \to T_K$ this can be approximated as $\tau \propto \exp(B/(T - T_K))$, hence explaining the empirical VF form (since τ is proportional to η).

Goldstein later explained the glass transition using the picture of a rough (free-) energy landscape. A crystalline state is at the bottom of the free energy landscape, but when a liquid is supercooled, it is trapped in a local energy minimum far above the global one. At a given temperature, the supercooled liquid hops between local minima that are all similar in energy. As the temperature is lowered, it gets trapped in deeper local minima such that the barriers between hops would grow, resulting in a super-Arrhenius growth in relaxation times of the system. Similar to the previous theory, these barriers increase due to the growing number of particles that collectively rearrange to relax the system [14].

The theories mentioned thus far are based on thermodynamic quantities. Mode coupling

[2]The paradox as such is that the entropy of a liquid might be less than that of a crystal. In fact, though strange, this is not really one and indeed it is the reason that liquids composed of hard spheres crystallize.

[3] Or to be more technical, sub-extensive configurational entropy

theory (MCT) was developed to try to find a microscopic, dynamical origin for the glass transition. The idea of mode coupling theory is to develop a self-consistent set of equations that predicts the increase in viscosity of the liquid based on only the slight change in structure that takes place. This theory is successful in many ways. One of the major problems with it, however, is that it predicts a divergence in relaxation times $\tau \sim (T - T_c)^{-\gamma}$ at a mode-coupling transition temperature T_c that is far higher than T_g and T_K. This problem is sometimes explained by saying MCT is a hydrodynamic theory and does not take into account hopping-type motion. Hence there could be a *crossover* in behavior near T_c where events such as those in the Goldstein picture becomes more important [2, 6, 15, 16].

Random-first order theory (RFOT) is a framework which has its origins based in all of the preceding ideas [2, 6]. In the RFOT picture, the system can be divided into a "mosaic" of states that each have different local configurational entropy. Because there are many available states, a given mosaic patch pays an entropic cost to stay in one state, hence the particles in it will try to rearrange. However, in doing so there is an energetic cost because the new state does not match perfectly the boundary induced by the adjacent patches. The interplay between the entropic gain of changing states (which scales approximately with the volume of the patch) and the energetic cost of breaking the interface with adjacent areas (which scales with the surface area of the patch) leaves the system in a steady-state with patches having an average size that depends on temperature, and in particular grows with decreasing temperature. As in the work of Adam-Gibbs-DiMarzio, the barrier to relaxation is proportional to the size of the region that has to re-arrange, and the growing length scale predicted in RFOT also results in a generalized Vogel-Fulcher growth in relaxation times commensurate with experiments. In RFOT, MCT applies down to approximately T_c, and then below that temperature the mosaic picture begins to be applicable. The length scale of the RFOT mosaic entails a measurement of "amorphous order," and potential ways to measure this length scale will be discussed in Chapter 2.

The theories I have presented thus far are a biased subset necessary to best understand the results presented in this thesis. However, there are others that are very important. A

distinct picture known as the Kinetic Facilitation theory of the glass transition provides a counterpoint to the theories previously mentioned [17]. From this perspective, the important aspects of the problem are exactly those mentioned before: dramatic slow down and dynamical heterogeneity. In the Kinetic Facilitation picture, we imagine that in the glass there are only rare "defect" regions which are able to relax at any given time. These defects are the central object of the theory. Hence we are left with a gas of defects or "excitations" that diffuse throughout the system and become more sparse and thus farther apart as the system is cooled. This results in the required relaxation behavior, as the disappearance of defects results in the increase in relaxation times, and the fact that relaxation only occurs near defects results in dynamical heterogeneity. The dynamics are termed facilitated, because after one region relaxes, an adjacent one will relax, and so on. A consequence of some models that fit this picture is that relaxation is hierarchical, in that relaxations at a given length scale produce relaxation on a larger length scale. For the most part, this picture makes little reference to what structural features compose these defects, though some work has been done to define these structures in terms of coarse-graining of features in models such as those described in the next section [18, 19]. Work in this area predicts an inverse square divergence of the logarithm of relaxation times, which seems to have similar validity to the quality of VF fits to experimental and simulation data [20]. Models related to this theory have also been used to make seemingly non-trivial predictions, for example, matching the the results of real calorimetry experiments with only the input of a few parameters from experiments [21].

1.3 Computer simulations of liquids and glasses

Many of the consequences of the theories described in Sec. 1.2 are difficult to distinguish using experimental probes. One way to better understand these consequences is to find simple systems which exhibit the general properties we wish to understand as emergent behavior, and then try to understand what features of the models led to those emergent

properties. All of my work in this thesis has focused on the use of systems of interacting spheres whose full details can be found when needed in the subsequent chapters. All of the systems are characterized by pairwise interactions and in all but one case they are binary systems. It was found early on in the study of such systems that monotonic systems tend to crystallize when cooled, but introducing a second, differently sized, species into the system frustrates the crystallization process. General descriptions of the systems can be found in Tab. 1.1. Despite having many differing qualities, these systems can all be supercooled to liquid states that are not crystalline and exhibit the two key characteristics described above: dramatic increase in relaxation times and dynamical heterogeneity. In this Section, we will discuss how these properties are measured. I note here in passing that there are many other models of glassy systems, including those that better model bonded systems by having three body interactions [22] and many other models whose components are constrained to the sites of a lattice. These lattice-based models are very important as they are simpler and it is easier to get a handle on the origin of their glassy properties. In addition, different version of these models can give motivation and justification for both the RFOT and Kinetic-Facilitation pictures described in Sec. 1.2.

The motivation for particle-based models of glassy systems is that they retain the flavor of molecular glasses[4] while being far simpler to simulate. The simulation of realistic molecules requires the use of bonded and charged species, both of which are far more expensive to simulate than the spherically symmetric, short ranged interactions given in Tab. 1.1. The main feature lost by this simplification is the ability to study the effect of supercooling on rotational dynamics, an important and experimentally accessible quantity [23, 24].

There are two general classes of methods for simulating physical systems. The first is the method of "Molecular Dynamics," (MD) in which, after placing the N "molecules" into a box of volume V and giving them some initial velocities based on the desired temperature T, one makes use of:

1. The forces between all components in the system computed by taking the gradient of

[4]Or dense colloidal systems.

the potential energy function between the molecules.

2. Newton's equations of motion, which are integrated numerically to move all of the constituents to new positions and to update their velocities based on the interactions at the new locations.

As stated, executing the steps above will conserve the total energy of the system, but methodological developments in this area have been developed to control the temperature or pressure, as well as for performing the latter of these steps in an efficient manner. Most molecular dynamics methods are now standard and can be found in many textbooks including those of Frenkel and Smit [25] and Tuckerman [26]. In particular, for the study of liquids, the classic book by Allen and Tildesley, despite being over 25 years old, remains required reading [27].

The second class of methods fall under the umbrella of "Monte Carlo" (MC) methods, with the name derived from the central aspect of the methods being random sampling. Here, in general, the method consists of (after again placing N molecules in a box of volume V and choosing a temperature T) the following stages:

1. Compute the total energy of the system.
2. Pick a molecule at random.
3. Move it in a random way.
4. Compute the new energy of the system.
5. Choose whether to keep the new configuration, or to go back to the previous one.

The key step in this method is the final one. The choice of whether to accept or reject the random move must be made in such a way that all of observables match correct thermodynamic properties for a temperature T. This can be done by satisfying "detailed balance," the property that the forward and back moves occur with equal probability. Generally this is carried out by having the random moves of the molecules have no directional dependence

and having the acceptance criterion for going from state A to state B be the Metropolis one:

$$P(A \to B) = 1, \text{ if } E_B < E_A \tag{1.2}$$

$$= e^{-(E_B - E_A)/k_B T} \text{ otherwise} \tag{1.3}$$

where k_B is Boltzmann constant and E_A and E_B are the total energies of states A and B respectively. Refs. [25–27] all have information about Monte Carlo methods, and I have also found the book of Newman and Barkema to be particularly helpful [28].

Monte Carlo techniques were first applied to a liquid of spheres by Metropolis, Rosenbluth, Rosenbluth, Teller, and Teller [29]. The first MD simulation for hard spheres followed shortly thereafter by Alder and Wainwright [30]. The first actually *molecular* MD simulations were performed by Berne and Harp [31]. An interesting review on early applications of these methods to supercooled liquids can be found in Ref. [32].

To study glassy systems using these methods, we first generate a series of configurations at a high temperature where we believe the system is not glassy. We then take those configurations and run simulations at a decreased temperature, take the final configurations from those simulations. This process is then repeated. If it is indeed a model of a glassy system the length of time needed to perform the simulations should increase exponentially in order to harvest equilibrium configurations. At some point we must stop, either because the model is not a very good one for our purposes and the samples crystallize, or because the length of the simulations exceed the length we are willing to wait for results. We then take supercooled liquid configurations at differing temperatures and generate new series of configurations (a "trajectory") using MD or MC. In principle, MC simulations don't convey any dynamical information, but in practice the resulting trajectories for dense glassy particulate systems are quite similar to those generated by MD [33]. However, this property is not exploited in this thesis.

We now need to check that these configurations have the desired properties necessary to use them as model glass formers. There are three main quantities that we use in this thesis. The first is a measurement of the the local structure of the liquid, called the radial distribution function or $g(r)$. $g(r)$ is the relative probability of finding a particle at a distance

r from the position of a tagged particle. It is computed by histogramming all of the particle distances in the system into bins of width Δr and then, at each distance, dividing by the probably of finding a particle in a shell of width Δr. $g(r)$ is defined formally in many books including Ref. [25, 26, 34]. When $g(r)$ is measured both for a sample liquid and for that same sample when supercooled, there are slight change in structure. $g(r)$ can be extracted from experimental light or neutron scattering experiments, and is related directly to the Fourier transform of the static structure factor $S(k)$. The result for a model system is found in Fig. 3.1.

In order to measure *how* supercooled the system is, we measure the self-intermediate scattering function [35]:

$$F_s(k,t) = \left\langle \frac{1}{N} \sum_{j=1}^{N} e^{i\mathbf{k}\cdot\delta\mathbf{r}_j(t)} \right\rangle = \left\langle \frac{1}{N} \sum_{j=1}^{N} \cos(\mathbf{k}\cdot\delta\mathbf{r}_j(t)) \right\rangle, \tag{1.4}$$

where $\delta\mathbf{r}_j(t) = \mathbf{r}_j(t) - \mathbf{r}_j(0)$ and the second equality is due to the fluid being isotropic and averaging over $\mathbf{k}$-vectors with length $k = |\mathbf{k}|$ pointing in all directions. At the beginning, the particles will not have moved at all, and we see that $F_s(k,0)$ will have a value of unity. The value of k is an inverse length scale on which particle motion is being measured. As the system evolves, the average particle displacement will grow relative to k^{-1} (if the system is indeed still a liquid) and the oscillating functions will have a shorter and shorter period, and hence $F_s(k, t \to \infty) = 0$. The length of time it takes $F_s(k,t)$ to decay completely depends on k and how glassy the system is. In Fig. 1.3 we show the way in which $F_s(k,t)$ decays over longer and longer time scales as the temperature is decreased in a glassy system. We can extract a relaxation time τ_α by the standard choice $F_s(k, t = \tau_\alpha) = 1/e$ for a k value approximately $2\pi/\sigma$, i.e. inversely proportional to the nearest-neighbor distance between particles in the system. In Fig. 1.3(c), τ_α can be seen to grown faster than the Arrhenius form e^{E/k_BT} as T is decreased, showing this system is a "fragile" glass as defined in Fig. 1.1.

Finally, we wish to study dynamical heterogeneity. To do this, we can assess after a given length of time, how much of the system has moved and how much of the system remains close to the initial configuration. The easiest quantity to investigate in this regard is called

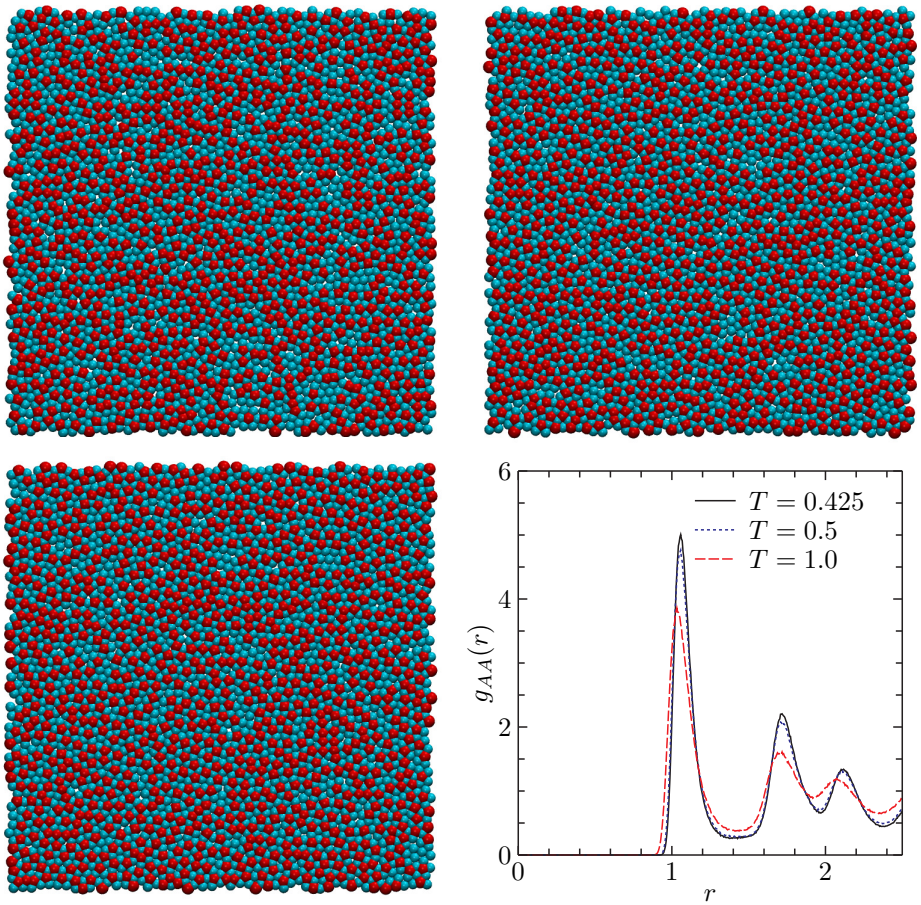

Figure 1.2: Snapshots of configurations of the 2D Kob-Andersen system at a normal liquid temperature, $T = 1.0$ (top left), and supercooled temperatures $T = 0.5$ (top right) and $T = 0.425$ (bottom left). In the bottom right is shown the radial distribution function for the large particles in the system, which has generally the same structure at $T = 1.0$ and $T = 0.425$ between which relaxation times have increased by a factor of over 500. The structural change between $T = 0.5$ and $T = 0.425$ is minute, and there the relaxation time increases by a factor of 10.

Name	**Potential -** $V(r_{ij})$	**Species**	**Density**	**Attractions?**
Kob-Andersen (KA) [36]	$4\epsilon_{ij}\left(\left(\frac{\sigma_{ij}}{r_{ij}}\right)^{12}-\left(\frac{\sigma_{ij}}{r_{ij}}\right)^{6}\right)$	2	1.2	Yes
Soft-sphere (SS) [37] & Pedersen (IPL) [38]	$A\epsilon_{ij}\left(\frac{\sigma_{ij}}{r_{ij}}\right)^{n}$	2	1.0, 1.2	No
Weeks-Chandler-Andersen (WCA) [39] (for KA)	$4\epsilon_{ij}\left(\left(\frac{\sigma_{ij}}{r_{ij}}\right)^{12}-\left(\frac{\sigma_{ij}}{r_{ij}}\right)^{6}\right)+\epsilon_{ij}$, $r<2^{1/6}\sigma_{ij}$	2	1.2	No
Harmonic Spheres (HARM) [40]	$\epsilon_{ij}\left(1-r_{ij}/\sigma_{ij}\right)^{2}$	2	0.675	No
Wahnstrom (WAHN) [41]	$4\epsilon_{ij}\left(\left(\frac{\sigma_{ij}}{r_{ij}}\right)^{12}-\left(\frac{\sigma_{ij}}{r_{ij}}\right)^{6}\right)$	2	1.297	Yes
Gaussian Core Model (GCM) [42]	$\epsilon e^{-(r/\sigma)^2}$	1	2.0	No

Table 1.1: List of systems studied in this thesis and their general characteristics. r_{ij} is the distance between two particles i and j, and ϵ_{ij} sets the energy scale of interaction between them while σ_{ij} represents the "diameter" or the sum of the radii of particles i and j, though in the KA, IPL and WCA potentials it is not additive as such. Species is the number of particle types, density is the number density $\rho = N/V$ and Attractions lists whether the potential has any attraction, i.e. whether it is negative at any distance.

$\chi_4(k,t)$ or the 4-point dynamical susceptibility. We can compute this quantity by looking at the fluctuations in $F_s(k,t)$ [33]:

$$\chi_4(k,t) = N\mathrm{Var}\left[F_s(k,t)\right] = N\left[\langle F_s(k,t)^2\rangle - \langle F_s(k,t)\rangle^2\right]. \tag{1.5}$$

$\chi_4(k,t)$ grows as the system is supercooled, as can be seen in Fig. 1.3(b-c), showing that the amount of dynamical heterogeneity increases with glassiness as is observed in experimental studies.

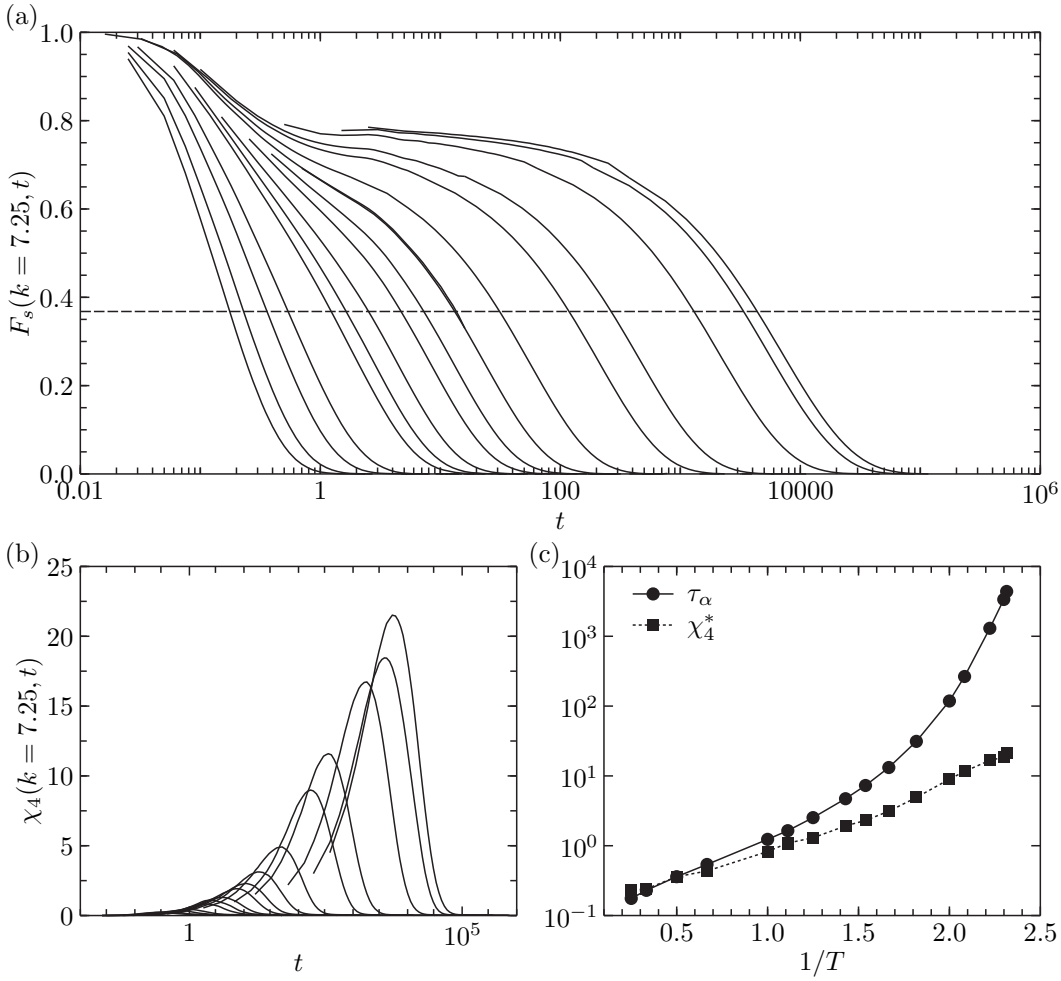

Figure 1.3: (a) Self-intermediate scattering function for the three-dimensional Kob-Andersen system with $N = 1900$ and temperatures from $T = 4.0$ down to $T = 0.432$. Intersection with horizontal dashed line defines τ_α. (b) χ_4 for the same simulations as in (a). (c) Relaxation time τ_α and peak height of χ_4 as a function of inverse temperature.

1.4 Thesis chapters in context

Having introduced the phenomenology of glassy systems and the techniques and systems used to investigate them, I now preview the contents of this thesis in context. All work in this thesis was performed under the guidance of and in collaboration with Prof. David R. Reichman.

In Chapter 2, I extract a static length scale of amorphous ordering for three different model systems and show evidence in the mildly supercooled regime that the growth in this length scale correlates with growing relaxation times in these systems, as might be predicted from RFOT-like ideas as described in Sec. 1.2. This work was done in collaboration with Thomas E. Markland.

In Chapter 3, I study the way that a glassy systems makes moves between adjacent energetic minima. We find that as the system is cooled, the directions along which the system moves are more and more aligned with the "normal modes" of the system, i.e. the directions the system can move to relax are more and more dominated by the current structure and the local energy landscape around that structure.

In Chapter 1, I investigate the effects of fixing the position of a set of particles to form a wall inside of the system. In particular I study the range over which the wall has an effect at different temperatures and find that the growth of this length slows down with cooling. I also find evidence for a change in the way particles can relax at an only mildly super-cooled temperature by the study of this length and by studying the difference in the wall's effect on motion perpendicular and parallel to its face. This work was performed in collaboration with Ludovic Berthier and Walter Kob.

In Chapter 5, I study how correlated is the local packing arrangement of a particle and its neighbors with how slow that particle is likely to be. Here we directly probed the connection between local structure and dynamical heterogeneity and found the answer to depend on which model we studied. We can still measure that there is *some* structural effect which induces dynamical heterogeneity, and hence we have shown that theories of the glass transition based only on purely local structure may run into trouble. We also present

results suggesting the quantities studied in Chapter 2 may present an alternative structural measurement to use when searching for the origin of dynamical heterogeneity. This work was done in collaboration with Daniele Coslovich and Atsushi Ikeda.

Finally, in Chapter 6, we study the effect of randomly pinning a percentage of particles in a glassy configuration by heating the system up to a higher temperature and watching it relax. By mimicking experimental setups, we show that these glasses with pinned particles have many similarities to experimentally produced "ultra-stable glasses," which are very deep in the energy landscape as if they had been cooled very close to T_K. This work was done in collaboration with Ludovic Berthier.

Chapter 2

Growing point-to-set length scale correlates with growing relaxation times in model supercooled liquids[1]

2.1 Introduction

The search for growing length scales accompanying the glass transition has been a major focus of the field for two decades [2]. Great progress has been made in quantifying the behavior of dynamical length scales associated with emergent dynamical heterogeneity, such as ξ_4, the length scale of the 4-point susceptibility [43]. Less mature is our understanding of possible thermodynamic length scales that grow upon supercooling. In some theories of the glass transition, such as the random first-order theory (RFOT), dynamical arrest is connected to a particular thermodynamically-based length scale associated with the depletion of independent particle configurations constrained by neighboring particles [7, 44]. Within this viewpoint the putative structural length scale is distinct from ξ_4 for modest supercooling [45]. In other approaches this length scale may be identical to that associated with

[1] Adapted from the work published in Phys. Rev. Lett. **108**, 225506 (2012).

dynamical heterogeneity at all temperatures [46, 47]. Furthermore, in these contrasting viewpoints the relationship of the various growing length scales with growing relaxation times are different. Clearly, elevating our level of knowledge of growing thermodynamic length scales associated with glass formation to that of dynamical ones is of paramount importance in the continued quest for a deeper understanding of the behavior of supercooled liquids and glasses.

A precise definition of one type of non-trivial structural length scale akin to that envisioned in theories like RFOT was put forward by Bouchaud and Biroli in 2004 [48]. Their work suggests a procedure for the extraction of this length scale in computer simulations. This length is a measure of the distance scale over which particles are self-consistently pinned by other particles in their vicinity. The static correlations embodied by this length scale are known as "point-to-set" (PTS) correlations. In what follows, we will use ξ_{PTS} to denote the PTS length scale. There has been a recent flurry of activity in the extraction of variants of ξ_{PTS} in a host of model glass forming systems [37, 47, 49–53]. In this Chapter we use this technique to address the crucial question of correlation between ξ_{PTS} and dynamics in systems with identical simple structural features (e.g. radial distribution functions, $g(r)$) but noticeably distinct relaxation time scales.

2.2 Systems and methods

We consider three closely related systems, chosen specifically to address this problem. The first two are the standard Kob-Andersen binary Lennard-Jones mixture (LJ) [54] and its Weeks-Chandler-Andersen truncation (WCA) [39], which were previously found to have significantly different dynamical behavior at supercooled temperatures [55], despite having nearly identical two-body static correlations at all temperatures (e.g. measured by $g(r)$). The third is a system characterized by a repulsive inverse power law potential (IPL) and was constructed based on the composition and parameters of the LJ system to reproduce both two-body structural features and the dynamics of the LJ model [38]. The similarities

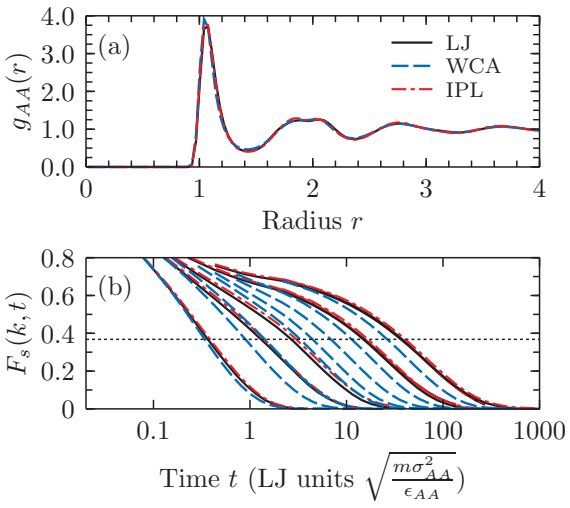

Figure 2.1: (a) The radial distribution functions for A-type particles at $T = 0.6$ for the three models studied as an illustration of the structural similarity between the models. Other temperatures and pairs are shown in Sec. 2.6. (b) The self-intermediate scattering functions for A-type particles at $k = 7.25$ for NVE molecular dynamics simulations of the bulk systems. The alpha relaxation, τ_α, is defined as the $1/e$ time of $F_s(k,t)$, illustrated by the horizontal dotted line. Curves shown for all models are, from L-R, $T = \{2.0, 1.0, 0.8, 0.6, 0.55\}$ and additionally for WCA $T = \{0.5, 0.45, 0.4\}$. Note the LJ and IPL match at all temperatures while the WCA matches only at T=2.0 and decays significantly faster at lower temperatures. These temperature represent the regime computationally accessible to our cavity simulations. Parameters for the models can be found in Sec. 2.6.

in pair correlations are illustrated in Fig. 2.1(a), and the structural relaxation times for the temperatures in this Chapter are shown in Fig. 2.1(b). While it should be noted that minor differences exist in $g(r)$ between the three systems [38] (see Sec. 2.6), they are far too small to account for the significantly weaker temperature dependence of relaxation times in the WCA system. In particular, neither mode-coupling theory nor activation-based theories that rely solely on the radial distribution function can account for this distinction [56]. These three systems will allow us to study whether ξ_{PTS} is sensitive to structural differences in the three models not appearing at the level of $g(r)$, and if so whether ξ_{PTS} can distinguish the LJ and IPL from the WCA.

To measure ξ_{PTS}, we follow the protocol of Ref. [37]. All simulations were performed by

the Monte Carlo (MC) technique of Ref. [57]. Bulk equilibrium configurations are generated at a desired temperature, and then cavities are constructed by freezing the particles outside a sphere of radius R. The center of the cavity is partitioned into $\tilde{N}$ cubes of side length l. The overlap is then defined as $q(R,t) = (l^3\tilde{N}\rho)^{-1}\sum_{i=1}^{\tilde{N}}\langle n_i(t_0)n_i(t_0+t)\rangle$ where brackets denote both a thermodynamic average and an average over independent cavities, and $n_i(t)$ is a binary digit specifying whether a particle is in box i at "time" t (time here standing for any measure of simulation progress). As the cavity evolves in simulation, this quantity decays to a plateau which is independent of time and denoted $q(R) = \lim_{t\to\infty} q(R,t)$. Overlaps generated in this fashion will be referred to as "standard overlaps". With the preceding definition, two independent configurations will have an overlap $q = \rho l^3$ which is also the value of $q(R \to \infty)$. We will henceforth subtract off this bulk overlap from q, and denote the resulting value $\tilde{q}$. Further details can be found in Sec. 2.6.

A major complication of the algorithm sketched above is that the plateau value $q(R)$ will over-estimate the true thermodynamic value of the overlap if the particle configuration inside the cavity breaks ergodicity or if the confinement simply induces relaxation on a time scale beyond that accessible to our simulations. We note that for all three systems studied here, relaxation times increase dramatically as cavity radius is decreased. The technique of particle swapping [57] ameliorates this problem in some systems, but is not effective in the systems studied here, as swap moves that exchange particles of different species are almost never accepted at supercooled temperatures. To test for convergence to the true (thermodynamic) value of $\tilde{q}(R)$, Cavagna and coworkers have proposed a technique based on the insertion of a *random* configuration of the same particles in the same cavity [58]. Initially such a configuration will have, on average, zero overlap ($\tilde{q} = 0$) with the pre-randomized configuration, but the structure of the boundary will induce finite overlap at long times. If this value measured with respect to the initial configuration yields the same value of $\tilde{q}(R)$ as that extracted from the direct decay of $\tilde{q}(R,t)$, one can be confident that the true thermodynamic value of the overlap has been obtained [58]. This quantity is difficult to converge in our systems, hence we have implemented an approach which we call "particle size

annealing" (PSA). In this method the particles inside the cavity are instantaneously reduced in size such that their positions quickly randomize, and are then evolved with the constraint of the cavity in place while their diameters are slowly tuned back to their original size. We have found this method, which is similar in spirit to algorithms used to generate randomly jammed packings of hard spheres [59], is more efficient and reliable in the generation of converged overlap values than standard Monte Carlo sampling. In what follows, we use PSA both as a check of the convergence of $\tilde{q}(R)$ to its thermodynamic value and as a means of generating estimates of $\tilde{q}(R)$ for small R values. Specifically, for radii where standard and PSA overlap values match within error bars, the standard overlap is taken as the thermodynamic overlap. For smaller radii, the value from PSA yields a lower bound to the converged thermodynamic value of $\tilde{q}(R)$. Further, we expect PSA to yield estimates of $\tilde{q}(R)$ that are extremely close to the desired thermodynamic values. This expectation arises from a comparison with other sampling techniques (e.g. replica exchange) and direct Monte Carlo sampling. A discussion of these comparisons will be made in a future publication. Details of our approach may be found in Sec. 2.6. Example results for a single cavity size can be seen in Fig. 2.2(a).

2.3 Results

We now turn to a discussion of the extraction of ξ_{PTS} from the spatial decay of the converged overlap function $\tilde{q}(R)$. Overlaps were fit to a generalized compressed exponential of the form $\tilde{q}(R) = A\exp(-\left(\frac{R-a}{\xi_{PTS}}\right)^{\eta})$. Though a previous study used a pure compressed exponential (i.e. $a = 0$) [37], we choose $a = 1$, physically motivated by the fact that cavities with $R \sim 1$ should on average contain a single particle and that the overlap properties at this cavity size should not be sensitive to growing amorphous order. Furthermore we do not expect the same compressed exponential form to extend to cavities containing on average fewer than one particle. Fixing an $a > 0$ allows us to perform a two-parameter fit with fixed A, leading to values of ξ_{PTS} with much smaller statistical variance. We find that for $a = 1$, $A = 0.5$ gives good fits to the data for all three systems at all temperatures studied; some example

fits can be seen in Fig. 2.2(b) and 2.2(c). An extended discussion of our fitting choices and methodology can be found in Sec. 2.6, as well as a table of fit parameters extracted from the data.

Fig. 2.3(a) illustrates our first main result, namely the growth of the absolute thermodynamic length scale ξ_{PTS} for all three systems discussed above. Several notable features deserve mention. First, it is clear that the length scale ξ_{PTS} grows unambiguously as temperature is lowered. This is fully consistent with other recent studies that demonstrate growth of ξ_{PTS} in a variety of pinning geometries [37, 47, 49–53]. Second, the distinction between the magnitude of ξ_{PTS} in the WCA system compared to the LJ and IPL systems at the same absolute temperature is stark. Despite the fact that the pair distribution functions of all three systems are nearly identical, the more subtle structural marker ξ_{PTS} can clearly distinguish the WCA system from the other two. The lengths of the IPL and LJ are found to be nearly identical at all temperatures and much larger than those found for the WCA.

We now address the crucial question of correlation with relaxation times in a quantitative manner. Is ξ_{PTS} correlated in a one-to-one manner with the alpha relaxation time τ_α extracted from the self-intermediate scattering functions of the systems under investigation? A key component of the answer to this question may be found in Fig. 2.3(b). While the absolute magnitude of ξ_{PTS} in the WCA system is clearly smaller than that of the other two systems at the same temperature, the lengths of all three systems collapse when temperature is scaled to the value where $\xi_{PTS} \approx 1.4$. These temperatures are quite similar to values obtained for "onset" temperatures obtained by independent means in earlier work [55]. In Fig. 2.3(c) we show the behavior of relaxation times τ_α (obtained from NVE molecular dynamics of bulk equilibrium systems) as a function of ξ_{PTS} in all three systems. Reasonable data collapse is found, signifying a strong correlation between these quantities in all three systems. Fig. 2.3(d) shows a scaling plot where the independent variable takes an activated form $\ln(\tau_\alpha) \sim \xi_{PTS}/T$, normalized by the values of the lengths and temperatures found from Fig. 2.3(b). The degree of collapse is similar to that shown in Fig. 2.3(c) with no adjustable parameters, making it difficult to distinguish between scaling forms where the temperature

dependence of the growth of τ_α may be attributed purely to the growth of ξ_{PTS} alone or the activated form commonly found in the literature [2, 7, 44]. Furthermore, both Figs. 2.3(c) and 2.3(d) show slight but systematic deviations from perfect data collapse, suggesting that similar but distinct exponents associated with the scaling variable (ξ_{PTS} or ξ_{PTS}/T) would be required to extend these scaling plots to larger τ_α values; this may be similar to what is seen in Ref. [60].[2] Regardless, the correlation between ξ_{PTS} and relaxation time growth is striking. Finally, we note that within the resolution of our current data, when relaxation times of these three models are similar, it is not only ξ_{PTS} as defined here that matches, but rather the full overlap profile $\tilde{q}(R)$; this is illustrated in the insets of Fig. 2.2. Hence, though our definition of ξ_{PTS} is not unique, we expect any reasonable definition to give the same qualitative results as seen in Fig. 2.3.

2.4 Conclusions

The results presented here provide useful clues to the underlying causes of the viscous slowdown of dynamics during the supercooling process. ξ_{PTS} is the central structural feature associated with slow dynamics in RFOT-like theories [2, 7, 44]. In this sense, the results presented in Fig. 2.3 would seem to be in harmony with that viewpoint. It should be noted, however, that within the standard RFOT, the lengths in the relatively high temperature regime are not expected to necessarily correlate strongly with relaxation times, as they do here. Our results bear a resemblance to some features found in some short-ranged p-spin models, which serve as a possible paradigm for how the mean-field models that RFOT is based on are altered by fluctuations. In particular, a weakly growing static length scale that is linearly correlated with $T\ln(\tau)$ all the way up through the high temperature regime as in Fig. 2.3(d) are features found in the model of Ref. [61]. Unfortunately, the static correlations

[2] In Fig. 8 of Ref. [60], Coslovich shows a relationship between cluster size of locally preferred structures in the LJ and WCA systems. Though he finds deviations at low temperatures, his Fig. 8 also implies approximate scaling of the "length" scale $\sim N_{LPS}^{1/3}$ with τ_α in the temperature regime of our work. A relationship between such clusters and ξ_{PTS} is not yet established.

in this model are spin-glass correlations, which are absent in real liquids. In general, studies such as those carried out here should shed light on how fluctuations modify (or destroy) the mean field behavior upon which the standard version of RFOT is based [62, 63].

The mere existence of a growing ξ_{PTS} is *not* in contradiction with a picture based on kinetically constrained models; however there are several aspects of our results which seem difficult to reconcile with the facilitated picture. To address this, one has to examine results from thermodynamically interacting models which can be mapped onto kinetically constrained models. It has already been noted that local dynamics inside compact cavities show markedly increasing relaxation times as the cavity radius is decreased [50]. While the same behavior holds in the three systems studied here (not shown), the opposite is true for large cavities in the triangular plaquette model, the one model known to be dual to a kinetically constrained model with hierarchical behavior [47]. In addition, the absolute length scales found here are quite small. Since ξ_{PTS} might loosely be interpreted as the mean distance between defects in a facilitated model, this fact would seemingly translate into an unrealistically high density of defects with a rather weak temperature dependence. Indeed, the magnitude of ξ_{PTS} found in this Chapter seems more consistent with the spatial extent of the "defects" found in a recent study than the separation between these regions [19]. Lastly, our results seem consistent with the idea that ξ_{PTS} and ξ_4 are distinct in the regime of weak to moderate supercooling [49], which would be unexpected in models such as the triangular plaquette model [45, 47].[3] It is important to bear in mind that plaquette models provide merely a small set of all possible mappings of an interacting system to one of kinetically constrained but thermodynamically non-interacting defects. It is unlikely, however, that any such mapping would have much to say about the small length scales found in this Chapter, which are expected to be similar to the coarse graining length scale in any mapping to a kinetically constrained model [18].

[3] This behavior is consistent with the square plaquette model, which is dual to the two-dimensional Fredrickson-Andersen model. This model has Arrhenius transport, unlike the atomistic systems studied here.

In conclusion, ξ_{PTS} in three model glass forming systems has been been extracted. Care has been exercised to avoid dynamical contamination of the overlap function. We find that ξ_{PTS} is small and grows systematically albeit modestly as temperature is lowered. The spatial range of the thermodynamic overlap functions and extracted ξ_{PTS} are clear discriminators of dynamical behavior, even when simple structural features such as pair distribution functions are blind to differences in relaxation times. We find that in the cases studied here, ξ_{PTS} correlates reasonably well in absolute terms with the relaxation times in all three systems. Future work will be devoted to assessing if these correlations robustly hold over a wider range of temperatures and systems, as well as connecting the results uncovered here to other recent work on non-trivial structural and thermodynamic markers of glassy behavior [49, 51, 60].

2.5 Acknowledgments

This research was performed on the following computing resources provided by the National Science Foundation (NSF), National Institutes of Health (NIH), and Depart of Energy (DOE) Office of Science: the Open Science Grid (supported by the NSF and DOE) and EngageVO (NSF Grant No. OCI-0753335), the PADS (NSF Grant No. OCI-0821678) and Beagle (NIH Grant No. S10-RR029030-01) systems at the Computation Institute, a joint institute of Argonne National Laboratory and the University of Chicago, and the Extreme Science and Engineering Discovery Environment (XSEDE, NSF Grant No. OCI-1053575). I thank Michael Wilde and the Swift development team for discussions and advice on using the Swift parallel scripting language [64] to facilitate the very large number of simulations that were performed on this diverse set of resources for this investigation. I thank Bruce J. Berne, Ludovic Berthier, Giulio Biroli, Chiara Cammarota, Andrea Cavagna, Daniele Coslovich, Tomàs Grigera, Robert Jack, Walter Kob, and Paolo Verrocchio for helpful conversations.

2.6 Supplemental information

2.6.1 System details

The LJ model is an 80:20 binary mixture of Lennard-Jones spheres with size and interaction parameters given by $\sigma_{AB}/\sigma_{AA} = 0.8$, $\sigma_{BB}/\sigma_{AA} = 0.88$, and $\epsilon_{AB}/\epsilon_{AA} = 1.5$, $\epsilon_{BB}/\epsilon_{AA} = 0.5$ [54]. The WCA system is characterized in the same way, but the interaction potential is shifted up by ϵ_{ij} and cut off at $r = 2^{1/6}\sigma_{ij}$ [39]. The IPL system is characterized by an inverse-power law potential given by $V(r_{ij}) = A\epsilon_{ij}(\sigma_{ij}/r_{ij})^n$ with $n = 15.48$ and $A = 1.945$ and the same size and energy parameters as the LJ system. All quantities are reported in standard reduced Lennard-Jones units, and all systems are studied at number density $\rho = 1.2$ [38].

Radial distribution functions have been generated for the three models at the temperatures studied in the main text. A figure showing these correlations for most of the temperatures in the relevant temperature regime can be found in Fig. 2.4. Though differences do exist between the $g(r)$'s at all temperatures, the differences stay relatively constant and are small. We do not attempt to demonstrate that these differences are too small to account for dynamical differences observed between the models, as this has already been discussed in prior work [55].

2.6.2 Simulation details

Eight independent configurations of 4050 particles were equilibrated at each temperature of interest for each system using Swap-MC [57]. Six locations were chosen randomly in each of the eight independent configurations and particles whose centers fell outside a sphere of a given radius were frozen. This was done with the condition that the ratio of particle types and the density within a sphere of a given size matched that of the bulk. In order to ensure this, radii were defined by the total number of particles inside that spherical cavity i.e. $R = (\frac{3N}{4\pi\rho})^{1/3}$ with N the number of particles and ρ the bulk density. Moves that took a particle outside of the cavity were rejected (although without this restriction, particles

escaped only rarely and usually returned immediately). The overlap (averaged over the 48 independent cavities) was monitored as a function of time until reaching a plateau. This plateau value was extracted through a fit to a shifted stretched exponential and the long time limit was taken as the thermodynamic overlap. Error in this value was estimated by bootstrapping a distribution of curves to fit [65].

As in Ref. [37], we use 125 boxes (a 5x5x5 cube) to probe the overlap. In Ref. [37], the authors choose $l^3 = 0.062876$ which they found was small enough to prevent two particles from appearing in the same box at number density $\rho = 1$. Our systems studied were at $\rho = 1.2$ so we chose to use box sizes approximately 1.2 times smaller, or $l^3 = 0.05$. The bulk overlap for our systems is therefore $\rho l^3 = 0.06$.

2.6.3 PSA details

In the Particle Size Annealing (PSA) method, the interaction between particles is adjusted such that $\sigma_{ij} \to \frac{\lambda_i \sigma_{ij} + \lambda_j \sigma_{ij}}{2} = \frac{\lambda_i + \lambda_j}{2} \sigma_{ij}$. Each fixed particle outside of the cavity is assigned $\lambda_i = 1$ and each cavity particle is assigned a λ_i based on some tunable switching function. The switching function we employ is given by $\lambda(t) = \lambda_0 + (1 - \lambda_0)\left[1 - (1 - (t/\tau_s))^\gamma\right]$ where λ_0 is the smallest particle size, τ_s is the time over which switching occurs and γ controls the steepness of the curve. For our purposes, we empirically chose to run at $\lambda_0 = 0.6$ for several bulk τ_α, and then to anneal with $\gamma = 4$ and τ_s ten times longer than the length of the randomization phase. These simulations are run using the Swap-MC algorithm because for $\lambda(t) < 1$, many swap moves are accepted and this greatly enhances sampling. Because these data are noisier than the thermodynamically averaged overlap from an equilibrium simulation (due to the fact that only the 48 initial cavity configurations exist for reference), two PSA simulations were run per cavity. These data were logarithmically binned and averaged across all of the cavities for a given system and temperature. The cavity overlap was taken by fitting the plateau of this curve to a horizontal line.

2.6.4 Fits and extraction of a length

Here we comment on the fitting form chosen for extracting a length from the overlap data and report the resulting fit parameters. The authors of Ref. [37] find that a compressed exponential form $\tilde{q}(R) = A\exp(-\left(\frac{R}{\xi_{PTS}}\right)^{\eta})$ fits their low temperature data well. However, they fix $\eta = 1$ to get good fits to their higher temperature data, resulting in a sharp jump in the lengths extracted. Physically, we do not expect their fitting form (rather, any fitting form) to hold for all $R > 0$ given that the overlap quantity is not well defined for very small cavities. We expect that when $R = 1$, i.e. the cavity radius is approximately the size of a large particle "diameter", to have a cavity with about one particle on average. For a cavity of this size, we would expect an overlap between zero and one, and moreover we predict this value to be approximately temperature independent and devoid of information related to emergent amorphous order. By still fitting our data to a compressed exponential, but shifting it to start at $R = 1$, it was found that the form $\tilde{q}(R) = A\exp(-\left(\frac{R-a}{\xi_{PTS}}\right)^{\eta})$ with $a = 1$ fits all of the data at all temperatures given a fixed A value in the range $(0.45 - 0.6)$. Thus a two parameter fit to all of the data becomes viable. By sweeping the value of A in this range, it was found that $A = 0.5$ fits the data best across the three models, though slightly better fits could be done by picking a different A for each model. We chose to use the same A value for all three models, because we felt this resulted in a value of ξ that was more equivalent when comparing the models and because this decreases the possibility of spurious overfitting. From an alternative perspective one sees by plugging in $\tilde{q}(\xi+1) = 0.5/e$ that our fit form is reporting as a length the cavity size where $\tilde{q}(R+1) \approx 0.18$ (again motivated by the physical argument that nontrivial amorphous order sets in at scales $R > 1$). Hence this definition could be used independently of fit form if an alternative function were determined to fit the data better.

Given this flexibility in method for extracting the length, we do not attempt to ascribe meaning to the fit parameter η or to the exact magnitude of ξ_{PTS}. Nevertheless, we show in Fig. 2.5 that generally the same qualitative conclusions can be drawn for η as for ξ_{PTS}, namely that the η values can distinguish the LJ and IPL from the WCA at a given temperature but

	LJ		IPL		WCA	
Temp	ξ	η	ξ	η	ξ	η
1.0	1.067 ± 0.005	1.599 ± 0.019	1.177 ± 0.003	1.667 ± 0.012		
0.9	1.243 ± 0.002	1.853 ± 0.009	1.305 ± 0.002	1.787 ± 0.010	0.986 ± 0.003	1.469 ± 0.010
0.8	1.427 ± 0.002	2.008 ± 0.014	1.466 ± 0.001	2.002 ± 0.000	1.077 ± 0.002	1.530 ± 0.006
0.7	1.620 ± 0.002	2.331 ± 0.014	1.581 ± 0.119	2.668 ± 0.984	1.255 ± 0.003	1.778 ± 0.011
0.65	1.770 ± 0.003	2.050 ± 0.013	1.865 ± 0.002	2.303 ± 0.013	1.322 ± 0.002	1.783 ± 0.007
0.6	1.949 ± 0.002	2.329 ± 0.011	1.940 ± 0.003	2.594 ± 0.014	1.423 ± 0.003	1.858 ± 0.011
0.55	2.055 ± 0.002	3.119 ± 0.017	2.108 ± 0.002	3.332 ± 0.016	1.502 ± 0.003	2.070 ± 0.015
0.5					1.679 ± 0.002	1.992 ± 0.001
0.45					1.884 ± 0.002	2.755 ± 0.014
0.4					2.161 ± 0.003	2.527 ± 0.013

Table 2.1: Values extracted from fitting as a function of temperature $\tilde{q}(R) = 0.5 \exp\left(\frac{R-1}{\xi}\right)^{\eta}$ for the three systems studied. Errors are calculated as discussed in the text of the supplemental information.

collapse when scaled to the onset temperatures. However, there is much more noise in the η values as extracted. As stated earlier, the errors in the fit parameters were determined by generating a bootstrap distribution of $\tilde{q}(R)$ curves from the 48 standard $\tilde{q}(R,t)$ or 96 PSA $\tilde{q}(R,t)$ data and calculating the standard deviation of that distribution [65].

We report the fit values obtained using the methods discussed in this section in Tab. 2.1.

2.6.5 Computational details

The computations above comprised approximately 30000 independent tasks broken into hundreds of thousands of jobs, totaling more than two million hours of computational time. They were executed in parallel on resources provided by the University of Chicago Computation Institute, the Open Science Grid, and the Extreme Science and Engineering Discovery Environment. These resources were leveraged by expressing the simulations in the Swift parallel scripting language [64]. Example Swift code for this project can be found in Ref. [64].

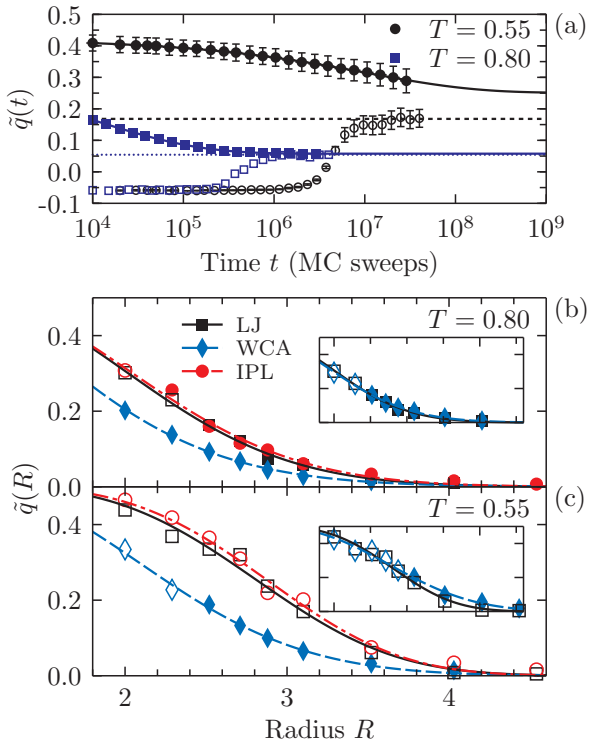

Figure 2.2: (a) Overlap as a function of MC sweeps is shown for cavity size $R = 3.1$ at two different temperatures. Filled symbols show the overlap from MC dynamics and solid lines show stretched exponential fits to this data. Open symbols show the overlap from PSA, and dashed and dotted lines show horizontal fits to the long time plateau. Note that the overlap from PSA and MC dynamics do not meet at the lower temperature. In PSA, the particles have reduced diameters and may sample many more configurations than when they are full-sized, thus the PSA data go below the bulk value at short times. Error bars are from a bootstrap analysis and for the higher temperature are substantially smaller than the symbols shown. (b), (c) Overlap as a function of cavity size at two different temperatures. Here, closed symbols show standard overlaps, open symbols overlaps from PSA. Lines through the data are compressed exponential fits with the form discussed in the text. The LJ system is represented by solid lines, the WCA dashed, and the IPL dash-dotted. The insets show the same LJ data from the main figure with the same axis limits. Overlaid are data from the WCA system at which the length is most similar — $T = 0.6$ in (b) and $T = 0.4$ in (c). Bootstrap errors are, at largest, the size of the symbols shown.

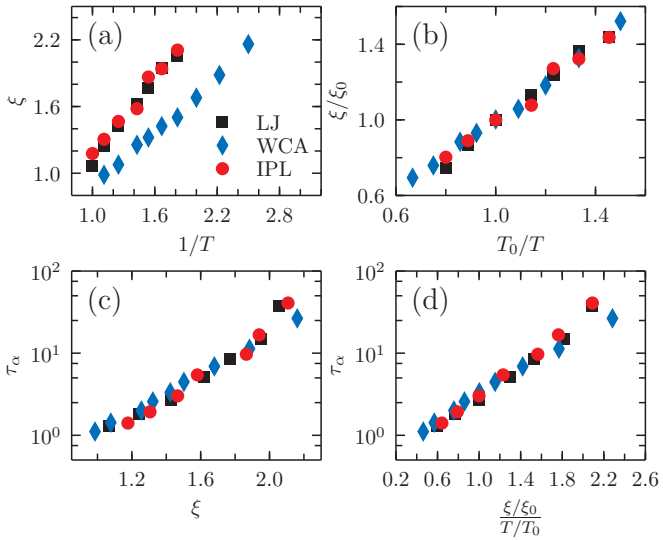

Figure 2.3: (a) Length vs. inverse temperature. For clarity, ξ here represents ξ_{PTS} of the text. A clear distinction of scale between the WCA system and the other two systems should be noted. (b) The same data as in (a) but scaled to a temperature where all three models have the same length, $T_0 = 0.8$ for the LJ and IPL and $T_0 = 0.6$ for the WCA. Here the length ξ_0 is ≈ 1.4. (c) Structural relaxation time τ_α vs. length ξ. The length scale correlates directly with the relaxation time scale. (d) Structural relaxation time vs. reduced length over reduced temperature. T_0 and ξ_0 are the values giving collapse in (b). Error bars from our bootstrap analysis are approximately the size of the data symbols. All data are reported in Sec. 2.6.

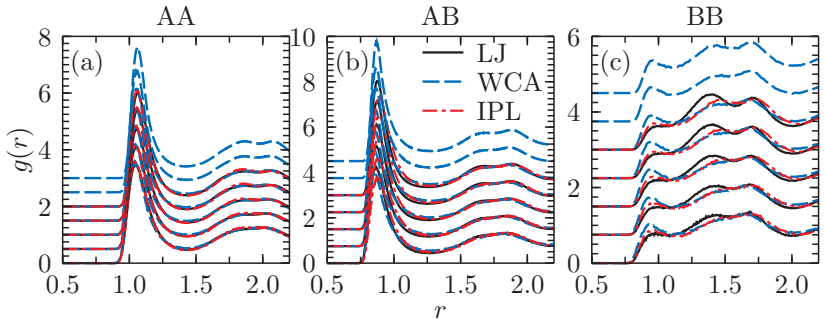

Figure 2.4: Radial distribution function for the three models. Shown are temperatures $T = \{0.9, 0.8, 0.7, 0.6, 0.55\}$ for all models and also $T = \{0.5, 0.4\}$ for the WCA model. Lines are shifted for clarity by 0.5 in panel (a) and by 0.75 in panels (b) and (c). The highest temperatures are at the bottom.

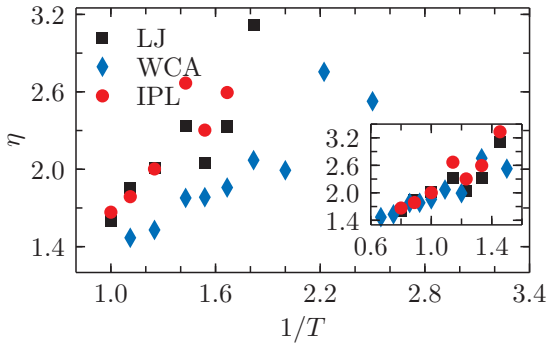

Figure 2.5: Fit parameter η as a function of inverse temperature. Inset: η plotted against scaled inverse temperature where the scaling is as in Fig. 3(b).

Chapter 3

A small subset of normal modes mimics the properties of dynamical heterogeneity in a model supercooled liquid[1]

3.1 Introduction

Understanding the formation of glass from a slowly cooled liquid remains one of the great unsolved problems in condensed matter science [1, 2, 66]. The lack of an obvious change in symmetry and the fact that the transformation does not occur at a well-defined thermodynamic critical point renders the problem of vitrification more difficult to describe than crystallization. Despite this challenge, many aspects of glass formation appear to be generic and not tied to the specific details of the liquid under investigation. In particular, the phenomenology of dynamical heterogeneity [4], which includes growing dynamical length scales, violations of the Stokes-Einstein relation, and prominent non-Gaussian displacements in the

[1] Adapted from the work published in J. Chem. Phys. 138, 12A537 (2013), in the "Special Topic Issue on the Glass Transition".

tails of real-space distribution functions, provides a framework upon which theories of the glass transition must be based [8].

A problem that bares some similarity with the standard laboratory glass transition is the jamming transition of hard spheres [2, 8, 67, 68]. Here, slow compression of the system may lead to the formation of a disordered solid. This problem is simpler than the vitrification of typical liquids in the sense that a single control variable, the packing fraction, unambiguously tunes the transition upon approach to an amorphous configuration with a maximally allowed density. While the relationship between the standard glass transition and the jamming transition is currently vigorously debated [69–71], it is clear that many aspects of the behavior of supercooled liquids and suspensions close to the jamming transition share important similarities. In particular, jamming systems display the hallmarks of dynamical heterogeneity first exposed in finite temperature fluids [72–74].

One approach that has been useful in both the study of supercooled liquids and the jamming transition invokes the notion of soft modes [75–78]. Soft modes represent a subset of the low frequency harmonic or quasi-harmonic displacements of particles around metastable configurations [79, 80]. Within traditional mean-field theories of glassy liquids, soft modes characterize the motion that involves relaxation of groups of particles when marginally metastable states first appear [2, 81–83]. Jamming systems provide a concrete case where such modes play a prominent role. In particular, numerical simulations provide clear indications of *diverging length scale* connected to the jamming transition associated with soft modes [75]. In addition, soft modes appear to play a critical role in defining the mechanical stability of athermal packings close to jamming [84, 85]. Currently the evidence for a primary role played by soft modes in the jamming transition is more extensive than it is for vitrification in thermal systems.

Despite the aforementioned lack of clarity of the role played by soft modes in supercooled liquids, interesting correlations between dynamics and soft modes in such systems have been uncovered via computer simulations. In a pioneering set of studies, Harrowell and coworkers defined the "isoconfigurational ensemble" as a means of quantitatively assessing

the influence of structure on subsequent dynamics [86–88]. These studies revealed that regions that were quantifiably "softer" than average were more likely to be involved in large amplitude dynamically heterogeneous motion when averaged over many independent simulations [86–88]. Later it was demonstrated that the real space properties of the inherent structure normal modes correlate closely with dynamical heterogeneities and irreversible configurational rearrangements [89–92]. Such connections have also been demonstrated in experiments performed on colloidal suspensions [93–96]. It remains unclear in the examples discussed above if the harmonic soft modes are an active player in the dynamics or if they are spectators whose positions correlate with regions of dynamical activity but which do not influence particle relaxation.

With an appropriate definition of normal modes emerging from the free energy landscape of hard spheres, Brito and Wyart have shown that dynamical heterogeneity in jamming systems also correlates with low frequency modes [84]. They have demonstrated that relaxation events in simulated hard spheres proceed along a small number of mode directions. Further, they have explicitly demonstrated that the number of such directions systematically decreases as the jamming threshold is approached [85, 97]. The purpose of this study is to explore the possibility that a similar effect may occur in *thermal* systems as temperature is lowered, even in the absence of an analog of the jamming threshold where the correlation length associated with soft modes diverges.

The paper is organized as follows. In Section 3.2 we will present the details of the two-dimensional glass forming liquid that we study here. In Section 3.3 we will review the notion of inherent structures (IS) and IS trajectories, and present relevant properties of the IS trajectories for our model. In Section 3.4 we will discuss normal modes (NM), the NM properties of our system, and the decomposition of IS transitions onto a basis of modes. In Section 3.5 we will discuss the quantitative results of the decomposition procedure just described, and finally in Section 3.6 we will summarize our results and frame them in a broader context.

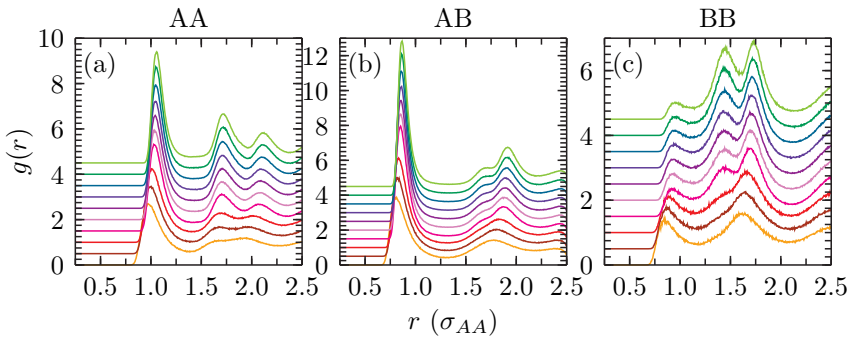

Figure 3.1: Radial distribution functions for the 2D 65:35 Kob-Andersen Lennard-Jones system at $\rho = 1.2$. Temperatures are $T = \{5.0, 3.0, 2.0, 1.0, 0.9, 0.8, 0.7, 0.6, 0.5, 0.45\}$ from bottom to top. Each $g(r)$ is shifted up by 0.5 from that of the preceding temperature for clarity.

3.2 Model details

We study the two dimensional "65:35" Kob-Andersen binary Lennard-Jones mixture [98]. In brief, it is characterized by the parameters $\sigma_{AB} = 0.8\sigma_{AA}$, $\sigma_{BB} = 0.88\sigma_{AA}$, $\epsilon_{AB} = 1.5\epsilon_{AA}$, and $\epsilon_{BB} = 0.5\epsilon_{AA}$, with 65% of the particles being of type A. All particles have unit mass. Time scales are reported in Lennard-Jones units with $\tau = \sqrt{m\sigma_{AA}^2/\epsilon_{AA}}$ and we fix the number density at $\rho = 1.2$. All interactions were shifted and cut off at $r_{ij} = 2.5\sigma_{ij}$. This model has been used previously because it resists crystallization in two dimensions better than the standard 80:20 variant [98, 99]. To our knowledge, structural and dynamical quantities for this system have not been previously reported. Here, for completeness, we briefly discuss these properties for $N = 1000$. In Fig. 3.1 we present the radial distribution functions for a series of temperatures that span the high and supercooled temperature regimes. In Fig. 3.2(a) we show the self-part of the intermediate scattering function for the A-type particles, $F_s^A(k = 6.28, t)$, as well as the α relaxation times as defined by $F_s(k = 6.28, t = \tau_\alpha) = 1/e$. These values are also reported in Table 3.1. Finally, in Fig. 3.2(b) we also show that time-temperature superposition appears to hold in the β-regime in a manner comparable to the 3D, 80:20 variant of Ref. [36].

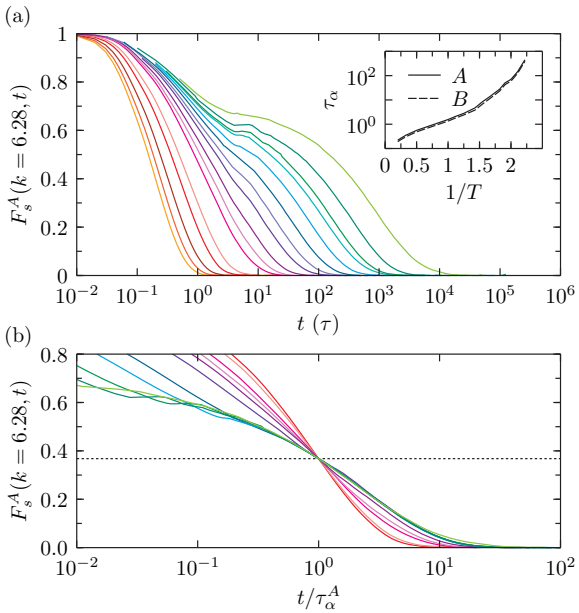

Figure 3.2: (a) Self-intermediate scattering function for A type particles from NVE molecular dynamics at the temperatures listed in Table 3.1, appearing from left to right. Inset: Alpha-relaxation times for both A and B type particles, with data given in Table 3.1. (b) $F_s^A(k=6.28,t)$ with the horizontal axis scaled by the alpha relaxation time τ_α^A. The curves collapse in the β-regime (the shortest times shown, where the correlation function has plateaued) as the temperature is lowered. The highest three temperatures are not shown. The dotted line shows the value $1/e$.

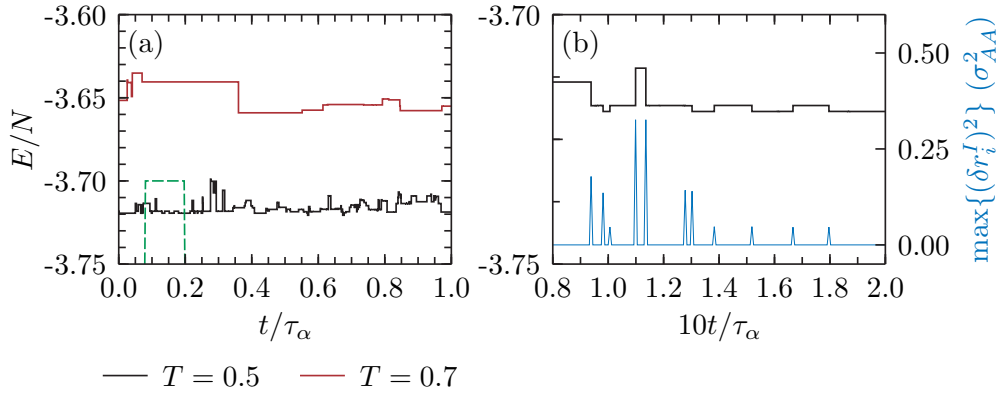

Figure 3.3: (a) Inherent structure energies (per particle) at $T = 0.7$ (above) and $T = 0.5$ (below), plotted as a function of time scaled by the alpha relaxation time τ_α at that temperature. Transitions occur between extended plateaus at both temperatures; they occur less frequently on an absolute time scale at the lower temperature but more frequently relative to the alpha relaxation time. The dashed box shows the area plotted in (b). (b) Above is a magnified look at the transitions at $T = 0.5$, with energies per particle shown on the left. Below are the maximum squared displacements between subsequent inherent structures, with values shown on the right. Note every energy transition has a structural difference as measured by maximum squared displacement, and there is an additional transition at $10t/\tau_\alpha \approx 1.28$ not visible in the energy trace.

T	τ_α^A	τ_α^B	τ_α	dt	T	τ_α^A	τ_α^B	τ_α	dt
5.000	0.22	0.19	0.20	0.001	0.700	4.70	3.81	4.21	0.003
4.000	0.27	0.23	0.25	0.001	0.650	8.10	6.51	7.35	0.003
3.000	0.36	0.31	0.33	0.001	0.600	13.9	11.5	12.7	0.003
2.000	0.56	0.49	0.52	0.001	0.550	27.5	22.9	25.3	0.004
1.500	0.79	0.70	0.73	0.002	0.525	50.1	42.1	46.0	0.004
1.000	1.56	1.35	1.45	0.002	0.500	70.1	59.3	64.8	0.005
0.900	2.06	1.76	1.91	0.002	0.475	145	124	135	0.005
0.800	2.80	2.40	2.60	0.002	0.450	449	388	418	0.005

Table 3.1: Alpha relaxation times (τ_α) for the 2D, 65:35 Kob-Andersen system, with $N = 1000$. τ_α is reported for A and B type particles, as well as for all particles together. Also listed for reference are integration time-steps used both in annealing the configurations and in generating inherent structure trajectories.

3.3 Inherent dynamics

The motion of particles in a supercooled liquid is extremely complex, and the ability of a single particle to change its current position is dependent on the interplay of fluctuations on many length scales. The notion of inherent structures (IS) has been developed as an aid to simplify the description of both structural and dynamical processes in supercooled liquids [100–102]. In the IS framework, the motion of the system as a whole is decomposed into transitions between local minima on the global potential energy surface (the "inherent structures") and the vibrations around these configurations. Each glassy configuration is then associated with the configuration which is the "closest" minimum, analogous to how one might associate a solid's configuration with a periodic crystal structure, ignoring thermal fluctuations. Here, "closest" is a practical definition meaning the structure obtained by a local energy minimization technique. A temporal series of IS generated by quenching a trajectory from a molecular dynamics simulation is termed an IS trajectory. Studies of these

trajectories have provided interesting insights into the *true* dynamics in glassy systems, for example, revealing the presence and nature of string-like cooperative motion [19, 103, 104].

For this study, we will require IS trajectories at a series of decreasing temperatures. Specifically, configurations of 250 particles each were generated using NVT dynamics in LAMMPS by annealing through the series of temperatures in Table 3.1, simulating for over $100\tau_\alpha$ (as calculated for $N = 250$) at the lower temperature for each subsequent annealing step [105]. Each resulting configuration was then simulated for an additional $100\tau_\alpha$, and $F_s(k,t)$ was calculated for that entire trajectory, as well as for the first and second halves. At the lower temperatures, signs of aging were obvious in the majority of these simulations; only those configurations resulting in a simulation that showed little or no difference in dynamics between the first and second half of the trajectory were used for subsequent analysis. At all temperatures, we obtained at least 20 independent configurations for future study. The integration time steps used throughout this Chapter are reported in Table 3.1.

For each of these independent configurations, IS trajectories were generated by quenching configurations from molecular dynamics simulations using steepest descent minimization. Our system is quite small, rendering the IS meaningful in concept and easy to identify. Specifically, trajectories of length 100,000 integration steps were generated at each temperature, saving every configuration, except at $T = 0.45$ where it was necessary to run 200,000 and save every 2 steps to obtain a comparable level of statistical accuracy. We generated IS trajectories using a bisection technique similar to that of Ref. [104]. A small number of configurations evenly spread throughout the trajectory were quenched to a local minimum. If two adjacent configurations differed (see next paragraph for more details), then we bisected that time interval and quenched the configuration halfway between the two endpoints. This procedure was iterated until a sequence of configurations was generated in which all transitions between minima occurred at the time scale of a single integration time step.

For every configuration in the new IS trajectory, we monitored both the energy and the displacement from the previous configuration. We calculated both the mean square displacement $\langle \Delta \mathbf{R}^2_{IS}(t_i) \rangle = \frac{1}{N} \sum_{j=1}^{N} |\mathbf{r}^I_j(t_i) - \mathbf{r}^I_j(t_{i-1})|^2$ and maximum squared displacement

$\max\{(\delta\mathbf{r}_i^I)^2\} = \max_{1\leq j\leq N}\{|\mathbf{r}_j^I(t_i) - \mathbf{r}_j^I(t_{i-1})|^2\}$ where t_i is the time index of the i'th inherent structure, $\mathbf{r}_j^I(t_i)$ is the position of particle j in inherent structure i, and N is the total number of particles. We find that these two quantities are correlated and significant changes in one always occur in the other simultaneously.

A plot of the IS energy, as displayed in Fig. 3.3(a), reveals a series of plateaus as in previous works [104, 106–108]. Differences in energy within these plateaus are on the order of 10^{-6} per particle or smaller. However, as discussed by Schrøder, *et al.*, there is the small probability that a change in structure occurs between two configurations with a vanishingly small difference in energy [104]. Hence, as in that previous work, we will identify changes in inherent structure by the difference in positions and not by energy. We used $\max\{(\delta\mathbf{r}_i^I)^2\}$ for this purpose but emphasize that choosing the mean square displacement would produce identical results. For the model studied here, we find that maximum squared displacements in the range of 10^{-5} to 10^{-2} are very rare. We therefore empirically choose a threshold value within this range and deem that whenever $\max\{(\delta\mathbf{r}_i^I)^2\} > 0.001$, a transition has occurred. The correlation between changes in structure and changes in energy is illustrated in Fig. 3.3(b).

It will be most important in future discussion to quantify the degree of localization of motion in an IS transition (or a normal mode, see Sec. 3.4). The metric we shall use is the standard participation ratio. For a vector quantity $\mathbf{v}$ of length dN such as the displacement field, the vector can be organized as a matrix $\mathbb{V}$ of size $N \times d$ where each row $1 \leq i \leq N$ contains a quantity pertaining to particle i. With these quantities, the participation ratio is defined as [80],

$$P(\mathbf{v}) \equiv \left[N \sum_{i=1}^{N} (\mathbb{V}_i \cdot \mathbb{V}_i)^2\right]^{-1}. \tag{3.1}$$

We use this definition to calculate the participation ratio of transitions $P(\Delta\tilde{\mathbf{R}}^I(t_i))$ at each temperature. Nearly all participation ratios fall in a range from 0 to 0.6, with just a few occurring with values larger than 0.6. As a matter of nomenclature only, we will refer to transitions with $P(\Delta\tilde{\mathbf{R}}^I(t_i)) > 0.3$ as "extended", and all others as "localized". A histogram is shown in Fig. 3.4. As the temperature is lowered, transitions with low participation ratio

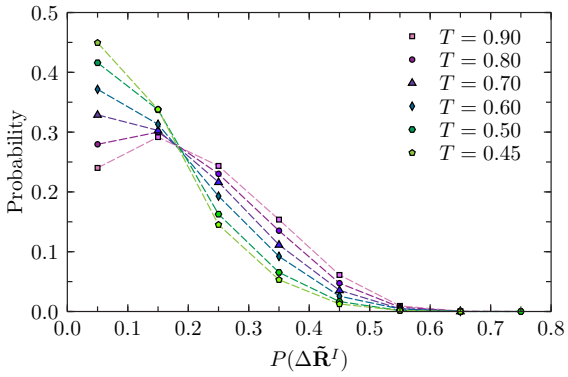

Figure 3.4: At each temperature studied, the proportion of inherent structure transitions histogrammed into bins of size $P(\Delta\tilde{\mathbf{R}}^I) = 0.1$. At high temperatures there are significantly more "extended" transitions than at low temperatures. Dashed lines are a guide to the eye. Note that calculations on transitions with $P(\Delta\tilde{\mathbf{R}}^I) \geq 0.55$ such as those in Figs. 3.9 and 3.10 may be skewed due to poor statistics, but this does not affect any of our conclusions.

become much more prevalent i.e. motion is increasingly localized. Interestingly, the curves intersect for participation ratio ≈ 0.17, although the meaning of this coincidence is unclear. An illustration of the types of IS transitions is shown in Fig. 3.6.

3.4 Normal modes

Suppose a transition in a given IS trajectory is found to occur at time t_i. We wish to study the relationship between the normal modes of configuration $\mathbf{R}_{IS}(t_i)$ and the transition $\mathbf{R}_{IS}(t_i) \rightarrow \mathbf{R}_{IS}(t_{i+1})$. To do this, we construct the Hessian or dynamical matrix for configuration $\mathbf{R}_{IS}(t_i)$ given by the matrix of second derivatives of the potential V, [89]

$$\mathbb{H}(t_i)_{jk} = \frac{\partial^2 V(\mathbf{R}_{IS}(t_i))}{\partial \mathbf{r}_j^I \partial \mathbf{r}_k^I}. \tag{3.2}$$

Normal modes are the eigenvectors obtained by diagonalization of this matrix. It is well known that the normal modes form a complete orthonormal basis for the motion of this configuration. For configuration i the eigenvectors can be ordered by eigenvalue and will be denoted $\{\mathbf{e}_j^i\}$. For a d-dimensional configuration of N particles, $\mathbf{e}_j^i$ will be a vector of length

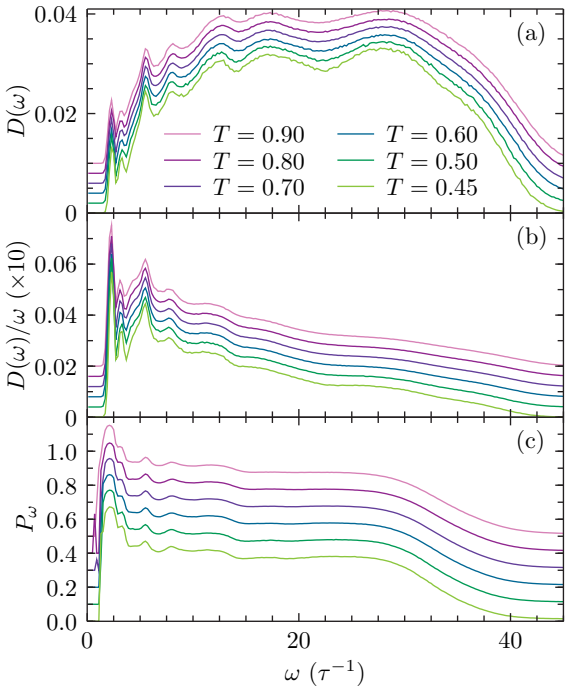

Figure 3.5: (a) Density of states for the 2D Kob-Andersen model with $N = 250$ at the series of temperatures shown. Curves are shifted up by 0.002 from the temperature below for clarity, the lowest temperature being at the bottom. (b) The same as (a) but the density of states has been divided by frequency, and scaled up by a factor of 10 for clarity. (c) Participation ratio as a function of frequency for the same series of temperatures as in (a). Curves are shifted up by 0.1 from the temperature below for clarity. Quantities in (a) and (b) are binned to a resolution of $0.2\tau^{-1}$.

dN and there will be dN eigenvectors, of which d will correspond to translational modes with eigenvalue 0. The Hessian is real and symmetric and hence the eigenvalues and eigenvectors are real. The density of states (DOS) $D(\omega)$ is a histogram of frequencies obtained from the eigenvalue spectrum, and is plotted for our system at a series of temperatures in Fig. 3.5(a). The same histogram is shown with the DOS divided by a factor of ω in Fig. 3.5(b) so that one can identify the so-called "boson peak", where the number of low frequency modes exceeds the Debye prediction of ω^{d-1} [76].

The displacement vector for a transition is given by $|\Delta\mathbf{R}^I(t_i)\rangle = |\mathbf{R}_{IS}(t_i)\rangle - |\mathbf{R}_{IS}(t_{i-1})\rangle$, and characterizes the inherent structure transition. For convenience, we will consider instead

the normalized displacement vector defined as $|\Delta\tilde{\mathbf{R}}^I(t_i)\rangle = \Delta\mathbf{R}^I(t_i)/\sqrt{\langle\Delta\mathbf{R}^I(t_i)|\Delta\mathbf{R}^I(t_i)\rangle}$. This can be projected onto a normal mode basis as,

$$|\Delta\tilde{\mathbf{R}}^I(t_i)\rangle = \sum_{j=1}^{dN} c_j^k(i)|\mathbf{e}_j^k\rangle. \tag{3.3}$$

Note that we label the eigenvectors with configuration index k to emphasize that these need not be the eigenvectors corresponding to time t_i. The coefficients $c_j^k(i)$ above are obtained through the orthonormality condition for the basis

$$\langle\mathbf{e}_j^k|\Delta\tilde{\mathbf{R}}^I(t_i)\rangle = \sum_{l=1}^{dN} c_l^k(i)\langle\mathbf{e}_j^k|\mathbf{e}_l^k\rangle = c_j^k(i). \tag{3.4}$$

Since $|\Delta\tilde{\mathbf{R}}^I(t_i)\rangle$ is normalized, its squared norm can be written as

$$1 = \langle\Delta\tilde{\mathbf{R}}^I(t_i)|\Delta\tilde{\mathbf{R}}^I(t_i)\rangle = \sum_{j=1}^{dN} |c_j^k(i)|^2. \tag{3.5}$$

We will refer to $|c_j^k(i)|^2$ as the *contribution* of mode j of basis k to transition i. These contributions can be ordered from highest to lowest in numerical value.

In order to get an idea of how much each mode contributes to a transition, we consider the quantity $N_{1/2}$, which is defined to be the smallest number of modes necessary to reproduce 50% of a given transition. We will also report $F_{1/2}$, the fraction of all modes necessary to reproduce 50% of the motion, which has been used previously [85, 97]. In general we can also define the quantities N_f and F_f where f is a fraction other than 0.5. To provide a unique definition of these quantities, we take $\{o_l^k(i)\}$ as a monotonically decreasing sequence of ordered contributions to transition i from basis k and then generate the cumulative series $s_m^k(i) = \sum_{l=1}^m o_l^k(i)$. Then

$$N_f^k(i) = \min\{m|s_m^k(i) > f\} \tag{3.6}$$

and $F_f^k(i) = N_f^k(i)/(Nd)$.

The definition of participation ratio given in Eq. 3.1 also applies to the normal modes obtained via diagonalization of the Hessian. By convention, the participation ratio averaged over modes with a given frequency is referred to as P_ω. This quantity, which will play a role in our future discussion, is shown in Fig. 3.5(c) for a wide range of temperatures.

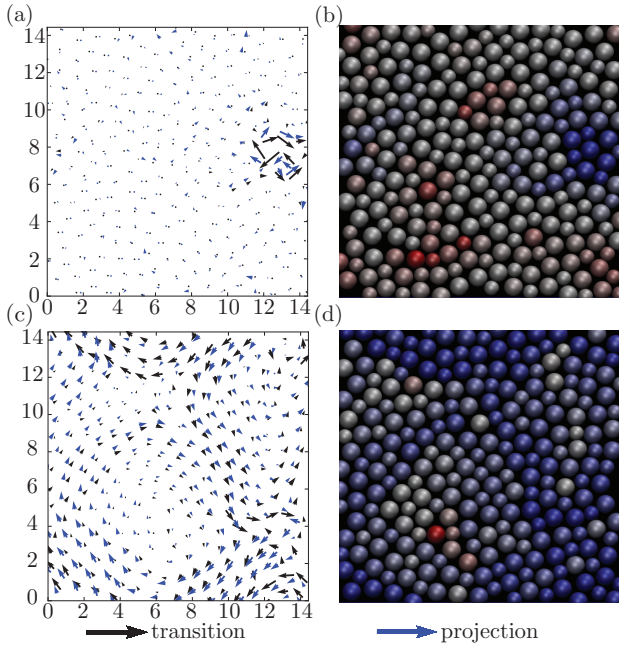

Figure 3.6: Inherent structure transitions for the 2D Kob-Andersen model with $N = 250$ at $T = 0.5$. Axis labels are simulation coordinates. (a) A "localized" transition with participation ratio $P(\Delta\tilde{\mathbf{R}}^I) = 0.04$ and $\langle(\Delta\mathbf{R}^I)^2\rangle = 0.06$. Particle displacements are shown with black arrows and a projection of the top 37 highest contributing modes, reproducing 50% of the transition is shown with blue arrows. Vectors are multiplied by a factor of two for clarity. (b) The same transition with the natural logarithm of square particle displacements $\ln((\delta\mathbf{r}^I)^2)$ represented from red at -12.5 to blue at -0.7. (c) Same as (a) but for an "extended" transition with $P(\Delta\tilde{\mathbf{R}}^I) = 0.5$ and $\langle(\Delta\mathbf{R}^I)^2\rangle = 0.2$. Here only one mode is needed to project onto 60% of the transition. (d) The same transition as (c), with $\ln((\delta\mathbf{r}^I)^2)$ ranging from -9.43 in red to -1.48 in blue.

In Fig. 3.6 we illustrate the concepts presented in this and the preceding section. Fig. 3.6(a) and (b) show an IS transition with low participation ratio, in which most of the contribution to the motion is localized to a few particles. In Fig. 3.6(c) and (d) we show an IS transition with high participation ratio, in which the motion is much more evenly spread throughout the system. In (a) and (c) we show the result of projecting the motion of an IS transition onto normal modes of the initial IS. The black arrows show the motion of the particles in the system during an IS transition, and the blue arrows show the sum of the normal modes that contribute to $N_{1/2}$ weighted by their coefficients as in Eq. 3.3. We see that for both localized and extended transitions, the degree of similarity is striking. In the single example of an "extended" transition, a single normal mode projects onto 60% of the actual displacement vector. We illustrate the opposite case with a particularly localized event, where just a few particles rearrange, and where a relatively large number of modes are needed to reproduce half of the motion compared to the average as discussed in Sec.3.5. In what follows, we use the metrics $N_{1/2}$ and $F_{1/2}$ as a quantitative measure of how faithfully a given transition may be represented by a small set of normal modes.

3.5 Results

We begin this section with a discussion of our main result. We examine the temperature dependence of the quantity $\langle N_{1/2} \rangle$ as defined in Section 3.4 (where brackets denote average over many transitions) following Brito and Wyart, who showed that this quantity decreased systematically in their system of hard spheres as the jamming transition was approached [97]. Analogously, we plot in Fig. 3.7 the identical quantity for our thermal system as a function of inverse temperature. It is clear that as our system becomes increasingly supercooled the number of normal modes needed to approximate the correlated atomic motion occurring in an inherent structure transition decreases. The degree to which this is true is independent of whether the pre- or post-transition inherent structure is used to produce the normal mode basis (which we term "forward" or "backward" transitions, respectively). This fact, which

is required if we are to interpret the mode basis as a set of directions along which reversible motion occurs on a potential energy landscape, is not entirely trivial as the modes of the two configurations are distinct.[2]

To gain some insight into the magnitude of $\langle N_{1/2} \rangle$, as well as the significance of the trend seen in Fig. 3.7, we also reconstruct the dynamical activity exhibited during inherent structure transitions with a random set of modes obtained from distant inherent structures sampled at the same temperature as the transitions under consideration. The inset of Fig. 3.7 shows that the value of $\langle N_{1/2} \rangle$ obtained from this procedure exceeds that obtained with modes associated with the actual transition by approximately one order of magnitude at the temperatures considered in our simulations. Further, as temperature is lowered, the average number of *random* modes needed to approximately reproduce the motion observed in inherent structure transitions remains constant, in stark contrast to the behavior seen when $\langle N_{1/2} \rangle$ is calculated with the modes associated with the IS transitions. In Fig. 3.8 we show that behavior illustrated in Fig. 3.7 does not depend on the choice of the threshold value f used to define the degree of overlap between the modes and the true particle motion. The behavior illustrated in Fig. 3.7 suggests that motion in mildly supercooled liquids proceeds along a successively smaller number of "soft" mode directions, a phenomena noted previously using a different definition of normal modes as hard spheres approach the jamming transition [97].

The behavior illustrated in Figs. 3.4-3.6 is, upon first consideration, contradictory with the result presented in Fig. 3.7. In particular, Fig. 3.4 shows that the motion that occurs during IS transitions becomes increasingly localized as temperature is decreased. In Fig. 3.6 we illustrate that, at least in one particular transition, it takes *more* modes to construct $\langle N_{1/2} \rangle$ for the case of a localized transition than for a delocalized one. This fact can be quantified, and we show in Fig. 3.9 that this is true on average at any temperature. Thus it is surprising that $\langle N_{1/2} \rangle$ decreases as temperature is lowered. The resolution of this conflict

[2]In fact, all quantities computed which compare modes with inherent structure transition displacement vectors were identical within error bars if computed using pre- and post-transition modes, and hence when calculating the values in Figs. 3.8-3.11 we average both sets of data for increased statistical accuracy.

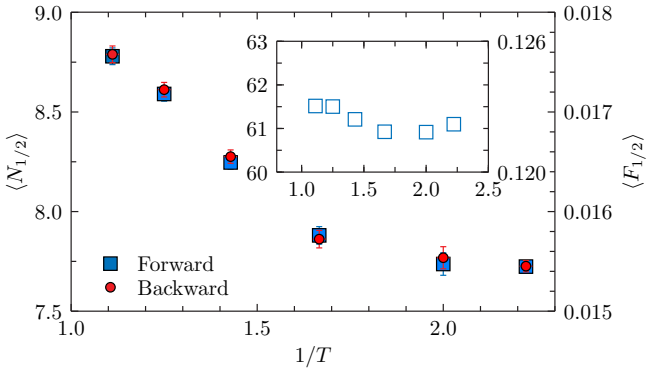

Figure 3.7: Average number of modes (left axis) or fraction of total modes (right axis) necessary to reproduce at least 50% of total particle motion in inherent structure transitions at each temperature studied. Blue squares are for transitions in the "forward" direction and red circles in the "backwards" direction as described in the main text. Error bars shown are jackknife standard errors [65]. Inset: Symbols are the values of $\langle N_{1/2} \rangle$ and $\langle F_{1/2} \rangle$ where 2000 inherent structures at each temperature are projected onto the modes from each of twenty-five random configurations from an independent IS trajectory. Note the difference in magnitude between the vertical axis of the inset and the main figure.

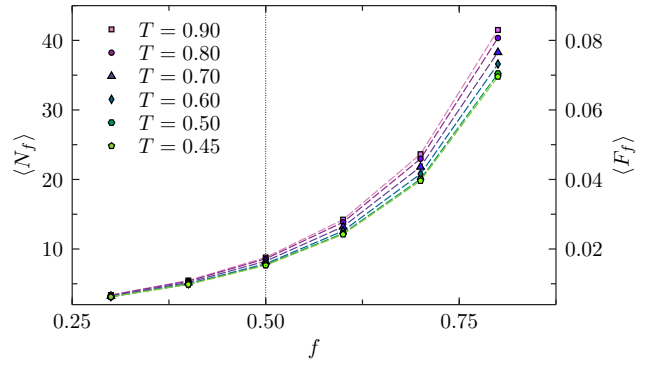

Figure 3.8: Average number and fraction of total modes necessary to reproduce a fraction f of inherent structure transitions from $f = 0.3$ to $f = 0.8$. A dotted line shows $f = 1/2$, the value focused on for most of this Chapter. A slice through this line gives the data shown in Fig. 3.7. $\langle N_f \rangle$ decreases with temperature for all values of f. Jackknife error bars are approximately the size of the symbols [65]. Dashed lines are a guide to the eye.

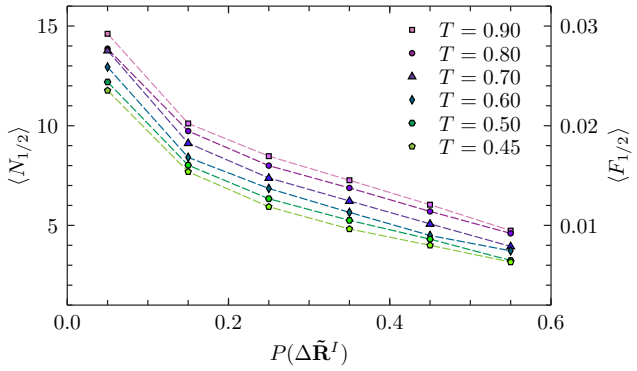

Figure 3.9: $\langle N_{1/2} \rangle$ and $\langle F_{1/2} \rangle$ for inherent structures as a function of participation ratio of IS transitions. Bins of size $P(\Delta\tilde{\mathbf{R}}^I) = 0.1$ are used. "Extended" transitions (measured by $P(\Delta\tilde{\mathbf{R}}^I)$ require fewer modes to reproduce their transitions. $\langle N_{1/2} \rangle$ and $\langle F_{1/2} \rangle$ decrease uniformly for all values of $P(\Delta\tilde{\mathbf{R}}^I)$ as temperature is lowered. Jackknife error bars are again approximately the size of the symbols and dashed lines a guide to the eye [65]. Data for $P(\Delta\tilde{\mathbf{R}}^I) > 0.55$ are not shown due to poor statistics, as seen in Fig. 3.4.

lies in the fact that the curves of $\langle N_{1/2} \rangle$ uniformly decrease for *all* types of transitions as temperature is lowered. Clearly either something in the structure of the modes or the type of particle motion occurring in IS transitions (or both) changes as temperature is lowered such that the overlap between motion and modes increases in a uniform fashion independent of the degree of localization of the transition. Any changes in the mode structure are evidently subtle, at least in terms of the common metrics shown in Fig. 3.5. In particular, since the temperature dependence of both the density of states and density of participation ratios of IS normal modes is very weak, differences must be found at the level of the small number of modes that actually contribute to $\langle N_{1/2} \rangle$ at each temperature.

While the overall features of the various densities of states are largely insensitive to the lowering of the temperature, we can show that the properties of the modes that actually contribute to $\langle N_{1/2} \rangle$ do have properties that systematically change as temperature is varied. The contributing modes are essentially confined to the low frequency band in the neighborhood of the "boson peak" (with frequencies of $10\tau^{-1}$ or smaller) at all temperatures studied. Within this band, there is a systematic shift of the frequencies of contributing modes to

lower values at lower temperatures, as illustrated in Fig. 3.10. Furthermore, for localized transitions the fraction of localized harmonic modes that contribute to $\langle N_{1/2} \rangle$ systematically increases as temperature is lowered, as shown in Fig. 3.11. Thus, as temperature is decreased the modes that contribute to $\langle N_{1/2} \rangle$ increasingly take on the character of the actual motion of particles during the IS transition.

3.6 Conclusion

The results of the previous section clearly show that dynamical heterogeneity in supercooled liquids, as exhibited by the motion of particles during IS trajectories, may be cleanly decomposed into a small number of harmonic normal modes associated with the inherent structures themselves. The fraction of Hessian eigenvectors needed to reproduce an average IS transition as quantified by $\langle N_{1/2} \rangle$ is on the order of two percent of the total number of modes and decreases as the liquid is increasingly supercooled. This decrease in the number of soft mode directions that the system follows takes place even though IS transitions become more localized. Further, we have demonstrated that this property is a nontrivial feature of the actual pre- and post-IS mode structure and cannot be reproduced by modes obtained from independent inherent structures.

This study was clearly inspired by the work of Brito and Wyart, who found similar behavior in hard-spheres as the packing fraction is varied and the jamming transition is approached [85, 97]. Our work shows that this relationship between modes and dynamical heterogeneity is similar in thermal systems where inverse temperature plays the same role as density. Interestingly, we find that for an analogous range of relaxation times, even fewer modes are needed in our study to reproduce the quantity $\langle N_{1/2} \rangle$ than needed in the hard-sphere case. This is somewhat surprising because the statically defined IS normal modes are, in a sense, cruder than the dynamically defined modes of Brito and Wyart which are associated with the free energy (as opposed to potential energy) of the system. It is still unclear if the results presented here can be taken as a feature of similarity between the

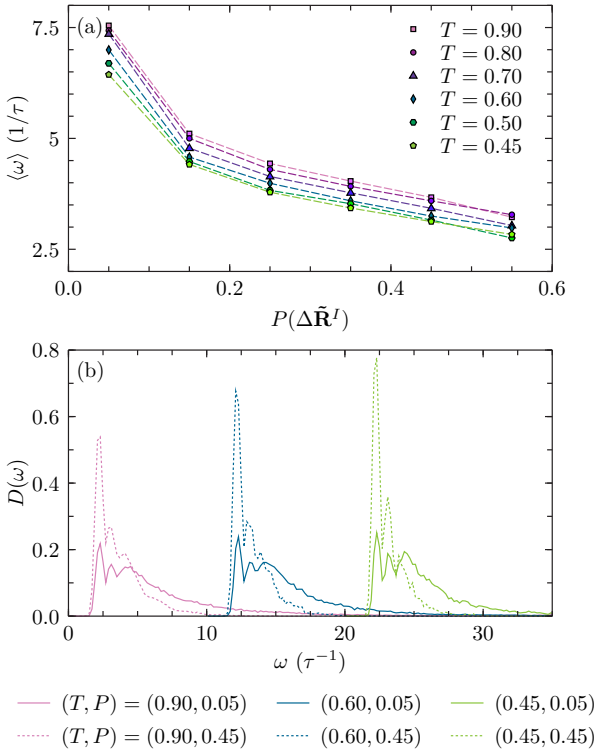

Figure 3.10: (a) Average frequency of modes contributing to $\langle N_{1/2}\rangle$ as a function of IS transition participation ratio histogrammed into bins of size $P(\Delta\tilde{\mathbf{R}}^I) = 0.1$. "Extended" transitions are made up of lower frequency modes. The frequency of contributing modes decreases with temperature for all sized transitions. Jackknife errors are smaller than the points shown [65]. Dashed lines are a guide to the eye. (b) Frequency distribution of modes used to compute $\langle\omega\rangle$ for three temperatures $T = \{0.9, 0.6, 0.45\}$, and two values of $P(\Delta\tilde{\mathbf{R}}^I) = \{0.05, 0.45\}$ (referred to as P here for convenience). Other temperatures and P values interpolate between these curves. Temperatures are shifted to the right from the temperature above by $\omega = 10$ and curves for $P = 0.45$ are dotted. We see that curves are more sharply peaked for higher P and the peak height increases as temperature is lowered.

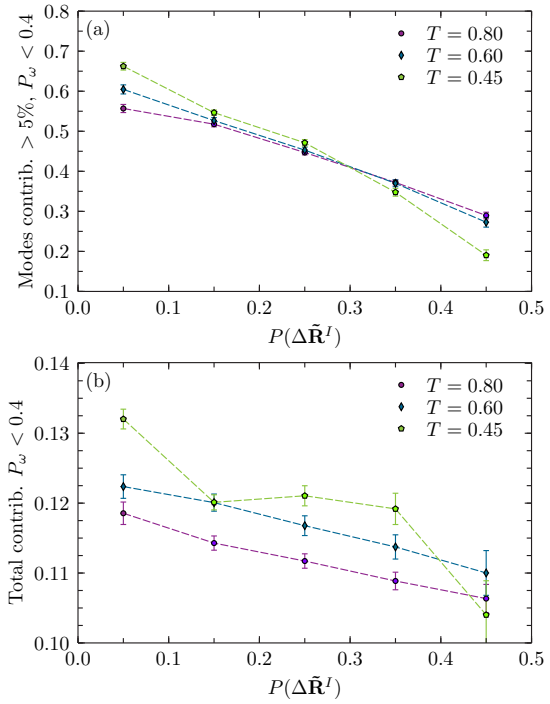

Figure 3.11: (a) Average number of modes which have a participation ratio $P_\omega < 0.4$ and which contribute more than 5% to transitions of a given type at three different temperatures. (b) For the same temperatures, average total contribution to a single transition of a given type from modes with $P_\omega < 0.4$. Error bars are jackknife standard errors [65]. Modes with low participation ratios contribute more to "localized" transitions ($P(\Delta\tilde{\mathbf{R}}^I) < 0.3$) at low temperatures than at high temperatures.

jamming and glass transitions. In particular, given the importance of marginal stability in jamming, the depletion of mode directions as a basis for motion in jamming is natural. On the other hand the role of such mechanical consideration in thermal glass-forming systems is totally unclear. One interesting possibility hinted at by the lowest temperature data point in Fig. 3.7 is that the temperature dependence of $\langle N_{1/2} \rangle$ plateaus at low temperature, perhaps close to the mode-coupling temperature of the system [82, 109, 110]. While the quality of statistics we have is not good enough to draw such a conclusion, this possibility is worthy of future scrutiny. In particular, the jamming transition is accompanied by a *divergence* of the length scale associated with mode polarization and hence the directions associated with relaxation vanish at the transition [75]. In thermal systems, this behavior is absent or averted due to other processes, leading to a possible saturation of the number of soft directions that overlap with the true relaxation of the system.

Another avenue worthy of future study concerns the degree to which the results presented here are an indication of the primacy of soft modes in the relaxation of supercooled liquids. In an interesting study, Ashton and Garrahan constructed models with mode structure by taking a standard lattice gas and connecting particles via springs with random force constants [111]. They showed that, within models where soft-modes are grafted onto kinetically constrained lattice gasses, the soft mode polarization will indeed congregate near vacancies but do not govern the motion of the defects, which instead move via local facilitated rules. Thus, in this class of models, soft modes are *passive* markers of defect structure that do not themselves participate in relaxation. It would be most interesting to repeat the exercise of decomposing the inherent structures transitions in kinetically constrained models onto the normal modes of the Ashton-Garrahan models to test if the picture of modes as passive markers is compatible with the behavior exhibited in Fig. 3.7 and the previous work of Brito and Wyart. We reserve this investigation for a future study.

3.7 Acknowledgments

This research was performed on the following computing resources provided by the National Science Foundation (NSF): the PADS resource (NSF Grant No. OCI-0821678) at at the Computation Institute, a joint institute of Argonne National Laboratory and the University of Chicago; the University of Chicago Computing Cooperative (UC3), supported in part by the Open Science Grid (NSF Grant No. PHY-1148698); and the Extreme Science and Engineering Discovery Environment (XSEDE, NSF Grant No. OCI-1053575). Simulations performed were organized by executing LAMMPS runs with the Swift parallel scripting language (NSF Grant No. OCI-1148443) [64].

Chapter 4

Crossovers in the dynamics of supercooled liquids probed by an amorphous wall[1]

4.1 Introduction

There has been a great surge in studies which seek to investigate length scales in supercooled liquids through simulation in the presence of quenched amorphous order [37, 53, 112–120]. This recent interest has been spurred on by the successful computational realization of thought experiments predicting growing static length scales on increased supercooling, as well as the ever-growing availability of CPU time which makes such studies feasible [37, 48, 53, 63, 115–120].

Yet, studies seeking to understand growing dynamical length scales by employing simulations with frozen particles go back even earlier [121, 122]. The authors of Ref. [121], in particular, studied the Kob-Andersen binary Lennard-Jones system (KA) in the presence of a rough wall created by fixing the positions of a slab of particles from a bulk equilibrium

[1] Adapted from the work published as Phys. Rev. E **89**, 052311 (2014).

configuration. They found that the dynamics near the rough wall slowed down substantially and the analysis of the profiles of relaxation times near the wall provided a length scale which grew with decreasing temperature. A recent study revisited these ideas in a supercooled harmonic sphere system (HARM) for larger sample sizes and down to very low temperatures, below the mode-coupling temperature T_c [113]. This study revealed a dynamical length scale that first increased as T approached T_c from above, and then surprisingly decreased for $T < T_c$ [113]. This behavior was attributed to a change in the dynamics below T_c where collective particle rearrangements become predominant [113, 123, 124]. Such a change is naturally understood in the framework of the random first order transition (RFOT) theory [2, 125], where a crossover between non-activated correlated relaxation to thermally activated cooperative dynamics is expected to take place.

It should be noted that the dynamical length scale defined in Ref. [113] need not correspond to that extracted from study of the bulk four-point correlation function $S_4(k,t)$, but simply defines an independent dynamic correlation length scale associated with the spatial extent of the perturbation of dynamic relaxation near an amorphous wall. Although there is a formal connection between bulk correlations and dynamic response to an infinitesimal field in the linear response regime [126, 127], the connection between these different approaches to measure dynamic correlation lengthscales in systems with glassy dynamics will not be addressed in this Chapter, but is a worthy topic for future research.

Since at present the non-monotonic $T-$dependence of the dynamical length scale probed by an amorphous wall has been observed only in one model glass-former, it is important to investigate whether this phenomenon is general or not. In order to address this question we have performed a similar analysis in the widely studied KA system (the same model used in Ref. [121]). When taken together, the results of previous studies in Refs. [126, 128, 129] may be interpreted as suggesting that a crossover in the relaxation dynamics across the mode-coupling temperature exists but is weaker for the KA than the HARM system. Therefore we anticipate that if the non-monotonic evolution of dynamic profiles near an amorphous wall results from this crossover, then this effect should be less pronounced in the KA model. In

the present work, we seek to assess this possibility and to better understand which features of supercooled liquids near an amorphous wall are generic. Given our findings in the KA system, we then extend our study to two other supercooled liquids. Furthermore we demonstrate that indications of an additional crossover at a temperature higher than T_c may be uncovered by the investigation of dynamics close to an amorphous wall, therefore showing that there are in fact *two* crossover temperatures at which the dynamics is changing.

This Chapter is organized as follows. In Sec. 4.2 we discuss the models to be studied, as well as the details of the various calculations we will employ. In Sec. 4.3 we present the results of our analyses and comparison with the previous results of Ref. [113]. In Sec. 4.4 we present results comparing the dynamics in directions perpendicular and parallel to the wall, which reveal further information related to the dynamics of supercooled liquids. Finally, in Sec. 4.5 we conclude and discuss the impact of our results in the broader context of recent work on supercooled liquids.

4.2 Models and methods

In this Chapter, we present data for three model systems. Our primary system of interest is the Kob-Andersen Lennard-Jones model (KA), an 80:20 binary mixture of particles at density $\rho = 1.2$ with very well characterized structural and dynamical properties [3, 130]. All quantities are reported in standard reduced units. In this model, we find the onset of slow dynamics occurs near $T_o \approx 1.0$, and the mode-coupling crossover has been previously reported as $T_c \approx 0.435$ [131]. We have fully equilibrated this model for the system size $N = 1900$ particles in a cubic box for the temperatures $T = 0.9$, 0.8, 0.7, 0.65, 0.625, 0.6, 0.575, 0.56, 0.55, 0.5, 0.48, 0.45, 0.435, and 0.432. Simulations were done with NVT dynamics for $100\tau_\alpha^{\rm bulk}$ at each temperature using the LAMMPS package [105]; $\tau_\alpha^{\rm bulk}$ was determined by calculating the self-intermediate scattering function, $F_s(k,t) = \frac{1}{N}\sum_{j=1}^{N} e^{i\mathbf{k}\cdot(\mathbf{x}_j(t)-\mathbf{x}_j(0))}$, and defining $F_s(k = 7.25, t \equiv \tau_\alpha^{\rm bulk}) = 1/e$. Each equilibrated configuration was replicated three times along the $z-$axis to make a rectangular box of dimensions approximately $11.655 \times$

11.655×34.966. The rectangular boxes were again simulated for $100\tau_\alpha^{\rm bulk}$ to remove the periodicity introduced by replicating the system. Each configuration was then tested for equilibration by calculating $F_s(k,t)$ for the first and second half of yet another $100\tau_\alpha^{\rm bulk}$ length trajectory. Only configurations whose dynamics showed no signs of aging (i.e. identical scattering functions for both halves of the trajectory) were used for subsequent steps.

To study these configurations with an amorphous wall, simulations were run where the positions of particles within a slab of width $W = 3$ were held fixed. Since we simulate the KA system with a standard cutoff of the potential at $r_{\rm cut} = 2.5$, this slab is effectively of infinite thickness as no particle on one side can interact directly or indirectly with those on the other side. This allows to determine the $z-$dependence of the static and dynamic properties of the system for distances up to $z_{max} = (34.966 - 3)/2 \approx 15.98$. At each temperature, we ran molecular dynamics simulations of length 500-$1000\tau_\alpha^{\rm bulk}$ for $30 - 45$ independent wall realizations to ensure both thermalization of a single realization, and a proper disorder average over the quenched disorder imposed by the frozen wall.

In addition to the KA system, we performed a similar set of studies for two other models. The first is the Weeks-Chandler-Andersen (WCA) version of the KA system [39], for which we performed simulations down to $T = 0.325$ (the mode-coupling temperature is $T_c \approx 0.28$ [131], and $T_o \approx 0.7$). For this model, identical box sizes were used as for the KA. The third model we study is the harmonic sphere system (HARM) of Ref. [113], which had been previously discussed [40, 132] ($T_c \approx 5.2$ [113], $T_o \approx 12$). As in Ref. [113], we use $N = 4320$, however here we prepare the system analogously to the KA system, first equilibrating a sample containing 1440 particles, then replicating it to construct a box with dimensions approximately $12.873 \times 12.873 \times 38.620$. In this case, we used a wave vector $k = 6.28$ to define the relaxation time of the system and other subsequent quantities, and a wall thickness of $W = 2$, due to the very short ranged potential in this model. For the HARM and WCA models we ran simulations with $20 - 30$ independent wall realizations. For the WCA system we found, by looking at aging behavior in $F_s(k,t)$, that some trajectories crystallized after times on the order of several hundred bulk τ_α at $T = 0.35$ in the presence of the wall. The

tendency to crystallize was more pronounced at $T = 0.325$. Crystallization was evident from visual inspection as well as from a drop in the potential energy of samples which crystallized. These trajectories were excluded from our data, and hence our statistical confidence at these temperatures is reduced and a detailed analysis of temperatures close to the mode-coupling crossover was not possible.

For each model and for each trajectory, we have calculated the overlap, $q_c(z,t)$, and self-overlap, $q_s(z,t)$, as a function of time and distance (z) from the face of the wall. These quantities, which contain similar information as the coherent and incoherent intermediate scattering functions, are calculated by tiling the system outside of the wall into small boxes of side-length l small enough such that they have occupation numbers (defined by the number of particle centers in a cell) $n_j \in \{0, 1\}$. In a previous work it was determined that $l \approx 0.37$ was a good size to enforce this condition in the KA and WCA systems without making l so small as to result in poor statistics [117]. In the present study we choose $l = 0.37597$ which tiles each short dimension of the samples into $\tilde{N} = 31$ boxes, but we have checked that changing this parameter does not have any effect on the resulting physics. Similarly, we choose $l \approx 0.45$ for the HARM, and tested that this gives the same results as $l \approx 0.55$, the value used in Ref. [113] (at that size, $n_j > 1$ occasionally). We define, at each distance z from the wall,

$$q_c(z,t) = \left\langle \frac{1}{\tilde{N}^2} \sum_{j=1}^{\tilde{N}^2} \frac{n_j(t'+t)n_j(t')}{\rho l^3} \right\rangle, \tag{4.1}$$

and

$$q_s(z,t) = \left\langle \frac{1}{\tilde{N}^2} \sum_{j=1}^{\tilde{N}^2} \frac{p_j(t)}{\rho l^3} \right\rangle, \tag{4.2}$$

where $p_j(t)$ is a function which is 1 if box j is occupied by a particle at a reference time t' and later by the same particle at $t' + t$. In a bulk system with no wall, $n_j(t)$ and $n_j(0)$ fully decorrelate as $t \to \infty$, so the correlation function $q_c(z,t)$ tends to the random value $q_r \equiv \rho l^3$. Hence we define $\tilde{q}_c(z,t) \equiv q_c(z,t) - q_r$ so that this function decays to zero in the bulk case. With the presence of the wall, this function will decay to a finite value termed $\tilde{q}_c(z,\infty) \geq 0$, which quantifies the strength of the static correlations imposed by the presence of the wall.

We define the relaxation time of the self-overlap $\tau_s(z)$ by $q_s(z, \tau_s(z)) = 0.2$.[2]

We have also investigated a second measure of density relaxation, the self-intermediate scattering of particles found at distance z from the wall,

$$F_s(\mathbf{k}, z, t) = \left\langle \frac{1}{N(z)} \sum_{j=1}^{N(z)} e^{i\mathbf{k}\cdot(\mathbf{x}_j(t)-\mathbf{x}_j(0))} \right\rangle, \tag{4.3}$$

where this sum extends over the particles which start in a slab of width 1.0 at distance z from the wall, but need not necessarily end in that slab. We then define scattering functions for relaxation parallel and perpendicular to the wall by using wave vectors which are aligned with the unit vectors $\hat{\mathbf{x}}$ and $\hat{\mathbf{z}}$ respectively. Thus, we define $F_s^{||}(z,t) \equiv F_s(\mathbf{k} = 7.25\hat{\mathbf{x}}, z, t)$ and $F_s^{\perp}(z,t) \equiv F_s(\mathbf{k} = 7.25\hat{\mathbf{z}}, z, t)$, and define $\tau^{||}$ and $\tau^{\perp}$ when the associated correlation functions decay to a value of $1/e$.

4.3 Overlap relaxation times

4.3.1 Saturating dynamic length scale

The first question we wish to address is whether the non-monotonic growth of the dynamical length scale seen in Ref. [113] is also found in models other than the HARM system. For this purpose we measure dynamical relaxation profiles by calculating $\tau_s(z)$ and $\tau_c(z)$ at a series of temperatures in the KA system. As discussed in Ref. [113], dynamical properties calculated from the self and collective overlaps give very similar physical results. However, as $q_c(z,t)$ decays to a plateau while $q_s(z,t)$ always decays to zero, it is easier to measure $\tau_s(z)$ with confidence as there is no need to include the long time limit of this correlation

[2] Ref. [113] defined the relaxation time of the self-overlap τ_s by fitting the final decay of $q_s(z,t)$ to a stretched exponential of the form $A\exp[(-t/\tau_s)^{\eta}]$ with $\eta < 1$. We found the definition in the main text to give relaxation times proportional to these, but due to the increased computational expense of simulating the KA system, we chose this definition, which allows us to extract relaxation times at distances near the wall at the lowest temperatures with shorter simulations than would otherwise be necessary.

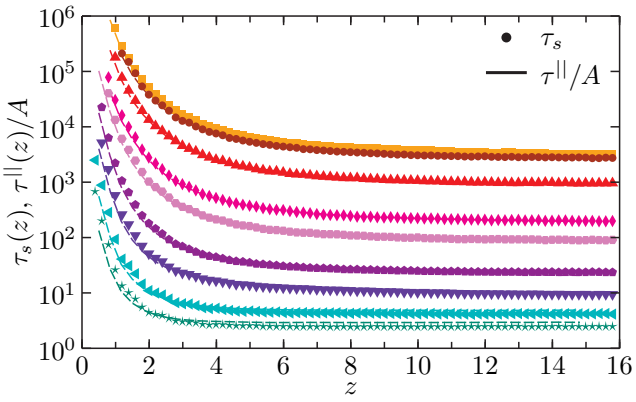

Figure 4.1: Relaxation times in the KA system from self-overlap (τ_s, points) and parallel self-intermediate scattering function ($\tau^{||}$, lines) versus the distance z from the wall, shown for all studied temperatures. Error bars as determined from a bootstrap analysis [65] are much smaller than the points shown. The second set of relaxation times is rescaled on the first one using a temperature independent rescaling constant $A = 0.7$ obtained from $A = \tau^{||}(z = 15, T = 0.435)/\tau_s(z = 15, T = 0.435)$. From top to bottom: $T = 0.432$, 0.435, 0.45, 0.48, 0.5, 0.55, 0.6, 0.7, and 0.8.

function as an additional fitting parameter. We therefore concentrate on properties derived from the self-overlap $q_s(z, t)$.

Before discussing these properties we note that, just as in the HARM system, the static overlap $\tilde{q}_c(z, \infty)$ decays exponentially with the distance z at all temperatures in the KA system, and that the static length extracted by fitting this decay grows by only a small fraction of its value at high temperatures over the considered temperature range. These properties are discussed in Sec. 4.7.1.

The relaxation times $\tau_s(z)$ for different temperatures are shown in Fig. 4.1. As expected from previous studies, the dynamics slow dramatically near the wall, and relaxation times at a given distance increase with decreasing temperature [113, 121]. At large z each curve tends to plateau before z reaches a value corresponding to half of the box length. For comparison, we show that the relaxation times $\tau^{||}$ scale directly on top of the data from the self-overlap. demonstrating that the relaxation of the self-overlap is mostly dominated by relaxation in the parallel direction to the wall. This is reasonable since the dynamics in the direction

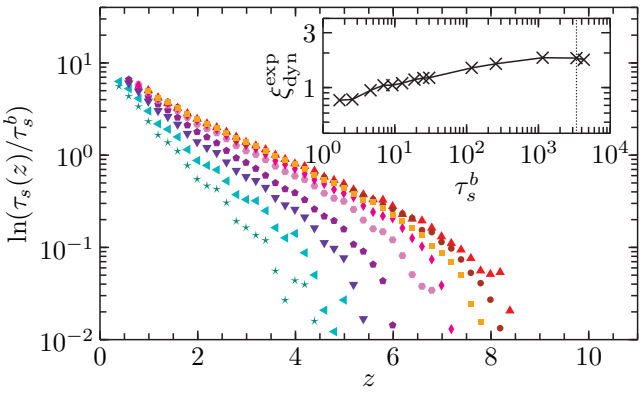

Figure 4.2: Self-overlap relaxation times in the KA system at a distance z from the wall are divided by the bulk relaxation for the given temperature. The temperatures and symbols shown are the same as in Fig. 4.1. By fitting these curves to Eq. (4.4), a dynamical length scale $\xi_{\rm dyn}^{\rm exp}$ is extracted, as shown in the inset for all temperatures listed in Sec. 4.2. This length scale grows with decreasing temperature but saturates at a temperature above T_c, where $\tau_s^b \approx 3 \times 10^3$, indicated by a vertical dotted line.

perpendicular to the wall is significantly slower (see Sec. 4.4 below), so that the self-overlap has already decayed by the time perpendicular motion sets in.

Based on earlier results for the KA model and results in the HARM system, we make the ansatz that the logarithm of the relaxation times in the presence of the wall decays exponentially to a plateau [113, 121],

$$\ln(\tau_s(z)) = B \exp\left(-z/\xi_{\rm dyn}^{\rm exp}\right) + \ln(\tau_s^b), \tag{4.4}$$

where τ_s^b is the bulk relaxation time, i.e. the relaxation time computed in the same manner but without the presence of the wall.

To extract the temperature dependence of the lengths in Fig. 4.1 we follow the recipe of Ref. [113]. At each temperature we divide the data by $\tau_s^b(T)$ (these data can be found in Sec. 4.7.2). We then fit the decay of $\ln(\tau_s(z)/\tau_s^b)$ to Eq. (4.4) and extract the length scale $\xi_{\rm dyn}^{\rm exp}$ and the prefactor B. The results of this procedure can be seen in Fig. 4.2.

The inset of Fig. 4.2 shows the growth of the obtained dynamical length scale $\xi_{\rm dyn}^{\rm exp}$ and we recognize that $\xi_{\rm dyn}^{\rm exp}$ saturates for $T > T_c$. That this saturation is not just an artifact

of the fitting procedure can be easily recognized from the data shown in the main panel of Fig. 4.2 which, for low temperatures, collapses almost perfectly onto a single master curve which implies that $\xi_{\rm dyn}^{\rm exp}$ depends only weakly on T. From this saturation we can conclude that our observed $T-$dependence of $\xi_{\rm dyn}^{\rm exp}$ is compatible with the results obtained for the HARM system [113], even if for the KA system there is no strong evidence for a non-monotonic behavior in $\xi_{\rm dyn}^{\rm exp}$ (although the length does appear to decrease very slightly). The absence of such a non-monotonic $T-$dependence in the KA system does not preclude the possibility of a change in behavior of $\xi_{\rm dyn}^{\rm exp}$ at lower temperatures. Indeed, it is expected that at temperatures below T_c, $\xi_{\rm dyn}^{\rm exp}$ will increase again at a temperature that is system dependent, and this behavior could supersede the non-monotonicity observed in the length scale of the HARM system [123].

That the $T-$dependence of $\xi_{\rm dyn}^{\rm exp}$ is less pronounced for the KA model than the HARM is also consistent with the results from Ref. [128] in which the relaxation dynamics of both KA and HARM has been studied using periodic boundary conditions. In that work it was shown that finite size effects can lead to a non-monotonic $T-$dependence of the relaxation times for the HARM system, but that in the KA system these effects are much less pronounced, a result that was argued to be related to how sharp the cross-over between mode-coupling like dynamics to activated dynamics is (less sharp for the KA system than for the HARM model), which is reflected directly in the $T-$dependence of the dynamical length scale (less pronounced for the KA than for the HARM). This difference between the two systems is also in agreement with the results from Ref. [129] where it was shown that for the HARM system the height of the peak in the dynamical four-point correlation function χ_4^{NVE} has a non-monotonic behavior in T whereas the one for the KA system shows only a saturation [126]. Finally we mention that the existence of a non-monotonic behavior in $\xi_{\rm dyn}^{\rm exp}$, or its saturation, can be naturally interpreted in the context of RFOT in terms of an underlying change of physical mechanism responsible for structural relaxation occurring at T_c [113, 123–125].

4.3.2 Further analysis of dynamic profiles

While the decay of $\ln(\tau_s(z))$ near the wall does indeed appear to match the exponential ansatz well, we observe that the relaxation times τ_s^b are larger than the relaxation time at $z = 15.98$ (see Sec. 4.7.2). This suggests that the analysis of the dynamic profiles is in fact not totally straightforward.

As an alternative approach for analyzing the data, we divide the profiles $\tau_s(z)$ by τ_s^h, the value of the relaxation time measured at large z. We show the result in Fig. 4.3(a). There are several features worthy of discussion when viewed from this perspective. First, except for the highest temperatures, the curves are at z_{max} still decaying which shows that the accuracy of our data allows us to see finite size effects in the dynamics even in the center of the box. Second, while the highest temperatures display exponential decay of $\ln(\tau_s)$, the curves at the lowest temperatures are somewhat bent in this log-lin representation and it is not clear how to best analyze quantitatively this curvature. As a first attempt, we have tried to describe these data using an exponential decay at short z, followed by a second exponential decay at longer z. At intermediate supercooling, particularly at $T = 0.6$, deviations from a single exponential decay are indeed quite pronounced. Third, the low T curves nearly collapse (except perhaps at very large z values). This is illustrated in the inset of Fig. 4.3(a) where the curves from the lowest five temperatures are isolated, clearly showing that these profiles are virtually identical over a large range of distances, despite the fact that relaxation times change by nearly two decades over that same temperature regime (see Fig. 4.1).

Since in this representation the data shows a clear curvature, we have chosen to split it into two parts, one for $z \leq z^*$ and one for $z > z^*$. From these fits we have extracted two dynamical length scales, $\xi_{\rm dyn}^{\rm short}$ and $\xi_{\rm dyn}^{\rm long}$, respectively. For $T > 0.6$ best fits were obtained with $z^* = 5$ and for $T \leq 0.6$ best fits resulted when using $z^* = 6$. These lengths are shown in Fig. 4.3(b), along with the previous $\xi_{\rm dyn}^{\rm exp}$, for reference. We have also fit these data with a sum of exponentials, which provides a fit that matches the raw data quite well. Unfortunately the large number of fit parameters leads to overfitting that results in nonphysical length scales.

It is important to emphasize that even with this refined method of analysis, our previous

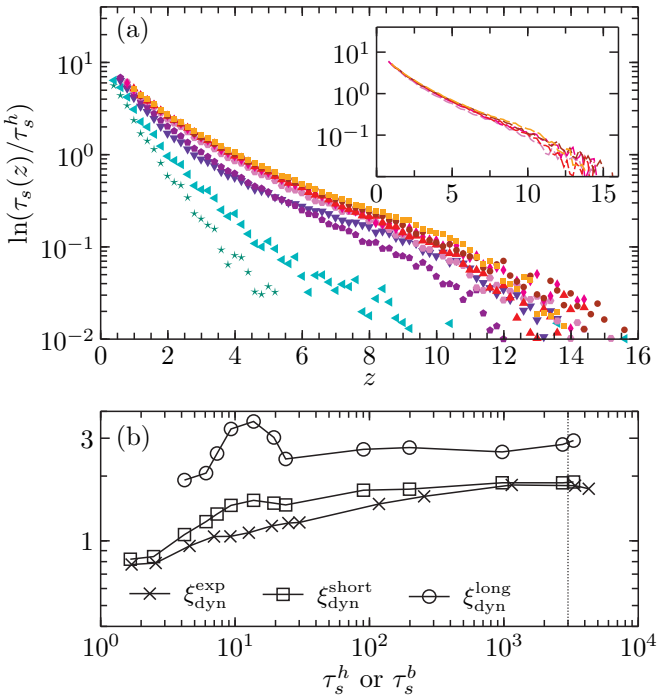

Figure 4.3: (a) Self-overlap relaxation times in the KA system divided by value τ_s^h, the value of $\tau_s(z)$ averaged over the large z range [15.4 : 15.8]. The temperatures shown her are the same as in Fig. 4.1. The relaxation is exponential at high T, becomes very curved at intermediate temperature $T \approx 0.6$, and then evolves very little at low T. For all temperatures, there is an exponential decay at short distances, yielding a length $\xi_{\rm dyn}^{\rm short}$. There is also an approximately exponential decay at long distances from which we extract $\xi_{\rm dyn}^{\rm long}$. The inset isolates temperatures $0.432 \leq T \leq 0.5$ to emphasize the low-T saturation. (b) Relaxation time dependence of the three dynamic lengths extracted from fitting the profiles plotted against τ_s^b for $\xi_{\rm dyn}^{\rm exp}$ and τ_s^h for $\xi_{\rm dyn}^{\rm long}$ and $\xi_{\rm dyn}^{\rm short}$. The approximate position of T_c is indicated by a vertical dotted line. Lengths are shown for all temperatures listed in Sec. 4.2.

results concerning the saturation of $\xi_{\rm dyn}^{\rm exp}$ remain robust. Clearly, even without any fitting, there is still a saturation of the dynamic profiles at temperatures close to T_c, as can be seen from the collapse of the data with the new normalization at low T (see inset of Fig. 4.3(a)). This shows that the observation that $\xi_{\rm dyn}^{\rm exp}$ saturates as a function of T does not depend on the detail how the length scale has been determined.

This more precise type of analysis permits to detect an unexpected feature in the T–dependence of the dynamic length scales. From Fig. 4.3(b) we see that the absolute value and the $T-$dependence of $\xi_{\rm dyn}^{\rm short}$ are very similar to the ones of $\xi_{\rm dyn}^{\rm exp}$ in that also this length scale grows with decreasing T and then saturates around T_c. The $T-$dependence of $\xi_{\rm dyn}^{\rm long}$ is somewhat weaker than the one of $\xi_{\rm dyn}^{\rm short}$ in that it increases only by a factor of around 1.5 instead of the factor of two found for the latter. Much more important is, however, the observation that at intermediate temperatures, $T \approx 0.6$, $\xi_{\rm dyn}^{\rm long}$ shows a very pronounced peak. We stress that this peak is in no way a result of the fit and the behavior is clearly evident from inspection of the data in Fig. 4.3(a).

We note that this temperature is significantly above the mode-coupling temperature of the system, $T_c \sim 0.435$, but it coincides with the crossover temperature recently termed "T_s" in Ref. [133]. The authors of Ref. [133] identify this T_s both with the breakdown of the Stokes-Einstein relation as well as a change in the "shape" of dynamical heterogeneities. While a quantitative connection between $\xi_{\rm dyn}^{\rm long}$ and the Stokes-Einstein decoupling is *a priori* not obvious, we will in the following provide evidence that both types of behavior are indeed correlated.

We emphasize that the non-monotonic evolution of the length $\xi_{\rm dyn}^{\rm long}$ is a qualitatively different phenomenon from the evolution of a dynamic length discussed in Ref. [113]. Indeed, because of the single exponential fitting protocol used in that paper, the analog crossover at temperature T_s was previously not detected in the HARM system. In fact, while $\ln(\tau_s)$ seems more exponential in the HARM system than in the KA system, we indeed see a signature of this higher temperature crossover around $T \approx 9$, near the putative T_s for this model, a temperature not examined in Ref. [113] (see Sec. 4.7.3). In particular, it should be noted

that fits to obtain $\xi_{\rm dyn}^{\rm exp}$ as shown in Fig. 4.2 and in Ref. [113] give relatively little weight to the relaxation times at large z, thus making the peak seen in $\xi_{\rm dyn}^{\rm long}$ is hardly noticeable in $\xi_{\rm dyn}^{\rm exp}$ (see Fig. 4.3). Note that the discovery of this novel crossover phenomenon does not affect any of the conclusions about the dynamical length scale having a maximum at T_c in this system because we find, as in the KA system, that $\xi_{\rm dyn}^{\rm exp} \approx \xi_{\rm dyn}^{\rm short}$, and both these length scales have indeed a maximum in the vicinity of the mode-coupling crossover temperature T_c.

To give further evidence for a relationship between the crossover temperature T_s and the evolution of the length $\xi_{\rm dyn}^{\rm long}$, we have repeated our full analysis of dynamic profiles for a third model, namely the WCA system, which again shows this anomalous behavior around $T_s \approx 0.425$, as shown in Sec. 4.7.3.

4.4 Comparison of transverse and longitudinal relaxation

In this section, we investigate the connection between dynamic profiles and the crossover temperature T_s further. Because T_s was previously related to a change in the geometry of dynamic heterogeneities [133], a possible connection could come from a geometric analysis of dynamic profiles near amorphous walls. To this end, we separately analyze the relaxation into perpendicular and parallel components with respect to the wall.

We analyze the self-intermediate scattering function at different distances from the wall, as defined in Eq. (4.3). It is simple to resolve the relaxation times for dynamics parallel and perpendicular to the wall, as done for instance in Ref. [134]. The relaxation times obtained for wavevectors parallel to the wall are shown in Fig. 4.1. Here, $\tau^{||}(z)$ has been divided by a constant value corresponding to the ratio $\tau^{||}(z)/\tau_s(z)$ at a single distance ($z \approx 15$) and a single temperature ($T = 0.435$). The curves and points respectively representing $\tau^{||}(z)$ and $\tau_s(z)$ lie perfectly on top of each other except for a small deviation at the highest temperatures, suggesting that $\tau^{||}(z)$ reports on the same physics as $\tau_s(z)$ at supercooled

temperatures, and does not contain additional physical information about relaxation near the amorphous wall.

In agreement with previous results [134], the relaxation times obtained for wavevectors perpendicular to the wall are always slower than for those parallel to the wall. In Fig. 4.4(a-c) we show how the perpendicular relaxation times compare to the parallel relaxation times at different distances from the wall via the investigation of the ratio $\tau^{||}(z)/\tau^{\perp}(z)$ in the three different models studied in this Chapter, the HARM, KA and WCA systems.

In each system three temperature regimes can be identified. The qualitative features of these regimes are illustrated by Fig. 4.4(d), where we select a subset of equivalent temperatures for each system, as being representative of the various regimes, which can be described as follows.

- Above T_o, the wall suppresses perpendicular more than parallel relaxation at small z, but then the ratio tends rapidly towards unity at large distances.

- Near T_o, the ratio tends to a pseudo-plateau at values less than one for all z values accessible. A dip in the ratio of $\tau^{||}(z)/\tau^{\perp}(z)$ is also observed to develop near $z \approx 1$. This results in a maximum of the ratio at an intermediate distance $z_{\text{peak}} \approx 4.0$ as T is lowered.

- At temperatures below T_o, the curves become more complex in that at large z the values of the ratio decreases whereas at z_{peak} the ratio is at intermediate T basically constant before it increases slightly. Furthermore we see that the dip at $z \approx 1$ also rises slightly with decreasing temperature.

We define z_{peak} as the distance from the wall where the ratio $\tau^{||}/\tau^{\perp}$ peaks and consider the temperature evolution of this peak value, as shown in Fig. 4.4(e). In all three systems, the temperature where the peak value is minimized falls very close to values of T_s given in Ref. [133].

This coincidence is robust against finite size effects that are known to affect the dynamics in simulation boxes with an elongated shape [135]. Tests using larger box sizes demonstrate

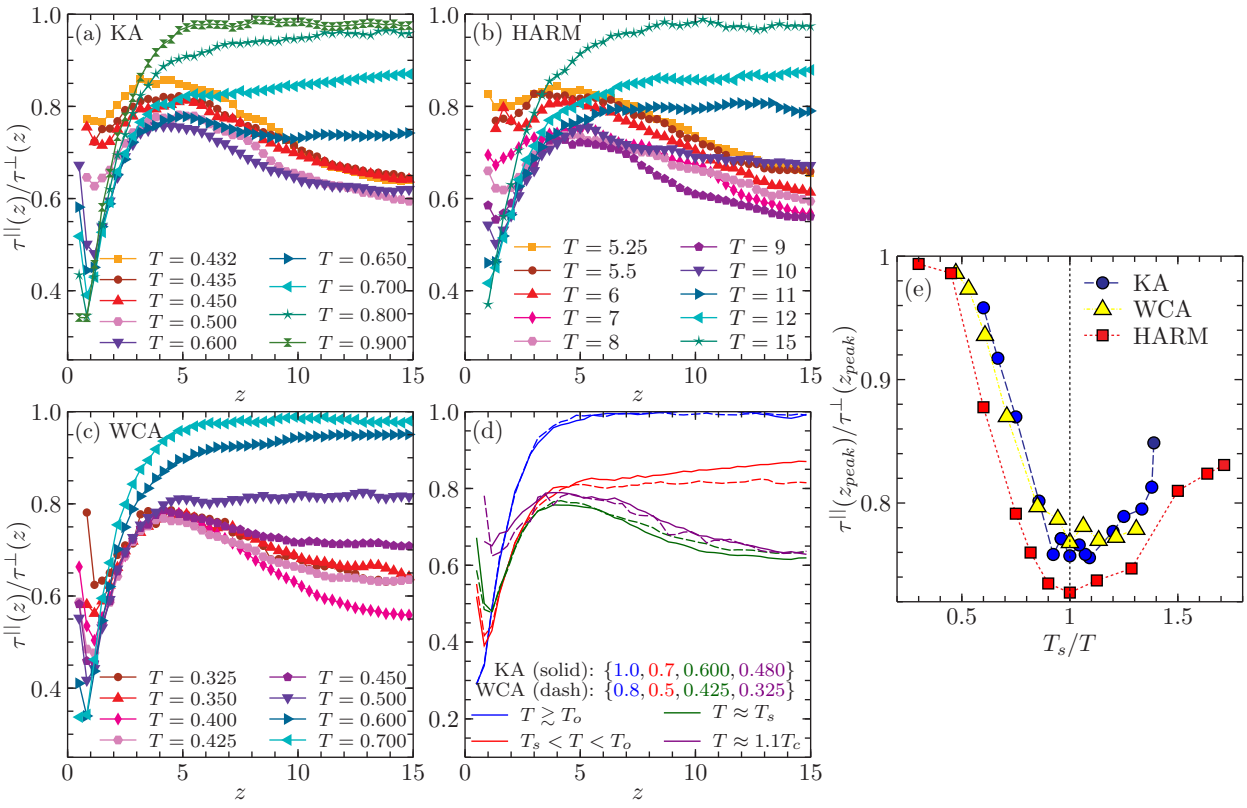

Figure 4.4: (a-c) Distance dependence of the ratio of the parallel to perpendicular relaxation times in the three models studied. Due to the presence of the wall, $\tau^{||}(z) \leq \tau^{\perp}(z)$ at all distances. At high temperatures, the curves tends to unity but for lower temperatures the curves approach a fractional value for the z-range accessible. (d) Profiles of the curves in the distinct regimes identified, emphasizing in particular the emergence of a maximum in the ratio at a distance $z_{\rm peak}$. Results for KA are shown with solid lines and for WCA with dashed lines. At $z = 15$, from top to bottom the curves are ordered $T \gtrsim T_o$, $T_s < T < T_o$, $T \approx 1.1T_c$, and $T \approx T_s$. (e) The ratio of relaxation times at $z_{\rm peak}$ as a function of T_s/T, showing that the peak value is minimized when $T \approx T_s$, the crossover temperature analyzed in Ref. [133]. The values used for T_s are 0.6, 9.0, and 0.425 for the KA, HARM and WCA systems, respectively.

that the precise value of the ratio at large z depends weakly on the box size, but the data up to z_{peak} and just beyond are fairly insensitive to such changes, as demonstrated in Sec. 4.7.4. Hence the behavior and temperature correspondence appear to be fairly insensitive to finite size effects.

The precise dependence of the ratio $\tau^{||}(z)/\tau^{\perp}(z)$ is complicated, and further microscopic investigations of its behavior would be needed to understand these data in more detail. However, it is interesting to speculate on the connection between the behavior observed in Fig. 4.4(e) and that reported in Ref. [133]. The authors of Ref. [133] note that the ratio of dynamical heterogeneity length scales associated with parallel and perpendicular displacements markedly changes behavior at T_s, which they claim to be the temperature at which violation of the Stokes-Einstein relation first occurs. The fact that we observe in the vicinity of T_s a significant change in the $T-$dependence of $\tau^{||}(z)/\tau^{\perp}(z)$ is harmonious with the notion that this temperature is associated with a change in directionally resolved relaxation motifs, and gives further impetus for microscopic study of particle motion near the frozen wall as T varies above and below T_s.

It should also be noted that we observe clear features of altered relaxation in both $\xi_{\text{dyn}}^{\text{long}}$ as well as $\tau^{||}(z)/\tau^{\perp}(z)$ at T_s, independent of metrics based on Stokes-Einstein violation, whose onset is not necessarily sharp enough to clearly define a characteristic temperature. In this sense, one can bypass definitions based on transport anomalies and relate T_s directly to the change of two-point relaxation behavior provided by the proximity of a frozen interface.

In summary we can conclude that the results of this section and Sec. 4.3 above give further evidence in support of the notion, first advanced in Ref. [133], of a well-defined characteristic temperature T_s below the onset temperature of slow dynamics but above T_c, which physically relates to a marked crossover in the geometric properties of dynamic heterogeneity.

4.5 Discussion and conclusions

In this Chapter we have extended previous studies related to the relaxation of supercooled liquids near a wall created from a subset of particles fixed in their equilibrium positions. We find clear evidence that as T_c is approached, the dynamical length scale defined in Refs. [113] and [121] quantitatively saturates in the KA system. This behavior is to be contrasted with the non-monotonic growth of the same length scale in the HARM system. This distinction, namely a saturation as opposed to a decrease in the length scale below T_c, is in harmony with both the behavior of χ_4^{NVE} [126, 129] as well as trends in the behavior of finite size effects as filtered through relaxation times in these two models [128]. Taken together, these results all suggest that the crossover between transport mechanisms at T_c is qualitatively similar in both systems, but is quantitatively sharper in the HARM, which may therefore be viewed to be closer to the idealized mean-field limit than the KA system.

We have also investigated the behavior of relaxation channels parallel and perpendicular to the wall. While motion parallel to the amorphous wall mirrors the behavior revealed by studies of the self-overlap function, we found that the behavior of the ratio $\tau^{||}(z)/\tau^{\perp}(z)$ shows clear evidence of a change in behavior at a recently identified temperature T_s, across three different model systems. In Ref. [133] it has been argued that T_s marks a temperature where the shape of the dynamical heterogeneities changes, in the sense that transverse and longitudinal relative motions of particles become decoupled. Thus it is physically reasonable that close to the wall such a decoupling also affects the relaxation behavior in the parallel direction in a different manner than in the orthogonal one, thus rationalizing our findings regarding the $T-$ and $z-$dependence of $\tau^{||}(z)/\tau^{\perp}(z)$.

While our results place the change of transport mechanisms invoked to account for the dynamics of the HARM model [113, 123] near an amorphous wall on firmer grounds, we emphasize that the strong saturation of the dynamic lengthscale $\xi_{\rm dyn}^{\rm exp}$ revealed in both HARM and KA models has no clear counterpart in available measurements of dynamic lengthscales from bulk four-point functions [136, 137], which appear to display no obvious saturation in the mode-coupling regime. Although this might indicate that both types of measurements are

unrelated, we also note that the crossover temperature T_s detected through analysis of four-point functions in Ref. [133] is also observed here using measurements near an amorphous wall via two-point quantities, albeit those extracted near an object that breaks spatial symmetry. While this approach is in the same spirit of earlier studies based on measurements of the response of two-point correlators to external fields [126, 138], the present set-up using pinned particles provides a potentially simple means to observe the changes that occur at T_s in an experimental setting. Future work should be devoted to real-space dynamical analysis of the behavior of motion parallel and perpendicular to the wall in order to gain deeper insight into the observations presented in this Chapter. Overall, these results reveal that a better understanding of the connection between the various dynamic lengthscales studied in supercooled liquids is needed.

4.6 Acknowledgments

I thank D. Coslovich, E. Flenner, and G. Szamel for useful discussions. Some of this research was performed on resources provided by the Extreme Science and Engineering Discovery Environment (XSEDE), which is supported by National Science Foundation (NSF) grant number OCI-1053575. Some computations were performed on the Midway resource at the University of Chicago Research Computing Center (RCC). Simulations performed were organized by executing LAMMPS runs with the Swift parallel scripting language (NSF Grant No. OCI-1148443) [64].

4.7 Appendix

4.7.1 Static Overlaps

Although the focus of this Chapter is on the dynamical properties of the KA system near an amorphous wall, it is also useful to investigate the growth of static order. In Fig. 4.5 we show the static overlaps for comparison with Ref. [113]. As in that work, we see that the static

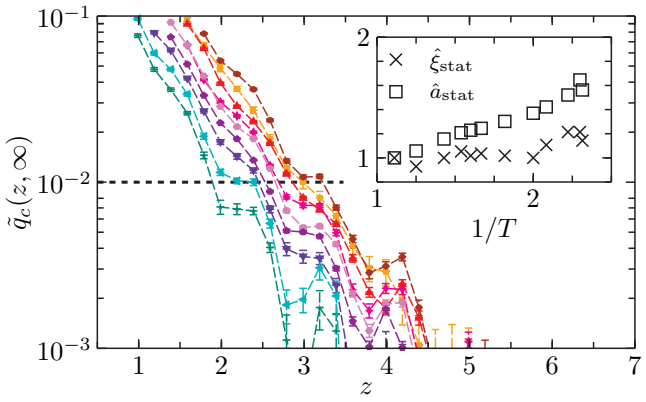

Figure 4.5: Static overlap values extracted from $q_c(z, t \to \infty)$ for the temperatures in Fig. 4.1. The decay is exponential and becomes steadily longer ranged as temperature is lowered. Two static length scales, $\xi_{\rm stat}$, the inverse of the slope of the decay, and $a_{\rm stat}$, the z value where $\tilde{q}_c(z,\infty)$ lines cross the value $C = 0.01$, as illustrated by a horizontal dashed line may be extracted. 1σ error bars from a bootstrap analysis are shown [65]. Inset: The lengths $\hat{a}_{\rm stat} = a_{\rm stat}/a^0_{\rm stat}$ and $\hat{\xi}_{\rm stat} = \xi_{\rm stat}/\xi^0_{\rm stat}$ where $a^0_{\rm stat}$=1.92 and $\xi^0_{\rm stat}$=0.56 are the values of the lengths at high temperature, $T = 0.9$.

overlap decays exponentially with distance from the wall, and we remark that these static quantities decay much more quickly than the dynamical profiles shown in Figs. 4.3. We see a slight "layering" effect which we suspect is more pronounced here than in Ref. [113] because in the present work we used a completely amorphous wall, while in Ref. [113] a reflective wall and an amorphous potential were used in combination.

To extract static length scales, we choose to fit these curves to the function

$$\tilde{q}_c(z,\infty) = C\exp(-(z - a_{\rm stat})/\xi_{\rm stat}), \tag{4.5}$$

with a fixed value of $C = 0.01$, shown by a horizontal dashed line in Fig. 4.5. This fit gives values for $\xi_{\rm stat}$ describing the exponential decay of the static profiles, which are small and grow very slowly. In addition, we can consider the evolution of $a_{\rm stat}$ quantifying the distance z for which the overlap equals $C = 0.01$. This is another static length scale, which is slightly larger than $\xi_{\rm stat}$ and also grows quite slowly.

Both are shown in the inset of Fig. 4.5 and are seen to grow by a much smaller amount

than the dynamical length scales measured. Although there are small qualitative differences between the KA and HARM systems with respects to the magnitudes of static and dynamic length scales, both show a pronounced decoupling between static and dynamic properties, in line with other studies showing static length scales which are smaller and grow more slowly than dynamical ones [49, 116–118].

4.7.2 Relaxation times in the KA system

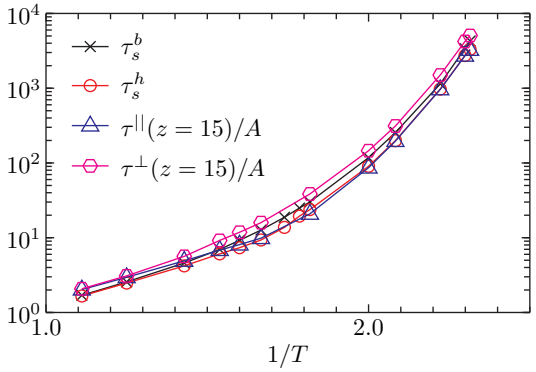

Figure 4.6: Temperature dependence of the various relaxation times discussed in the main text for the KA system. The values of $\tau^{||}$ and $\tau^{\perp}$ have been scaled by the value $A = 0.7$ as discussed in Fig. 4.1.

Fig. 4.6 compares the four relaxation times used in the main text for the KA system. As discussed previously, the values of $\tau^{||}(z)$ and $\tau_s(z)$ can be scaled on top of each other using a temperature independent constant, although there is some deviation at high temperatures. The need for rescaling simply arises because of the choice of the window size $l = 0.45$ for the self-overlap calculation and the value $k = 7.25$ for the self-intermediate scattering function. In Fig. 4.6, we have also rescaled the values of $\tau^{\perp}$ showing that relaxation in the perpendicular direction in the middle of the box is slower than in the parallel direction at all temperatures. Finally, we also show the value of the self-overlap relaxation time without the wall, which is larger than the self-overlap relaxation time at all temperatures at the center of the box in the presence of the wall. This origin of this result will be discussed in a

forthcoming work [135].

4.7.3 Overlap curves in the HARM and WCA systems

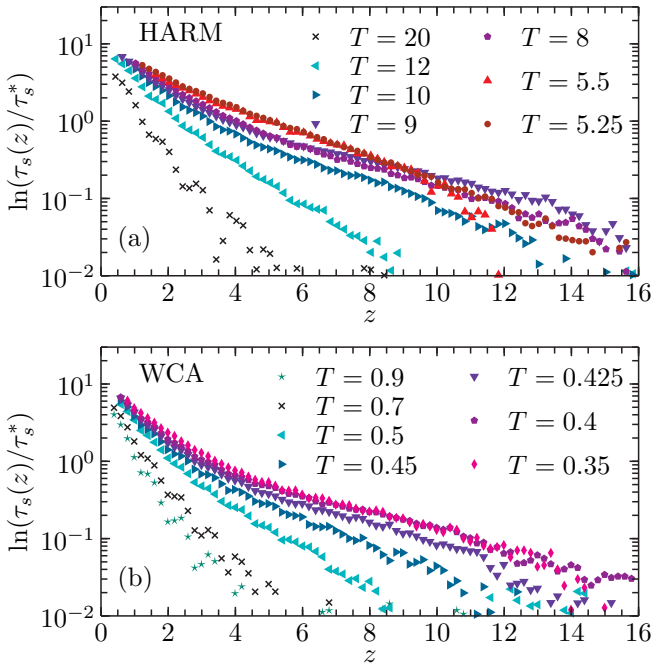

Figure 4.7: Distance dependence of the self-overlap relaxation times for the HARM system (a) and the WCA system (b) in a representation similar to the one of Fig. 4.3 for the KA model.

For the sake of comparison with the results presented in Fig. 4.3, we also include the results for the HARM and WCA systems. In Fig. 4.7(a) the results for the HARM system are plotted. While the curves decay in a completely exponential manner at the highest and lowest temperatures, there is a pronounced curvature or double-exponential character near $T = 9$, a temperature not studied in Ref. [113]. The curvature at $T = 8$ is consistent with the data in that work.

Figure 4.7(b) shows results for the WCA system. Here again the data appears to have double exponential character starting near $T = 0.425$. We note for both models that this behavior occurs in the range identified as T_s by Ref. [133]. A more extensive study should test whether there is any difference using a smoothed WCA potential, which has slightly

different dynamical properties at low temperatures from those of the standard WCA (see e.g. Ref. [60]).

4.7.4 Finite size effects

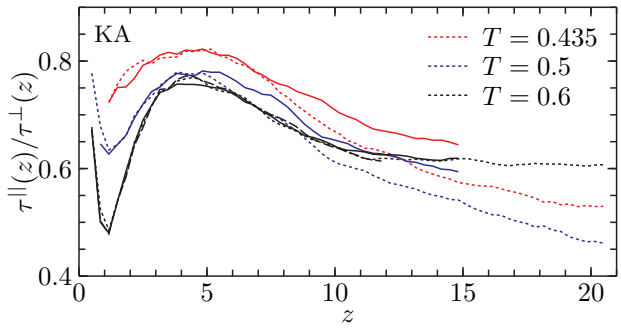

Figure 4.8: Ratio of parallel to perpendicular relaxation times in three different box sizes. The size used in the main text is indicated by a solid line, while data for a larger box size is shown with dotted lines, and for a smaller box at $T = 0.6$ by a dashed line, showing that finite size effects do not affect the crossover behavior at $T = T_s$ discussed in Sec. 4.4.

We have performed additional simulations to check that our conclusions are robust with respect to changes in system sizes. As an example of such tests, we consider the behavior of the ratio of perpendicular and parallel relaxation times for the KA system shown in Fig. 4.4(a).

In Fig. 4.8 we show the same calculation for the KA system using $N = 7600$ in a box with aspect ratio $1 : 1 : 4$. We also show at $T = T_s = 0.6$ the behavior for the $N = 5700$ system in an effectively smaller box, generated by freezing a wall of thickness $W = 9$ rather than $W = 3$ as in the main body of this article. While the large-z behavior seems to depend on the system size, the data up to $z_{\rm peak}$ appear to be independent of the box size considered. Hence we conclude that our approach to analyze the data in Fig. 4.4(e) to define T_s is safe, and that the existence of a correspondence between the crossover T_s of Ref. [133] and the present comparative study of parallel and perpendicular relaxation times is a robust finding.

Finally, we note that the large-z values of these data change with system size. We

believe that this is due to complex hydrodynamic coupling between the dynamics in the two directions. In fact, we found *in the bulk* that for $T < T_o$ in a non-cubic box, the ratio of $\tau^{||}(z)/\tau^{\perp}(z)$ is non-unity due to hydrodynamic effects (data not shown). For example, in the KA system, this ratio is approximately 0.85 for a $3:1:1$ box at temperatures $T \leq 0.8$. Study of the precise origin of this phenomenon is beyond the scope of this Chapter and will require further investigation.

Chapter 5

Correlation of local order with particle mobility in supercooled liquids is highly system dependent[1]

5.1 Introduction

Supercooled liquids display markedly heterogeneous dynamics, despite possessing structural properties that appear nearly unchanged from those of normal liquids from which they are prepared [4]. While there has been intense focus on understanding dynamical heterogeneity in a wide variety of systems, the structural origin of this phenomenon is not well understood [2, 8]. Simulations of model supercooled liquids are useful for understanding the connections between structure and dynamics because particle locations may be followed precisely for all times. Nonetheless, new theoretical tools are needed to filter out extraneous detail from the key structural and dynamical fluctuations in glassy systems.

One particularly useful simulation-based tool for quantifying the influence of structure on dynamics is the "isoconfigurational ensemble," where a large number of molecular dy-

[1] Adapted from the work published as arXiv:1402.6709 (2014).

namics (MD) simulations are initiated from the same starting configuration with momenta sampled randomly from a Boltzmann distribution [86, 87]. Under glassy conditions, spatial heterogeneities are immediately evident in the isoconfigurational displacement (or "propensity") field. A reasonable hypothesis is that particles with low propensity have a larger measure of local structural stability. Surprisingly, however, simple structural quantities, such as free volume and local potential energy, show little correlation with the heterogeneity of the propensity field [139]. In some models, localized soft modes [89–91] or unstable modes [140] appear to correlate strongly with propensity, but the degree of universality of this connection has not been thoroughly investigated.

Recently, focus has turned to the study of specific structural motifs and their putative connection with the dynamics of supercooled liquids. The notion that the frustration of local order incommensurate with bulk crystalline periodicity may be related to glass formation is an old one [141–144]. New evidence for the growth of domains associated with local packing motifs has been presented for several simple [145] and realistic model systems [146], where particles tend to be found in certain "locally preferred structures" (LPS) with increased supercooling. As a general rule, more fragile systems display a more rapid increase in LPS concentration and domain extent [145, 146]. In some systems, a correlation between the size and location of LPS and slow dynamics has been observed [147, 148], although the quantitative meaning of the correlations observed remains, in a statistical sense, obscure.

"Point-to-set" (PTS) correlations have emerged as an alternative quantifiable metric of amorphous ordering. PTS correlations measure the decrease of configurational entropy imposed by the presence of particles pinned in an equilibrium configuration [48, 116]. The length scale associated with PTS correlations has been demonstrated to grow upon increased supercooling in several systems [37, 116, 117], although its variation is rather modest over the dynamical range currently accessible in simulations [149], Nonetheless, several observations indicate that the growing PTS length scale should ultimately drive the dramatic increase in relaxation times in supercooled liquids [49, 150, 151]. It should be noted that PTS correlations, as well as other recently proposed measures of static correlations [152, 153],

are "order agnostic" [149] and therefore their growth does not necessarily connect to the emergence of specific local structures, such as those identified in the LPS studies.

In this Chapter we quantify the correlation between between static structure and dynamical heterogeneity in supercooled liquids in a statistically precise sense and within a coherent simulation framework. Our results indicate that scenarios connecting LPS cluster formation and glassy behavior [155, 156] cannot be generically correct. The observed model dependence suggests instead that local structural quantities play a key role in systems with large deviations from mean-field glassy behavior. Lastly, we show that a connection exists between growing PTS correlations and LPS in systems where LPS are strongly predictive of dynamical heterogeneity.

5.2 Models and methods

The first two models we will study are binary Lennard-Jones mixtures, namely the Kob-Andersen (KA) system [36] and the Wahnström (Wahn) system [41]. The definition of these models and their LPS statistics have been extensively detailed in Ref. [60]. The KA system is an 80:20 mixture while the Wahn system is equimolar. As a third system, we study a binary mixture of harmonic spheres (Harm) at a density such that that jamming is approached by lowering temperature near to zero [157]. In all cases, one species is smaller (B for KA and Wahn, A for Harm) and is intrinsically more mobile. Results for the small particles will be reported in the main text (Sec. 5.3) and for the large particles in Sec. 5.6. In the following, we will discuss all quantities using standard reduced units. Simulation details and a description of the LPS in each system can be found in Sec. 5.6.

While all of the above models are simple binary mixtures with short ranged interaction potentials, their local structures differ significantly. For each model, we identify particles participating in LPS through a Voronoi analysis (see Sec. 5.6). These LPS correspond to icosahedra, bicapped square anti-prisms, and distorted icosahedral structures in Wahn, KA, and Harm respectively. The relative abundance of these LPS at low temperatures is model

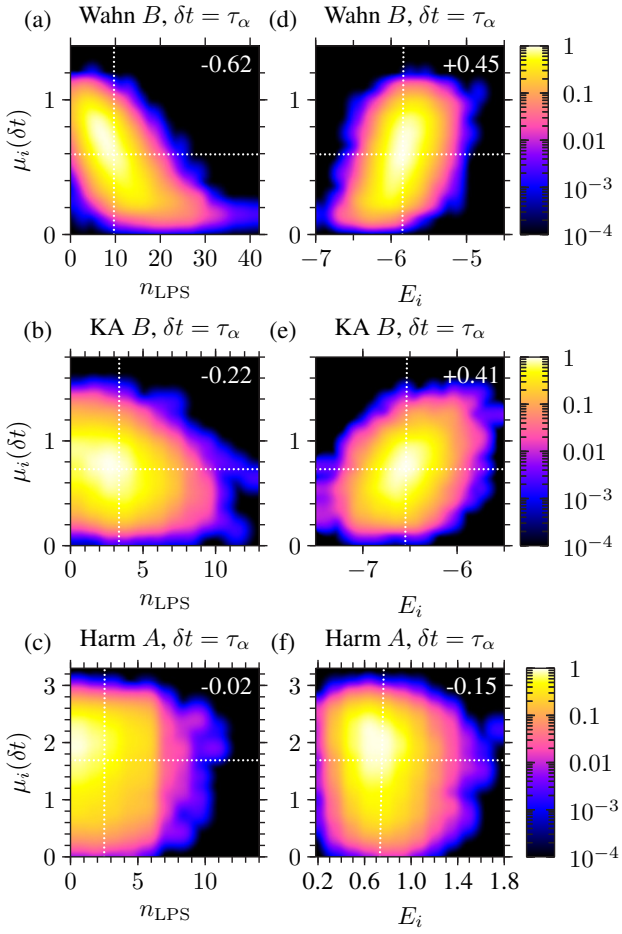

Figure 5.1: Interpolated histograms of particle mobility. Numbers at top-right indicate Spearman correlation coefficients K [154]. The first column shows the correlation between mobility and n_{LPS} with the LPS defined in the text. The second column shows correlation with E_i, the sum of a particle and its neighbors' pair energies. White dotted lines show the average value of the quantity on the horizontal and vertical axes.

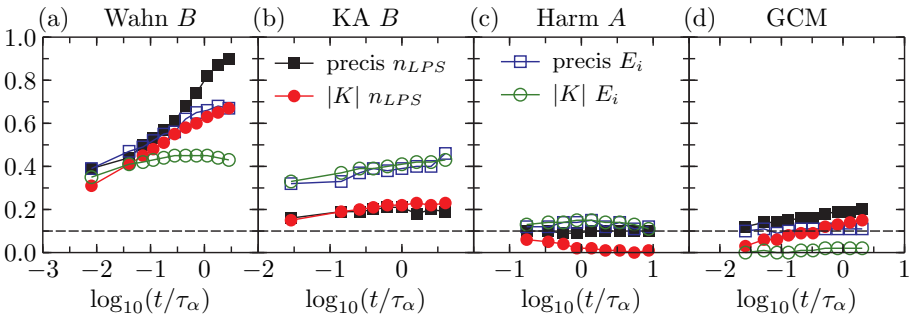

Figure 5.2: Time dependence of predictability metrics and correlation coefficients as a function of time for four models. Closed symbols correspond to data comparing mobility with $n_{\rm LPS}$ as in the left-hand column of Fig. 5.1 and open symbol comparing local energy E_i (defined in text) to mobility, as in the right-hand column of that figure. K is the Spearman correlation coefficient [154]. Precision is defined as the percentage of particles in the the top (bottom) 2% of $n_{\rm LPS}$ (E_i) which are in the bottom 10% of μ_i. Horizontal dashed lines show the result for the precision metrics which would result from random classification of particles as slow.

dependent: it is fairly significant in the Wahn model (about 10% of the particles are at the center of a LPS) and weaker in the other models. In the KA model this is due to the fact that twisted bicapped prisms are mostly centered around the small particles, which constitute the minority species.

In order to investigate the connection between the LPS in each system and dynamical behavior, we perform simulations in the isoconfigurational ensemble at supercooled temperatures, $T = 0.588$ for the Wahn, $T = 0.45$ for the KA and $T = 5.5$ for the Harm. These temperatures correspond roughly to the same degree of supercooling, as measured by the relative distance (about 3–6%) from their fitted Mode-Coupling temperatures, T_c (see Sec. 5.6).

We select 40 (20) equilibrated configurations for the LJ and Wahn (Harm) systems and perform the Voronoi analysis as discussed above. For each configuration, we performed 200 (100) NVT simulations in the isoconfigurational ensemble. From the simulations starting from each configuration, we compute the particle mobilities $\mu_i(t) \equiv \langle|\mathbf{r}_i(t) - \mathbf{r}_i(0)|\rangle_{\rm iso} \equiv \langle|\delta\mathbf{r}_i(t)|\rangle_{\rm iso}$. To quantify the number of LPS associated with a given particle, we count the

number of structures deemed locally preferred in a spherical region of radius l around each particle (n_{LPS}). All results reported here are nearly insensitive to this l value in the range we have investigated $1.5 \leq l \leq 3.0$, and we chose to report results only for $l = 2.5$.

5.3 Results

In Fig. 5.1(a)-(c) we show the combined probability distribution of μ_i and n_{LPS} for the 3 systems introduced above. We quantify correlation by using the Spearman correlation coefficient K [154], which has been used previously in a similar context [139]. K is 1 if two quantities are related by a monotonically increasing function and -1 if by a decreasing one. K values are shown in the top-right corner of each histogram. We see visually and quantitatively that the correlation is much stronger in the Wahn system than in the LJ and Harm systems. For comparison, the probability distributions for correlation between mobility and local energy ($E_i = e_i + \sum_{j \in \mathrm{neigh}(i)} e_j$) are shown in Fig. 5.1(d)-(f). Correlation is fairly significant in the two LJ mixtures and much weaker in the Harm system.

Close inspection of Fig. 5.1(a) reveals a long tail in the histogram of n_{LPS} values. From these data, we can predict that a particle in a domain rich in icosahedral structures will be very immobile. Looking at the data at $n_{\mathrm{LPS}} = 0$ instead, we see that such particles will have higher than average mobility. However, slow and fast particles have a wide range of n_{LPS} values. In Fig. 5.2 we show the level of "precision" [154] in predicting which particles are slow based on n_{LPS} and E_i for the models studied, as well as the K values. Here, precision is defined as the percentage of particles in the top (bottom) 2% of n_{LPS} (E_i) which are also in the bottom 10% of $\mu_i(\delta t)$. In Sec. 5.6 we show results for predicting which particles will have low mobility. All trends discussed are insensitive to the particular percentiles chosen for this definition of precision.

When viewed from this statistical perspective, several striking features are observed. For the Wahn system, LPS are highly predictive of slow dynamics. In particular, using our definition of precision one may "predict" the location of slow particles with near perfect accuracy

up to τ_α, and such a correlation continues to grow to the longest times we investigated. In the KA system, local energy is more predictive of slow dynamics than LPS locations, and correlation for both local energy and n_{LPS} in KA and Harm are far lower than in the Wahn system.

We may thus conclude that the correlation between dynamics and local structural metrics such as n_{LPS} is highly system dependent. What may be taken from this dramatic degree of variability? Among the three models studied, the Wahn system shows the largest departures from mean-field behavior. Namely, Wahn exhibits large violation of the Stokes-Einstein relation, sizable deviations from time-temperature superposition, and large inconsistencies between fitted Mode-Coupling exponents [158] (see Sec. 5.6). From this perspective, the KA system shows moderate deviations from mean-field behavior. Finally, although the Harm system does not uniformly display mean-field behavior, finite size effects [128] and the existence of non-monotonic dynamical length scale [157] suggest that its properties are largely harmonious with the mean-field paradigm. A discussion of how mean-field behavior may be tuned by the interatomic potential is contained in Sec. 5.6.

This trend suggests a connection between a high degree of local structure-dynamics correlation with strong spatial fluctuations that manifest in deviations from mean-field behavior. To further test this notion, we study a fourth system, the high-density ($\rho = 2.0$) Gaussian Core Model (GCM). The GCM is a single-component fluid with Gaussian repulsions [42, 159], which has all the hallmarks of glassy behavior while matching mean-field predictions of dynamical exponents, strongly suppressed non-Gaussian fluctuations and minimal Stokes-Einstein violation [42]. This mean-field behavior seems to arise naturally from the long ranged and ultra-soft interaction potential (see discussion in Sec. 5.6).

In Fig. 5.2(d) we show results for $N = 3456$ Gaussian core particles at $T = 3.2$ with 100 isoconfigurational runs initiated from 20 independent configurations. We note that this temperature is slightly higher, relative to $T_c = 2.7$, than the one used in the other models, but corresponds instead to the same relative increase in relaxation time as observed for the Wahn system (see Sec. 5.6). We found that distorted crystal-like structures constitute the

LPS of the model (the underlying stable crystal at the studied density is BCC). In agreement with our expectations, the correlation between n_{LPS} and dynamics in the GCM system is very low, just as in the Harm system, and only marginally improves as t increases.[2]

It would be natural to speculate that in systems such as the Harm and GCM models, there simply exists *no* connection between structure and dynamics. However, this statement is incorrect. We have used the "R_4-ratio" analysis of Berthier and Jack [160] to quantify the structural component of the dynamic fluctuations. As detailed in Sec. 5.6, we found that all 4 systems analyzed in Fig. 5.2 show a marked correlation between structure and dynamics, despite the fact that no *specific* structural motif connects to dynamics in the more mean-field like models. These striking results will be a subject for future investigations. Here we just point out an interesting analogy with the behavior of mean-field p-spin models [161], which *do* display large values of R_4 close to the dynamic transition.

One may take the inability of specific structural metrics, such as LPS determined from Voronoi analysis, to correlate universally with dynamics in supercooled liquids as an indication that a more general form of growing amorphous order must be implicated. In the remainder of this Chapter we focus on structural correlations embodied in "point-to-set" and related length scales [37, 117, 150, 151]. In order to show that this type of order may subsume specific structural metrics, we investigate the connection between local order as measured by n_{LPS} and PTS correlations.

The PTS length scale is extracted by calculating the range over which spatial correlations imposed by an equilibrium amorphous spherical boundary decay. We first establish that it is possible to ergodically sample cavities at some R_{cav} using the "Particle Size Annealing" (PSA) method detailed in Ref. [117]. In brief, we monitor the overlap q, a measure of the similarity between the initial configuration in the cavity and that at a later time t. The

[2] It may appear that the correlation between n_{LPS} and dynamics in both the KA and GCM system are superficially similar. However, the LPS in the GCM system are simple crystalline motifs that exist because of the difficulty of avoiding such particle arrangements in a monatomic system. In this sense, we view the correlation of *both* n_{LPS} and E_i as significantly weaker in the GCM system when compared to LJ.

overlap is defined as $q(R_{cav}, t) = (\rho l^3 \tilde{N})^{-1} \sum_{i=1}^{\tilde{N}} \langle n_i(t) n_i(0) \rangle$ where the center of the cavity has been tiled into $\tilde{N} = 125$ cubes of side length $l = 0.36$, small enough such that the cell occupancy $n_i(t)$ is always zero or one. We use both regular Monte Carlo (MC) sampling and a sampling where the particle diameters are shrunk to 60% of their original size and grown back in, and check that the q values agree at long times. In the limit of large cavity and long time, $q(t)$ will tend to the bulk value $q_b = \rho l^3$ and so this value is conventionally subtracted from q.

In Fig. 5.3(a) we show that for $R_{cav} = 3.0$, q is sampled ergodically. We then take 30 of the Wahn configurations used earlier and perform two standard MC simulations for cavities centered at 27 positions in each. The longtime overlap value is extracted from each cavity, and the number of icosahedral centers within the cavity as well as the one within the inner $R = 2.5$ of the cavity, are calculated. We find that high overlap cavities generally have high n_{LPS} and *vice versa*. This implies that (for the Wahn system) the cavity simulations are mostly probing the same type of local ordering measured by the Voronoi construction, although it does not necessarily mean that the correlation *length* measured by doing cavity simulations at a series of radii is the same as would be measured by the extent of LPS domains.

5.4 Conclusions

In conclusion, we have demonstrated that the correlation between local structural metrics (e.g. E_i and n_{LPS}) and dynamics in supercooled liquids is highly system dependent. In models such as the Wahn mixture, accurate predictions of heterogeneous dynamics may be made on the basis of a single structural marker while essentially no correlation exists in mean-field like systems such as the GCM. However, a strong link between *some* aspect of static structure and dynamics does exist, as signified by the sizable R_4-ratio observed in all the systems we have studied. Despite being "order agnostic," PTS correlations appear to show a connection with specific types of local order such as Voronoi signatures in systems

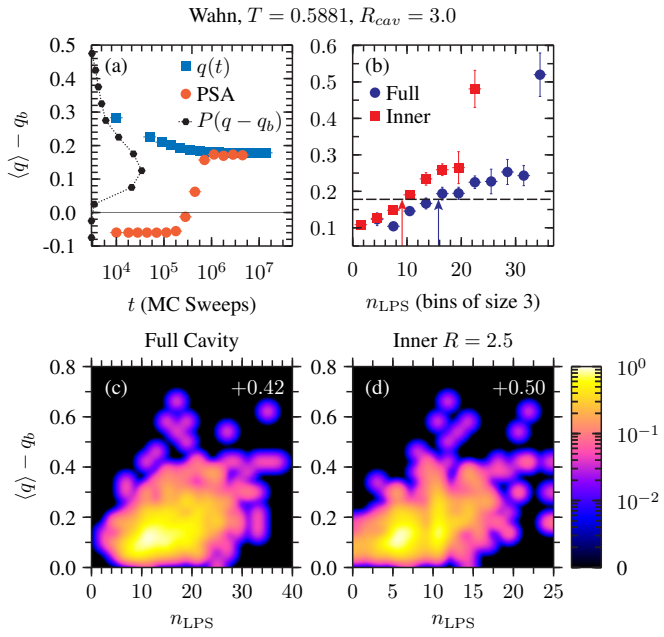

Figure 5.3: (a) Cavity overlaps and PSA overlaps (with the value for a bulk system q_b subtracted) indicating ergodic sampling at this cavity size and temperature. The dashed line shows the overlap probability distribution $P(q - q_b)$. (b) On average, cavities containing a large number of LPS centers have high overlap. "Inner" points count only LPS which are within $R = 2.5$ of the center of the cavity. Dashed line shows the average overlap and arrows show the average number of LPS. (c) and (d) show the full data distribution and Spearman correlation coefficients [154]. The data in (b) is obtained from (c) and (d) by averaging over vertical slabs of width 3.

whose dynamics may be predicted by the location of such structural motifs. Furthermore, previous work has detected an apparent connection between the growth of relaxation times and "order agnostic" length scales in systems where the connection between relaxation times and specific structural metrics is not very strong [117, 150, 151]. These facts suggest that PTS correlations may provide a more general description of the key static fluctuations that determine dynamical behavior in supercooled liquids.

5.5 Acknowledgments

I thank Mark Ediger and Asaph Widmer-Cooper for stimulating discussions. Simulations were executed in part on the Midway cluster at the University of Chicago's Research Computing Center, and on the seeder cluster of the University of Chicago Computing Cooperative (UC3), supported in part by the Open Science Grid, NSF Grant No. PHY-1148698. LAMMPS [105] simulations were organized and executed using the Swift parallel scripting language, development supported by NSF Grant No. OCI-1148443 [64].

5.6 Supplemental information

5.6.1 Models, units and relevant temperatures

The Kob-Andersen (KA) [36] and Wahnström (Wahn) [41] models are binary Lennard-Jones mixtures where particles interact through the potential

$$u_{\alpha\beta}(r) = 4\epsilon_{\alpha\beta}\left[\left(\frac{\sigma_{\alpha\beta}}{r}\right)^{12} - \left(\frac{\sigma_{\alpha\beta}}{r}\right)^{6}\right], \tag{5.1}$$

where $\alpha, \beta = A, B$ are species indices. For the KA model the interaction parameters are $\sigma_{AB} = 0.8\sigma_{AA}$, $\sigma_{BB} = 0.88\sigma_{AA}$, $\epsilon_{AB} = 1.5\epsilon_{AA}$, and $\epsilon_{BB} = 0.5\epsilon_{AA}$, while for the Wahn model $\sigma_{AB} = 0.916\sigma_{AA}$, $\sigma_{BB} = 0.833\sigma_{AA}$, and $\epsilon_{BB} = \epsilon_{AB} = \epsilon_{AA}$. The chemical composition is $x_1 = 1 - x_2 = 0.8$ for the KA model and $x_1 = x_2 = 0.5$ for the Wahn model. The mass ratio m_1/m_2 is 1 and 2 in KA and Wahn, respectively. The potentials are cut and shifted at

$2.5\sigma_{\alpha\beta}$. In the main text, σ_{AA}, ϵ_{AA}, and $\sqrt{m_A\sigma_{AA}^2/\epsilon_{AA}}$ are used as units of distance, energy, and time, respectively.

The Harm model is an equimolar mixture of elastic spheres [162] with equal masses m. The interaction potential is given by

$$u_{\alpha\beta}(r) = \frac{\epsilon}{2}\left(1 - \frac{r}{\sigma_{\alpha\beta}}\right)^2, \tag{5.2}$$

if $r_{\alpha\beta} < \sigma_{\alpha\beta}$ and zero otherwise. The interaction parameters are $\sigma_{AA} = 1$, $\sigma_{AB} = 1.2$ and $\sigma_{BB} = 1.4$. As in the KA and Wahn models, σ_{AA} and $\sqrt{m\sigma_{AA}/\epsilon}$ are used as units of length and time, respectively. The unit of energy is $10^{-4}\epsilon$.

The Gaussian core model [163, 164] (GCM) is a one-component fluid of particles interacting via a Gaussian potential

$$u(r) = \epsilon e^{-(r/\sigma)^2}.$$

The potential is cut and shifted at $r = 5\sigma$. The units of length, energy and time are given by σ, $10^{-6}\epsilon$ and $\sqrt{m\sigma_{11}/\epsilon}$ respectively.

The simulations have been carried out using the LAMMPS package [105]. Integration time steps δt used were 0.004 for the Wahn and LJ system, 0.1 for Harm, and 0.4 for the GCM. Temperature was maintained by a Nosé-Hoover thermostat with a time constant of 100 δt in all cases.

The estimated Mode-Coupling critical temperatures of all the models and the wave-vectors k used to compute the structural relaxation times τ_α (see section on R_4 values) are reported in Tab. 5.1. The estimated critical temperatures were obtained, in the references cited in in Tab. 5.1, from power law fits to the relaxation times data.

5.6.2 Identification of locally preferred structures

Particles participating in LPS are identified through a Voronoi analysis [60]. To characterize the local structure around a given particle, we determine the number n_k of faces having k edges of the Voronoi polyhedron formed by the nearest neighbors. Each particle may therefore be labeled by a Voronoi signature (VS) $(n_3, n_4, n_5, ..)$, where n_3 is the number of

triangles, n_4 the number of quadrilaterals, etc. of the corresponding Voronoi polyhedron. As in Ref. [60], we focus on the polyhedra found around type B particles, whose temperature variation were shown to correlate better with slow dynamics. In the Wahn system, the $(0, 0, 12)$ polyhedron (icosahedron) appears around over 25% of type B particles at low temperatures, while the second most common VS, $(0, 2, 8, 1)$, appears around approximately 9% of B particles. In the KA system, the $(0, 2, 8)$ arrangement (bicapped square antiprism) appears around approximately 10% of small particles and the $(1, 2, 5, 3)$ appear around 8%. It is important to remember that, because the KA system is an 80:20 mixture, the $(0, 2, 8)$ motif is found in only about 2% abundance while more than 10% of Wahn particles are found in $(0, 0, 12)$ configurations. We therefore considered the union of $(0, 2, 8)$ and $(1, 2, 5, 3)$ polyhedra as the LPS of KA model. The analysis carried out in the main text remains qualitatively unchanged if only $(0, 2, 8)$ are considered. In the Harm system, the most frequent signature at low temperature is $(0, 2, 8, 2)$, which may be regarded as a distorted icosahedral structure. The abundance of this LPS is about 5% at the lowest studied temperatures, while the second most frequent signature is $(0, 2, 8, 1)$ has 4%. In the GCM, we found a variety of low symmetry polyhedra, some of which are found in FCC and BCC crystals at finite temperatures [165]. At the studied temperature, $(0, 3, 6, 4)$, $(0, 2, 8, 4)$, and $(0, 4, 4, 6)$ (ideal FCC structure) are the most abundant ones. These crystal-like structures tend to grow slightly by decreasing temperature and their union is considered as the LPS of the model.

5.6.3 Mean-field behavior and pair potential

As mentioned in the body of the text, the Harm and GCM systems seem to embody manifestations of the predictions of mean-field theories of glasses, however they do so in distinct ways. The Harm system shows a well defined crossover between seemingly "activation-less" and "activated" regimes as predicted by the mean-field perspective. However, SE violation is still pronounced in the Harm system (see Fig. 5.4). In this sense, "critical" fluctuations expected in finite dimensions [166] are still sizable. In the GCM system, the entire range of temperatures that can be simulated displays a near-complete, quantifiable correspondence

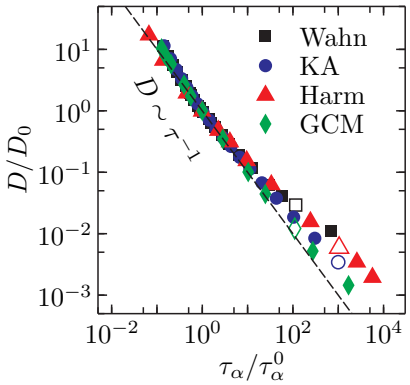

Figure 5.4: Diffusion constants vs. τ_α (see SI text) for each of the four models. Open symbols represent the temperatures studied in the main body of this work. The diffusion constants D were extracted from the limiting relationship $\lim_{t\to\infty} \delta\mathbf{r}_i^2(t) = 6Dt$. The values of the diffusion constants and τ_α are scaled by their value at the approximate onset temperature of glassy behavior, with T_0 values used here of 1.0, 1.0, 12 and 5 for the Wahn, LJ, Harm and GCM respectively. The dashed line shows the approximate high temperature behavior $D \propto \tau^{-1}$.

with high dimensional mean-field behavior, including the absence of Stokes-Einstein violation (despite the GCM system being highly "fragile"). Both potentials share an ultra-soft core, which prevents the physics from being dominated by harsh short-ranged repulsions. In addition, the GCM potential is (quasi) long-ranged, mimicking the effect of increased dimensionality [159, 167–169]. Thus ultra-softness may be a necessary condition for triggering aspects of mean-field behavior. However, to further suppress critical-like fluctuations in low dimensions, a (quasi) long-ranged potential, as found in the GCM, is also necessary.

5.6.4 R_4 values

In order to quantify the total connection between structure and dynamics we perform the analysis of Berthier and Jack (Ref. [160]). They definite the quantity $R_4(t)$ which represents the fraction of the total run-to-run variance in a dynamical quantity from analyzed in the isoconfigurational ensemble which is encoded by the initial configurations. Hence a value of zero means all fluctuations come from the randomly selected initial velocities while a value

System	T_c	k	$\delta_4(\tau_\alpha)$	$\chi_4(\tau_\alpha)$	$R_4(\tau_\alpha)$
Wahn	0.56 [170]	7.7	5.60	8.99	0.623
KA	0.435 [36]	7.25	13.3	21.4	0.620
Harm	5.2 [157]	6.28	3.61	9.20	0.392
GCM	2.7 [42]	8.40	8.08	18.9	0.428

Table 5.1: Predictability ratio results for the four systems studied. See Ref. [160] and Sec. 5.6 text for further discussion.

of unity means that all fluctuations in the dynamical quantity are determined by the initial structure. R_4 is defined as,

$$R_4(t) = \frac{\delta_4(t)}{\chi_4(t)}, \tag{5.3}$$

where

$$\delta_4(t) = N\{\mathbb{E}[\langle F(t)\rangle_{\text{iso}}^2] - \mathbb{E}[F(t)]^2\} \tag{5.4}$$

$$\chi_4(t) = N\{\mathbb{E}[\langle F^2(t)\rangle_{\text{iso}}] - \mathbb{E}[F(t)]^2\}. \tag{5.5}$$

Here, "F" is a collective dynamical quantity, a function averaged over all particles. $\mathbb{E}$ represents an equilibrium ensemble average while $\langle\cdots\rangle_{\text{iso}}$ represents the isoconfigurational average over realizations of momenta. here we choose $f(t)$ to be the self-intermediate scattering function $f_s(k,t) = \frac{1}{n}\sum_{i=1}^{n} e^{\mathbf{k}\cdot\delta\mathbf{r}_i(t)}$. the relaxation time τ_α is defined by $f_s(k, t \equiv \tau_\alpha) = 1/e$. for the four systems studied in this Chapter, we report the results of the r_4 analysis at $t = \tau_\alpha$ in tab. 5.1. for all four systems, we find values that should be considered large based on prior analyses using this quantity, though as would be expected from our other results and discussion, it is smaller in the Harm and GCM systems than in the two LJ systems.

5.6.5 Mobility correlation and predictability

For completeness, in Fig. 5.5 we present histograms for the GCM data analogous to that of Fig. 5.1. In Fig. 5.6 we show the histograms for both the A and B types of particles for

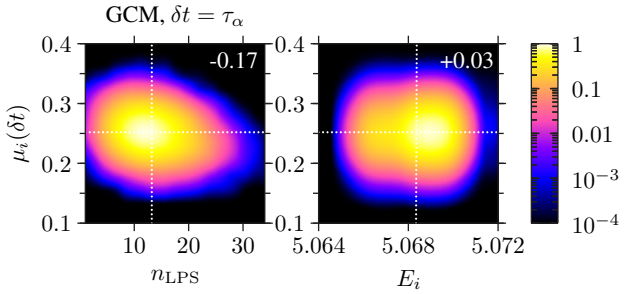

Figure 5.5: Mobility μ_i and local energy E_i vs. n_{LPS} histogram for the GCM as in Fig. 5.1.

the three binary systems presented in Fig. 5.1. Lastly, in Fig. 5.7 we show the results for predictability of the fastest 10% of particles based on the lowest 2% of n_{LPS} or the highest 2% of E_i for contrast with Fig. 5.2. For comparison, the same data for K as in Fig. 5.2 are also shown.

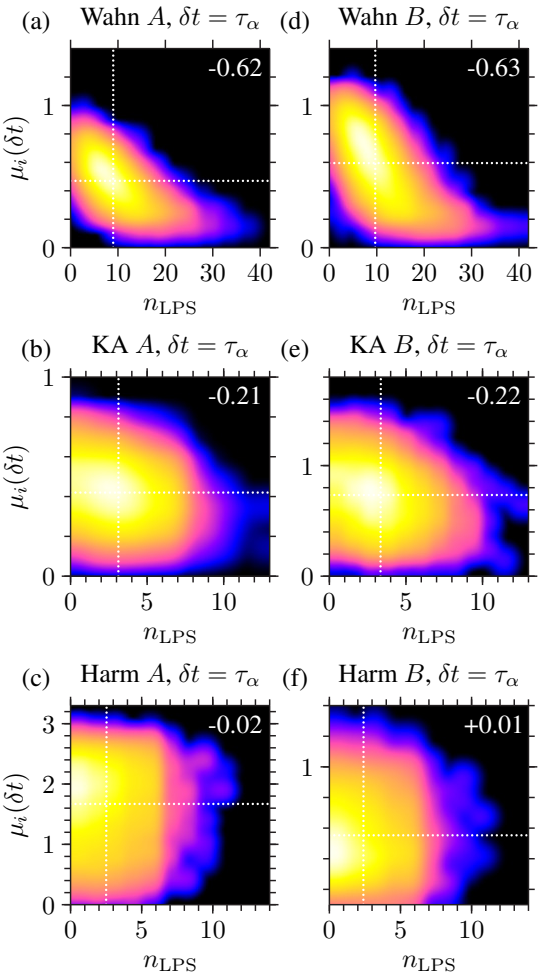

Figure 5.6: Mobility μ_i vs. n_{LPS} histogram for the three models in Fig. 5.1 comparing both species of particles. The larger particle always has a smaller range of dynamical activity (note the differing ranges of vertical axes) and this intrinsically reduces the correlation.

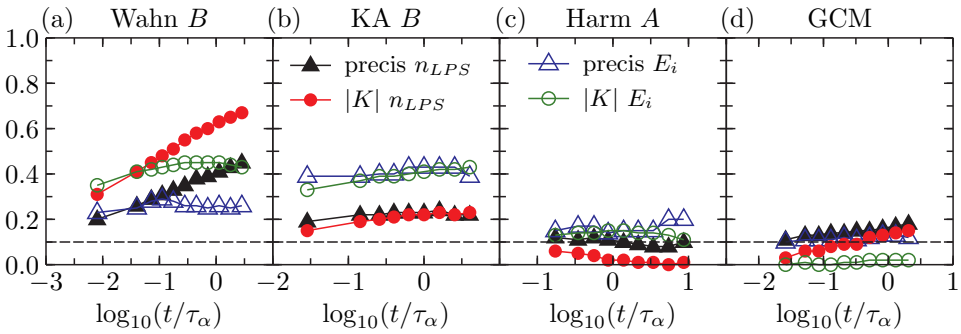

Figure 5.7: Same as Fig. 5.2 except the precision in that figure, the precision of prediction the slowest 2% of particles, has been replaced by the precision of predicting the fastest 2% of particles based on a lack of local stability (high E_i, small $n_{\rm LPS}$). We see that the trends are all the same as for the "slow precision", however, the "fast precision" is much worse for both n_{LPS} and E_i in the Wahn model, reflecting the wider density at the left and than on the right end in Fig. 5.1. In contrast, the precision for the KA system does not change much reflecting the more ovular shape of the density in Fig. 5.1.

Chapter 6

Equilibrium ultrastable glasses produced by random pinning

6.1 Introduction

Recently, glasses with remarkable thermodynamic and kinetic stability have been prepared by vapor deposition on substrates maintained below the conventional glass transition temperature, T_g, of the bulk liquid [171, 172]. It is estimated that these "ultrastable" glasses (USGs) occupy states that are so low in the energy landscape that it would take several decades of conventional annealing of bulk amorphous samples to prepare equivalently stable glassy materials [171, 173]. In addition to potential technological applications of these materials [173], the ability to prepare USGs poses new challenges for theory and thus opportunities for gaining a deeper theoretical understanding of amorphous materials.

A framework for rationalizing the formation of USGs has been put forward by Ediger and coworkers. Specifically, they have hypothesized that deposition on a cold substrate combined with enhanced mobility at the free surface allows the system to effectively burrow to deeper free energy minima [171, 173]. Computational studies using facilitated lattice models, simulations of Lennard-Jones systems, as well as theoretical results based on Random First Order Theory (RFOT) have demonstrated phenomenology in concordance with these

ideas [174–177]. By inhabiting deeper basins on the energy landscape, USGs are in some sense closer to the putative Kauzmann or "ideal glass transition" temperature (T_K). This idea has been quantified by experimental estimation of fictive temperatures (T_f) that lie well below T_g [171]. Ultrastable glasses may thus provide an experimental means of producing an amorphous material whose configurational entropy approaches that of its crystalline counterpart.

As difficult as it is to experimentally produce annealed glasses at temperatures that approach T_K, it is all the more so *in silico*. Even the most powerful computers and computational methodologies cannot simulate model supercooled liquids that approach T_g, let alone T_K, although work mimicking vapor deposition protocols as well as the use of biased sampling of trajectories have moved us closer to this goal [176–179]. Recently, however, theoretical ideas have been put forward that potentially make accessing and testing the behavior of "ideal glass" states possible. In particular, Cammarota and Biroli have proposed that within RFOT, random pinning of particles may produce a Random Pinning Glass Transition (RPGT) which has the characteristics of an ideal glass transition [52]. Crucially, the RPGT is speculated to occur at temperatures accessible in computer simulations because pinning a fraction f of the particles effectively increases the glass transition temperature $T_K(f)$ [52]. With this motivation, we hypothesize that it should be possible to form glasses in equilibrium via random pinning that share many properties with ultrastable glasses formed in the laboratory via nonequilibrium vapor deposition techniques. To test this hypothesis, we study behavior of these pinned liquids upon heating, which yields critical new insights into the properties of deeply supercooled liquid states.

6.2 Results

Here, we study the properties of the two-dimensional 65:35 Kob-Andersen Lennard-Jones system, which has been previously shown to be stable against crystallization and thus serves as a good model supercooled liquid [98, 180]. Studying the two-dimensional system rather

than the more standard three-dimensional one [36] allows us to directly visualize the spatial variation in observables. We have prepared many equilibrated supercooled configurations with $N = 10000$ and density $\rho = 1.2$ at temperature $T = 0.425$ and subsequently fix the position of a percentage f of particles as described in Sec. 6.4.

6.2.1 Calorimetry

The quenched disorder from random pinning of particles, by necessity, restricts the system to one region of phase space. With respect to this initial configuration, we expect any other configurations of similar energy to be rare and thus difficult to access. In this respect, the configuration we produce effectively behaves as if they are very low in the energy landscape *within the constraints imposed by the pinned particles*, and we will refer to our pinned samples as "pinned glasses" (PGs). In order to quantify the energetic stability of our pinned samples, we mimic the experimental technique of scanning calorimetry used to study USGs. To perform these experiments we heat, then cool, then reheat the sample again at constant rate γ from initial temperature T_i to a maximum temperature of $T = 2.0$. In Fig. 6.1(a) we show the results of this heating and cooling for samples with $f = 5$ and $f = 10$. Upon heating, the system stays on the "glass branch" over some range of temperatures, and then melts and collapses onto a "liquid branch." On cooling, the samples do not return to the original glass branch but to one higher in energy. Very little hysteresis is observed upon reheating, showing that this new sample is no longer very glassy. We also observe that the simulations for larger f need to be heated to a much higher temperature before they "melt" than do the simulations with smaller f, and additionally that the difference in energy between the original sample and re-annealed sample is larger for larger f. Differential scanning calorimetry experiments on USGs look quite similar, with the conditions under which the USG was prepared determining how high above the standard T_g they must be heated before converting into a liquid.

By taking the numerical derivative of the heating curves, we can extract the heat capacity of the pinned samples, shown in Fig. 6.1(b). We see that the peak temperature, the temperature at which the sample "melts," moves to higher temperature with increasing f and

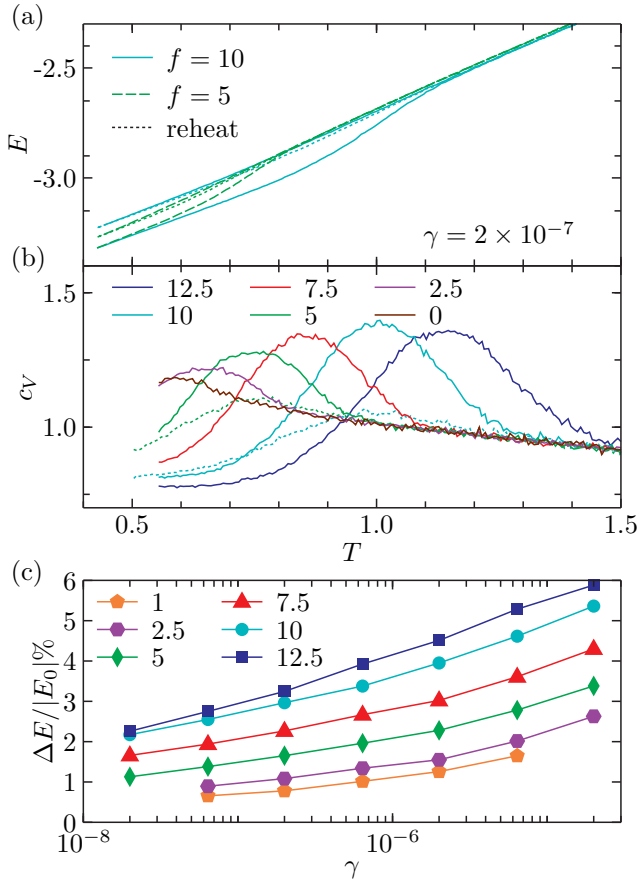

Figure 6.1: (a) The average energy per particle of Samples created with $f = 5$ or $f = 10$ percent of particles heated from $T_i = 0.425$ to $T = 2.0$ and then cooled back down at a constant rate γ. (b) Heat capacity per particle, with solid lines for initial heating and dotted lines for reheating at $f = 5$ and $f = 10$. (c) Energy gap at T_i after heating and cooling at rate γ for different pinning fractions f, symbols shown in the key. Jackknife errorbars are smaller than the symbols.

the peak height grows with f. In particular, the peak height continues to increase relative to its baseline value near T_i. Heat capacities for the re-annealed samples (dotted) are much smaller, providing verification that re-annealed samples occupy higher energy states. The peaks in the heat capacities of the re-annealed PGs lie approximately under those from the initial heating, in contrast to what is seen for USGs, where the re-annealed samples melt at substantially higher temperature than the vapor deposited ones. We attribute this to the fact that for USGs, the state to which the sample relaxes is a normal supercooled liquid or glass, whereas in the high T state of the PG, the pinned particles remain in place.

The energy gap between the initial and re-annealed PG depends on the rate at which the annealing is performed. In particular, the gap shrinks for slower cooling. In Fig. 6.1(c) we show the energy gap at T_i, ΔE, normalized by the average initial energy-per-particle E_0. In all cases, we observe $\Delta E > 0$, with gaps that increase with increasing f. Extrapolation of these curves, even for small f, suggests that it would take γ values significantly smaller than those used here (with simulation times certainly exceeding 1 cpu-year) to re-anneal our samples to their initial energies, thus illustrating the intrinsic stability of PGs.

6.2.2 Melting

A unique feature of PGs is that they are equilibrium supercooled samples, namely their dynamics lack a non-equilibrium driving force and exhibit no aging if the dynamics are simulated at T_i. Unfortunately, for most temperatures and values of f, relaxation times will be inaccessibly large [124, 181]. Here we instead choose to study the response of PGs to a change in temperature, with the subsequent dynamics now being out of equilibrium. In order to monitor the response to heating, we compute the self-overlap function for the for N_u unpinned particles,

$$q_s(t, t_w) = \frac{1}{N_u} \sum_{j=1}^{N_u} q_j(t, t_w), \tag{6.1}$$

$$q_j(t, t_w) = w(|\mathbf{r}_j(t + t_w) - \mathbf{r}_j(t_w)| - a), \tag{6.2}$$

where t_w is a waiting time, $w(x)$ is the window function which is unity for $x \leq 0$ and zero for $x > 0$. We can define the self-overlap relaxation time τ_s for a given T by $q_s(\tau_s, 0) \equiv 1/e$. In this case we chose $a = 0.22$ where we find the equilibrium relaxation with $f = 0$, $\tau_s(T = 0.425)$ corresponds to the τ_α as measured in Ref. [180].

The relaxation of samples heated to T becomes drastically slower as f is increased. This is shown for $T = 1$ in Fig. 6.2(a). In addition, a plateau develops and grows in height suggesting a more stable glass, which as also been observed for pinned samples in equilibrium [124, 181]. As the waiting time increases, the system relaxes towards a high temperature liquid state as shown in Fig. 6.2(b).

The overlap relaxation time $\tau_s(T, f, t_w)$ can serve an indicator of the progress of melting. In Fig. 6.2(c), we show the overlap relaxation time for each f after waiting time t_w. The relaxation time becomes independent of t_w, indicating that the system has reached equilibrium. We define the the transformation time t_{trans} as the time where $\tau_s(T, f, t_w)$ has fully decayed to this plateau value, which we term τ_α, in analogy to how it has been defined for USGs [182, 183]. We find inspection of the decay of $\tau_s(T, f, t_w)$ to determine t_{trans} is imprecise, but have observed that $q_s(t_{\text{trans}}, 0, T) \equiv 0.01$ serves as a consistent proxy definition across all f and T and is a simpler and more accurate tool for the extraction of t_{trans} than is inspection of the τ_s curves shown in Fig. 6.2(c).

With increasing f, we observe a substantial increase in t_{trans} relative to that for the unpinned sample. For example, the data in Fig. 6.2(c) show an increase of a factor of $\approx 10^3$. We believe this quantity could be used to quantify the stability of PGs or USGs. In recent studies of USGs, however, a *different* ratio, that of $t_{\text{trans}}/\tau_\alpha$, has been used to characterize the stability of the stable glass relative to that of the supercooled liquid [183]. In Fig. 6.2(c) we observe $t_{\text{trans}} >> \tau_\alpha$ for all f. In Fig. 6.3(a) we compare these two values for all (f, T) points studied. On average we find $t_{\text{trans}} \approx 100\tau_\alpha$ for these data, with the maximum ratio being ≈ 300. In the case of PGs, we see that the denominator of this expression increases substantially over the unpinned supercooled liquid. The increase of these two quantities in tandem suggests that the barrier to transformation from the PG to

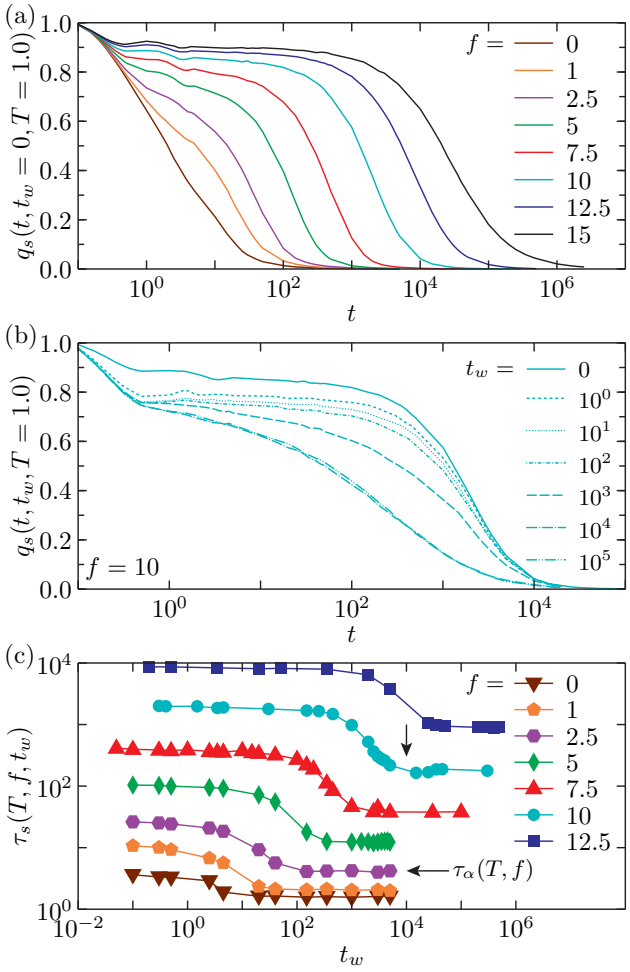

Figure 6.2: (a) Self overlap relaxation times for the instantaneous ($t_w = 0$) heating of samples to $T = 1$ for a given value of f. Curves decay more slowly as f increases, with an increasing plateau height. (b) Self-overlap relaxation time for $f = 10$ with $T = 1$ after waiting a time t_w specified in the legend. The overlap decays faster at longer waiting times, eventually converging. (c) The self-overlap relaxation times τ_s extracted for different waiting times. Curves move upward with increasing f. Examples of quantities t_{trans} and τ_α defined in the text are indicated by the vertical arrow and horizontal arrow, respectively.

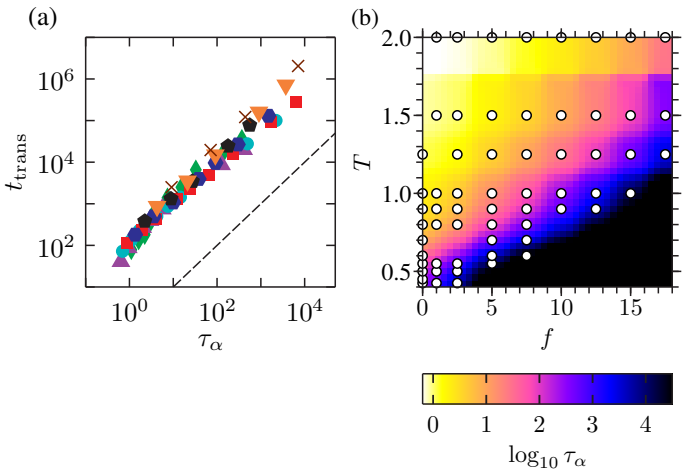

Figure 6.3: (a) Scatter plot of $t_{\rm trans}$ and τ_α as described in the main text for all f and T computed. The symbols and colors are the same as in Fig. 6.2. Dashed line indicates $t_{\rm trans} = \tau_\alpha$. (b) τ_α values for the same set of simulations are shown displayed as a color map with values of $\log_{10}\tau_\alpha$ interpolated between the points where simulations were performed, represented by open circles. Pinned glasses produced at $T_i = 0.425$ lies in a (black) region that is not accessible at equilibrium by conventional means.

the pinned liquid with increasing f may have the same origin as the increase in relaxation times in the equilibrium pinned liquid. The wide range of τ_α is highlighted in Fig. 6.3(b) and there is a clear difference in character between the equilibrium pinned liquid relaxation curve in Ref. 6.2(b) as compared to the unpinned liquid shown in Ref. [180]. We again remark that although the PGs we have produced appear to be good representatives of USGs, their equivalent high temperature states are not the standard supercooled liquids of the KA system.

6.2.3 Spatial Heterogeneity

Given the stability of PGs, and the aging behavior exhibited in Fig. 6.2, we expect to see pronounced dynamical heterogeneity in our simulations. In order to demonstrate this, we first show the spatial distribution of $q_j(t = \tau_{1/2}, t_w = 0, T)$, where $\tau_{1/2}$ is the time at which $q_s(t = \tau_{1/2}) = 1/2$. Fig. 6.4(a-d) shows snapshots for $f = 0$, 2.5, 5, and 10

where the color of the particles represents q_j averaged over a local region of radius 1.5, i.e. $\tilde{q}_j(t) = \sum_l q_l(t) w(|\mathbf{r}_l(0) - \mathbf{r}_j(0)| - 1.5)$. In all cases, half of the particles have $q_j = 1$ and half have $q_j = 0$. As f increases, we see that the regions that have melted or remain stuck grow in connectivity. Theory suggest that the activation barrier to collective dynamical relaxation increases with increasing f, and we therefore hypothesize that the resulting ability of a sample to initially relax becomes more and more dependent on regions of slightly enhanced mobility, what one might call localized "defects" or "soft-spots", to nucleate melting.

To quantitatively check the result suggested by visual inspection of Fig. 6.4(a-d), we compute the dynamical structure factor which measures the scattering off of these domains,

$$S_4(k, t, t_w, T) = \frac{1}{N} \left\langle \sum_{j,l} q_j q_l e^{i\mathbf{k}\cdot(\mathbf{r}_l(0) - \mathbf{r}_j(0))} \right\rangle, \tag{6.3}$$

where q_j is shorthand for $q_j(t, t_w, T)$ defined in Eq. 6.2. The resulting profiles shown for one temperature in Fig. 6.4(e) have larger spatial variation measured by $S(k \to 0, t)$ with increasing f. This reveals a growing non-equilibrium length scale of dynamically heterogeneous melting. If we wait for the system to start to relax after heating, we can see from Fig. 6.4(f) that the heterogeneity in dynamics quickly decreases as the sample transforms into a high temperature liquid. For a given value of f, S_4 also grows as T is decreased. As T is lowered, the initial barriers to relaxation are expected to increase at least exponentially, and we expect that this further accentuates the tendency for transformation to the liquid to occur in a nucleated manner.

6.2.4 Melting Fronts

One of the most interesting aspects of the behavior of USGs is the dynamics of melting that is initiated from an interface which is situated adjacent to a normal liquid [184, 185]. Here we investigate this behavior in PGs. To do this, we pin a percentage f of particles only in a rectangular subset of our system, producing an interface with an unpinned glass. We then monitor the overlap per particle averaged over vertical stripes in the system, commensurate with the symmetry of the interface, $\langle q_j(t, 0) \rangle_y$. Fig. 6.5(a-d) demonstrates that the melting

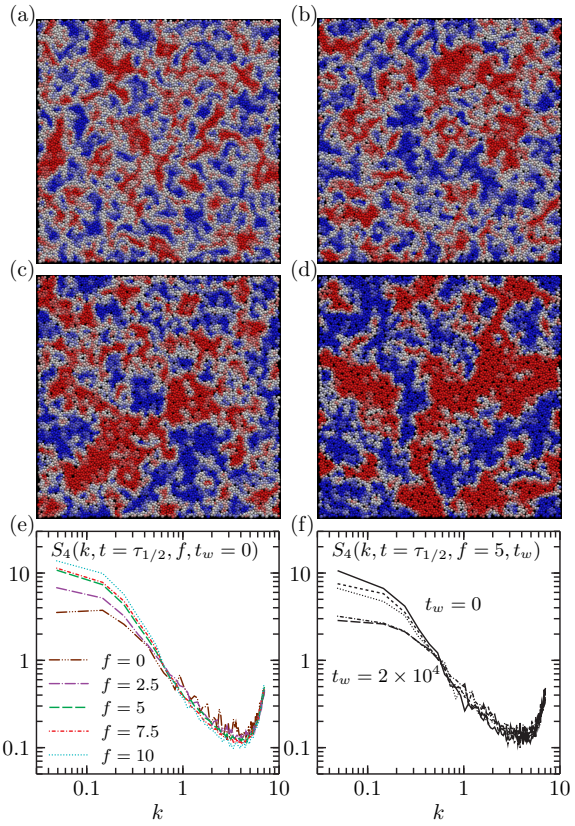

Figure 6.4: (a-d) Four representative snapshots of melting of pinned glasses with $T = 0.9$ for times where $\langle \tilde{q}_j(t, 0) \rangle = 0.5$. Each particle is colored by the value of $q_j(t, 0)$ averaged in a disc of radius 1.5, with overlap ranging from blue for $q_j = 1$ to red with $q_j = 0$. Values of f are $0, 2.5, 5$, and 10 from a-d, respectively. (e) Dynamical structure factor increases and becomes longer ranged in space with increasing f. (f) Dynamical structure factor decreases and becomes shorter ranged after waiting time t_w.

first occurs in the unpinned region. Clearly the interface between frozen and melted sections of the sample propagates from the unpinned region into the pinned sample. Example slices are shown in Fig. 6.5(e), in the manner of Ref. [175]. We define a critical melting value of $\langle q_j(t,0)\rangle_y = 0.2$, approximately the border between the red and white regions in Fig. 6.5(a-d). We then define a melting *front* by positions in the sample where $\langle q_j(t,0)\rangle_y$ goes from above 0.2 to below 0.2 precisely twice.

By fitting the average growth position for a given (T, f) to a linear function $x_{\text{front}} = x_0 + v_{\text{melt}}t$ we can extract melting velocities v_{melt}, shown with open symbols for four values of f in Fig. 6.5(f). At higher temperatures, it was not possible to satisfy our definition of the melting front for a time range sufficient to extract a melting velocity. This is exemplified in Fig. 6.5(a), where at $\log_{10}(t) \approx 3.2$, the sample has fully melted at a position far from the interface, indicating that the time scale for the bulk relaxation is shorter than the time taken for the front to propagate over the relevant distance. We find that v_{melt} is proportional to τ_α^{-1} (see Fig. 6.5(f)) suggesting that the same relaxation mechanisms that govern melting front propagation allow for density relaxation in the pinned bulk.

We suggest that the maximum length scale over which melting can be observed is given by $\xi^{\text{max}}_{\text{melt}} \approx v_{\text{melt}}\tau_s$. The competition of timescales directly visualized here suggests a consequence for experiments on the melting of USGs. For these samples, *transformation* length scales on the order of microns have been observed [183]. We suggest this can be understood using a simple heuristic, $\xi^{\text{max}}_{\text{trans}} = v_{\text{trans}}t_{\text{trans}}$. Clearly,

$$\xi^{\text{max}}_{\text{trans}} = [v_{\text{trans}}\tau_\alpha][t_{\text{trans}}/\tau_{alpha}] \tag{6.4}$$

$$= [\xi_{\text{decouple}}][\text{Stability Ratio}] \tag{6.5}$$

Since the stability ratios observed for USGs can be on the order of 10^5, a reasonable assumption of molecular dimensions for this decoupling length, as we find for $v_{\text{melt}}\tau_\alpha$, results immediately in a transformation length scale on the order of microns. Hence this seemingly massive transformation length scale is not a distinct property of USGs, but rather directly equivalent to their previously determined ultra-slow melting behavior.

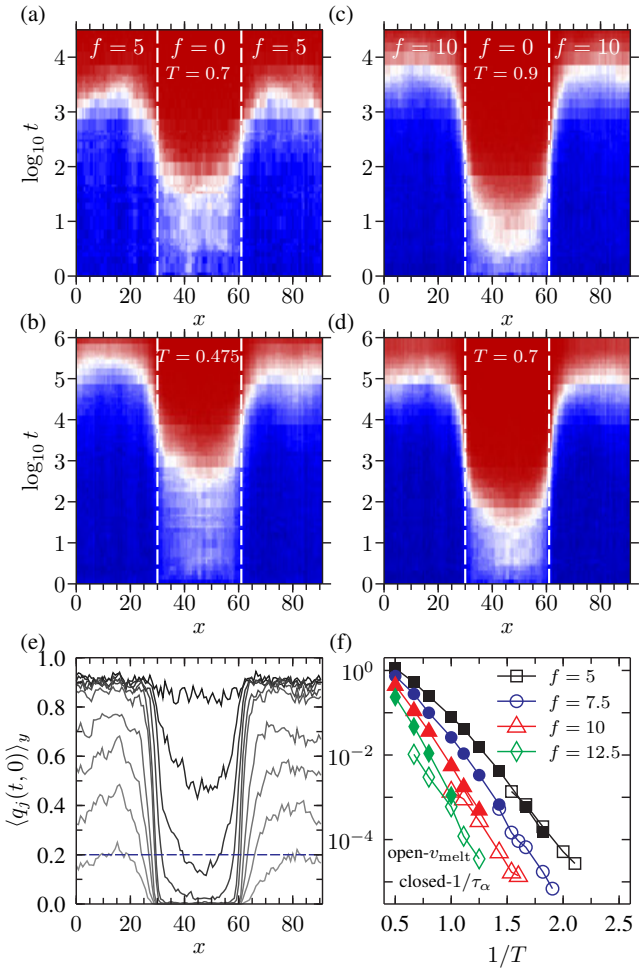

Figure 6.5: (a-d) Melting front profiles for systems with $f = 5$ (a,b) or $f = 10$ (c,d) for a volume to the left and right of the vertical dashed lines. The samples are heated to T and the overlap $q_j(t, 0)$ is averaged over slices of width 0.8 at each time in the simulation. Colors are the same as in Fig. 6.4. (e) Time slices for the data in panel (d) from short time (dark gray) to long time (light gray). A melting front is defined where the horizontal dashed line crossed a gray line exactly twice. (f) Melting velocities defined in text for three pinning fractions are compared to the equilibrium relaxation times as defined in the text and pictured in Fig. 6.2(c).

6.3 Discussion

We have shown that the random pinning of particles in a two-dimensional model supercooled liquid produces highly stable *in silico* glasses termed "pinned glasses" (PGs). PGs are in many ways analogous to USGs as we have demonstrated in this Chapter. The main difference is that PGs are formed *in equilibrium*. This is a unique feature that distinguishes PGs from USGs previously studied. Further distinctions are primarily due to differences in the melted state, which still contains pinned particles. For example, we have not observed "stability ratios", $t_{\rm trans}/\tau_\alpha$, above 10^3 while for USGs produced by vapor deposition, values of 10^5 have been measured. Although we do not discount the possibility that this ratio could grow to be much larger for T values below those we were able to study due to the difference in fragility as a function of f at $T_i = 0.425$ and $T > T_i$ [124, 181], we believe we have already demonstrated that PGs provide a simple conceptual framework that allows for the ability to understand many striking features found in USGs.

6.4 Methods

The Kob-Andersen Lennard-Jones system is a binary system of particles with pairwise Lennard-Jones interactions, such that particles i and j separated by a distance r_{ij} interact with the potential $V(r_{ij}) = \epsilon_{\alpha\beta}\left((\sigma_{\alpha\beta}/r_{ij})^{12} - (\sigma_{\alpha\beta}/r_{ij})^{6}\right)$, where α and β represent the particle type, A or B for particle i and j respectively. Interaction parameters are given by $\epsilon_{AA} = 1$, $\epsilon_{AB} = \epsilon_{BA} = 1.5$, $\epsilon_{BB} = 0.5$, and $\sigma_{AA} = 1$, $\sigma_{AB} = \sigma_{BA} = 0.8$, $\sigma_{BB} = 0.88$ [36]. The interaction between particle types α and β is truncated and shifted up at distance $2.5\sigma_{\alpha\beta}$. All particles have equal mass m. Energies, distances, and times are reported in reduced units proportional to ϵ_{AA}, σ_{AA} and $\tau = \sqrt{m\sigma_{AA}^2/\epsilon_{AA}}$. In this Chapter, we study the 2D variant of the model, for which as 65:35 ratio of A to B particles was previously shown to be a robust model supercooled liquid, resistant to crystallization [98, 180]. We generated configurations using Molecular Dynamics at a series of decreasing temperatures following the procedure of Ref. [180] to generate configurations at density $\rho = 1.2$ with $N = 10000$ down to $T = 0.45$, and then generated configurations at $T = 0.425$ by running simulations on these configurations for an additional $1.25 \times 10^5\tau$ using an integration

time-step of $\mathrm{d}t = 0.005\tau$. In all cases, simulations were performed using LAMMPS [105], and the temperature was maintained using a Nosé-Hoover thermostat with a time constant of $100\mathrm{d}t$ [186].

We wished to perform simulations with a fraction $\tilde{f} = f/100$ of particles fixed in place in a "uniformly random" manner similar in spirit to Ref. [119] to avoid sampling problems arising from localized extra-slow dynamics due to clusters of pinned particles. In order to do this, we chose a minimum distance between pinned particles $d_{min}(\tilde{f})$ and then randomly picked a set of particles commensurate with this minimum pair difference. In practice, we were able to do this for the $\tilde{f}$ of interest by using $d_{\mathrm{min}}(\tilde{f}) = 0.85 d_{\mathrm{avg}}(\phi = 0.55)$, where $d_{avg}(\phi)$ is the diameter $\tilde{f}N$ particles would have if they were placed in the same box with packing fraction $\phi = \tilde{f}\rho\pi(d_{\mathrm{avg}}/2)^2$. In this way the radial distribution function for the pinned particles is similar to that of a simple liquid with packing fraction $\phi = 0.55$, which was chosen heuristically. The results presented in this Chapter robust to the specific choice here, or indeed if the particles to pin are chosen totally at random.

In order to perform the heating and cooling experiments shown in Fig. 6.1, twelve simulations were run for every value of f and γ, by choosing four sets of $\tilde{f}N$ random particles from three completely independent starting configurations. These configurations were heated from $T_i = 0.425$ to $T = 2.0$ with the thermostat temperature raised in a linear fashion at a rate γ. The samples were subsequently cooled back to $T = 0.425$ and reheated to $T = 2.0$, also at a rate γ. For other data in this Chapter, the thermostat temperature was instantly raised to a "melting temperature" T. For any data point or curve shown here, at least 8 simulations were performed, with 4-6 independent configurations using 2-5 sets of randomly pinned particles. The simulation temperature stabilized at T by $1000\mathrm{d}t$, or 10 times the thermostat relaxation time. For all of these simulations, the simulation integration time-step was kept at $\mathrm{d}t = 0.005$ without any adverse consequences.

6.5 Acknowledgments

I thank Mark Ediger, Shakeel Dalal, and Giulio Biroli for stimulating conversations. LAMMPS simulations were executed and organized using the Swift parallel scripting language (NSF Grant No. OCI-1148443) [64] and were executed in part on resources provided by the University of Chicago Research Computing Center and on resources at the Texas Advanced

Computing Center (TACC) provided through the Extreme Science and Engineering Discovery Environment (XSEDE), supported by NSF Grant No. ACI-1053575.

Bibliography

[1] M. D. Ediger, C. A. Angell, and S. R. Nagel, J. Phys. Chem. **100**, 13200 (1996).

[2] L. Berthier and G. Biroli, Rev. Mod. Phys. **83**, 587 (2011).

[3] W. Kob, J. Phys. Condens. Matter **11**, R85 (1999).

[4] M. D. Ediger, Annu. Rev. Phys. Chem. **51**, 99 (2000).

[5] W. Kob, arXiv:cond-mat/0212344 (2002).

[6] A. Cavagna, Phys. Rep. **476**, 51 (2009).

[7] V. Lubchenko and P. G. Wolynes, Annu. Rev. Phys. Chem. **58**, 235 (2007).

[8] L. Berthier, G. Biroli, J.-P. Bouchaud, L. Cipelletti, and W. van Saarloos, *Dynamical heterogeneities in glasses, colloids, and granular media* (Oxford University Press, 2011).

[9] K. Binder and W. Kob, *Glassy materials and disordered solids: An introduction to their statistical mechanics* (World Scientific, 2011).

[10] P. G. Wolynes and V. Lubchenko, *Structural Glasses and Supercooled Liquids: Theory, Experiment, and Applications* (John Wiley & Sons, 2012).

[11] C. A. Angell, Science **267**, 1924 (1995).

[12] J. H. Gibbs and E. A. DiMarzio, J. Chem. Phys. **28**, 373 (1958).

[13] G. Adam and J. H. Gibbs, J. Chem. Phys. **43**, 139 (1965).

[14] M. Goldstein, J. Chem. Phys. **51**, 3728 (1969).

[15] W. Götze, J. Phys: Cond. Mat. **11**, A1 (1999).

[16] D. R. Reichman and P. Charbonneau, J. Stat. Mech.: Theor. Exp. **2005**, P05013 (2005).

[17] J. P. Garrahan, P. Sollich, and C. Toninelli, Dynamical Heterogeneities in Glasses, Colloids, and Granular Media **150**, 111 (2011).

[18] J. Garrahan and D. Chandler, Proc. Natl. Acad. Sci. **100**, 9710 (2003).

[19] A. S. Keys, L. O. Hedges, J. P. Garrahan, S. C. Glotzer, and D. Chandler, Phys. Rev. X **1**, 021013 (2011).

[20] Y. S. Elmatad, D. Chandler, and J. P. Garrahan, J. Phys. Chem. B **113**, 5563 (2009).

[21] A. S. Keys, J. P. Garrahan, and D. Chandler, Proc. Natl. Acad. Sci. **110**, 4482 (2013).

[22] B. W. H. Van Beest, G. J. Kramer, and R. A. Van Santen, Phys. Rev. Lett. **64**, 1955 (1990).

[23] S. A. Mackowiak, L. M. Leone, and L. J. Kaufman, Phys. Chem. Chem. Phys. **13**, 1786 (2011).

[24] L. M. Leone and L. J. Kaufman, J. Chem. Phys. **138**, 12A524 (2013).

[25] D. Frenkel and B. Smit, *Understanding molecular simulation: from algorithms to applications* (Academic Press, 2001).

[26] M. Tuckerman, *Statistical Mechanics and Molecular Simulations* (Oxford University Press, 2008).

[27] M. P. Allen and D. J. Tildesley, *Computer simulation of liquids* (Oxford university Press, 1989).

[28] M. E. J. Newman and G. T. Barkema, *Monte Carlo methods in statistical physics* (Oxford University Press, 1999).

[29] N. Metropolis, A. W. Rosenbluth, M. N. Rosenbluth, A. H. Teller, and E. Teller, J. Chem. Phys. **21**, 1087 (1953).

[30] B. J. Alder and T. E. Wainwright, J. Chem. Phys. **27**, 1208 (1957).

[31] G. D. Harp and B. J. Berne, J. Chem. Phys. **49**, 1249 (1968).

[32] D. Frenkel and J. McTague, Annu. Rev. Phys. Chem. **31**, 491 (1980).

[33] L. Berthier and W. Kob, J. Phys: Cond. Mat. **19**, 205130 (2007).

[34] J.-P. Hansen and I. R. McDonald, *Theory of simple liquids* (Academic Press, 2006).

[35] U. Balucani and M. Zoppi, *Dynamics of the Liquid State* (Clarendon Press, Oxford, 1994).

[36] W. Kob and H. C. Andersen, Phys. Rev. Lett. **73**, 1376 (1994).

[37] G. Biroli, J. Bouchaud, A. Cavagna, T. S. Grigera, and P. Verrocchio, Nature Phys. **4**, 771 (2008).

[38] U. R. Pedersen, T. B. Schrøder, and J. C. Dyre, Phys. Rev. Lett. **105**, 157801 (2010).

[39] J. D. Weeks, D. Chandler, and H. C. Andersen, J. Chem. Phys. **54**, 5237 (1971).

[40] C. S. OHern, S. A. Langer, A. J. Liu, and S. R. Nagel, Phys. Rev. Lett. **88**, 075507 (2002).

[41] G. Wahnström, Phys. Rev. A **44**, 3752 (1991).

[42] A. Ikeda and K. Miyazaki, J. Chem. Phys. **135**, 054901 (2011).

[43] S. Franz, C. Donati, G. Parisi, and S. C. Glotzer, Phil. Mag. B **79**, 1827 (1999).

[44] T. R. Kirkpatrick, D. Thirumalai, and P. G. Wolynes, Phys. Rev. A **40**, 1045 (1989).

[45] S. Franz and A. Montanari, J. Phys. A: Math. Theor. **40**, F251 (2007).

[46] D. Chandler and J. Garrahan, Annu. Rev. Phys. Chem. **61**, 191 (2010).

[47] R. Jack and J. Garrahan, J. Chem. Phys. **123**, 164508 (2005).

[48] J. Bouchaud and G. Biroli, J. Chem. Phys. **121**, 7347 (2004).

[49] S. Karmakar, C. Dasgupta, and S. Sastry, Proc. Natl. Acad. Sci. **106**, 3675 (2009).

[50] L. Berthier and W. Kob, Phys. Rev. E **85**, 011102 (2012).

[51] S. Karmakar, E. Lerner, and I. Procaccia, Physica A **391**, 1001 (2012).

[52] C. Cammarota and G. Biroli, Proc. Natl. Acad. Sci. **109**, 8850 (2012).

[53] B. Charbonneau, P. Charbonneau, and G. Tarjus, Phys. Rev. Lett. **108**, 035701 (2012).

[54] W. Kob and H. C. Andersen, Phys. Rev. E **51**, 4626 (1995).

[55] L. Berthier and G. Tarjus, Phys. Rev. Lett. **103**, 170601 (2009).

[56] L. Berthier and G. Tarjus, Euro. Phys. J. E **34**, 1 (2011).

[57] T. S. Grigera and G. Parisi, Phys. Rev. E **63**, 045102 (2001).

[58] A. Cavagna, T. S. Grigera, and P. Verrocchio, Phys. Rev. Lett. **98**, 187801 (2007).

[59] B. D. Lubachevsky and F. H. Stillinger, J. Stat. Phys. **60**, 561 (1990).

[60] D. Coslovich, Phys. Rev. E **83**, 051505 (2011).

[61] D. Alvarez, S. Franz, and F. Ritort, Phys. Rev. B **54**, 9756 (1996).

[62] M. A. Moore and J. Yeo, Phys. Rev. Lett. **96**, 95701 (2006).

[63] C. Cammarota, G. Biroli, M. Tarzia, and G. Tarjus, Phys. Rev. Lett. **106**, 115705 (2011).

[64] M. Wilde, M. Hategan, J. M. Wozniak, B. Clifford, D. S. Katz, and I. Foster, Parallel Computing **37**, 633 (2011).

[65] B. Efron and R. Tibshirani, *An introduction to the bootstrap*, Monographs on statistics and applied probability, Vol. 57 (Chapman & Hall/CRC, 1993).

[66] P. G. Debenedetti, F. H. Stillinger, *et al.*, Nature **410**, 259 (2001).

[67] A. J. Liu and S. R. Nagel, Nature **396**, 21 (1998).

[68] A. J. Liu and S. R. Nagel, Ann. Rev. Cond. Mat. Phys. **1**, 347 (2010).

[69] Z. Zhang, N. Xu, D. T. N. Chen, P. Yunker, A. M. Alsayed, K. B. Aptowicz, P. Habdas, A. J. Liu, S. R. Nagel, and A. G. Yodh, Nature **459**, 230 (2009).

[70] T. K. Haxton, M. Schmiedeberg, and A. J. Liu, Phys. Rev. E. **83**, 031503 (2011).

[71] A. Ikeda, L. Berthier, and P. Sollich, Phys. Rev. Lett. **109**, 018301 (2012).

[72] O. Dauchot, G. Marty, and G. Biroli, Phys. Rev. Lett. **95**, 265701 (2005).

[73] A. S. Keys, A. R. Abate, S. C. Glotzer, and D. J. Durian, Nature Phys. **3**, 260 (2007).

[74] O. Dauchot, D. J. Durian, and M. van Hecke, in *Dynamical Heterogeneities in Glasses, Colloids, and Granular Media* (Oxford University Press, 2011) pp. 110–151.

[75] L. Silbert, A. Liu, and S. Nagel, Phys. Rev. Lett. **95**, 098301 (2005).

[76] N. Xu, M. Wyart, A. J. Liu, and S. R. Nagel, Phys. Rev. Lett. **98**, 175502 (2007).

[77] N. Xu, V. Vitelli, M. Wyart, A. J. Liu, and S. R. Nagel, Phys. Rev. Lett. **102**, 038001 (2009).

[78] C. P. Goodrich, A. J. Liu, and S. R. Nagel, Phys. Rev. Lett. **109**, 095704 (2012).

[79] H. R. Schober and B. B. Laird, Phys. Rev. B **44**, 6746 (1991).

[80] B. B. Laird and H. R. Schober, Phys. Rev. Lett. **66**, 636 (1991).

[81] G. Biroli, J. P. Bouchaud, K. Miyazaki, and D. R. Reichman, Phys. Rev. Lett. **97**, 195701 (2006).

[82] F. Krzakala and J. Kurchan, Phys. Rev. E **76**, 021122 (2007).

[83] J. Kurchan and L. Laloux, J. Phys. A: Math. Gen **29**, 1929 (1996).

[84] C. Brito and M. Wyart, Euro. Phys. Lett. **76**, 149 (2006).

[85] C. Brito and M. Wyart, J. Chem. Phys. **131**, 024504 (2009).

[86] A. Widmer-Cooper, P. Harrowell, and H. Fynewever, Phys. Rev. Lett. **93**, 135701 (2004).

[87] A. Widmer-Cooper and P. Harrowell, J. Phys: Cond. Mat. **17**, S4025 (2005).

[88] A. Widmer-Cooper and P. Harrowell, Phys. Rev. Lett. **96**, 185701 (2006).

[89] A. Widmer-Cooper, H. Perry, P. Harrowell, and D. R. Reichman, Nature Phys. **4**, 711 (2008).

[90] A. Widmer-Cooper, H. Perry, P. Harrowell, and D. R. Reichman, J. Chem. Phys. **131**, 194508 (2009).

[91] R. Candelier, A. Widmer-Cooper, J. K. Kummerfeld, O. Dauchot, G. Biroli, P. Harrowell, and D. R. Reichman, Phys. Rev. Lett. **105**, 135702 (2010).

[92] N. Xu, V. Vitelli, A. J. Liu, and S. R. Nagel, Euro. Phys. Lett. **90**, 56001 (2010).

[93] C. Brito, O. Dauchot, G. Biroli, and J. P. Bouchaud, Soft Matter **6**, 3013 (2010).

[94] A. Ghosh, V. Chikkadi, P. Schall, J. Kurchan, and D. Bonn, Phys. Rev. Lett. **104**, 248305 (2010).

[95] K. Chen, W. G. Ellenbroek, Z. Zhang, D. T. N. Chen, P. J. Yunker, S. Henkes, C. Brito, O. Dauchot, W. van Saarloos, A. J. Liu, and A. G. Yodh, Phys. Rev. Lett. **105**, 025501 (2010).

[96] K. Chen, M. L. Manning, P. J. Yunker, W. G. Ellenbroek, Z. Zhang, A. J. Liu, and A. G. Yodh, Phys. Rev. Lett. **107**, 108301 (2011).

[97] C. Brito and M. Wyart, J. Stat. Mech. Theor. Exp. **2007**, L08003 (2007).

[98] R. Brüning, D. A. St-Onge, S. Patterson, and W. Kob, J. Phys. Cond. Mat. **21**, 035117 (2009).

[99] S. Karmakar and I. Procaccia, Phys. Rev. E **86**, 061502 (2012).

[100] F. H. Stillinger and T. A. Weber, Phys. Rev. A **25**, 978 (1982).

[101] T. A. Weber and F. H. Stillinger, J. Chem. Phys. **81**, 5089 (1984).

[102] T. A. Weber and F. H. Stillinger, Phys. Rev. B **31**, 1954 (1985).

[103] S. Sastry, P. G. Debenedetti, and F. H. Stillinger, Nature **393**, 554 (1998).

[104] T. B. Schrøder, S. Sastry, J. C. Dyre, and S. C. Glotzer, J. Chem. Phys. **112**, 9834 (2000).

[105] S. Plimpton, J. Comp. Phys. **117**, 1 (1995).

[106] B. Doliwa and A. Heuer, Phys. Rev. E **67**, 030501 (2003).

[107] B. Doliwa and A. Heuer, Phys. Rev. E **67**, 031506 (2003).

[108] R. A. Denny, D. R. Reichman, and J. P. Bouchaud, Phys. Rev. Lett. **90**, 025503 (2003).

[109] R. Mari, F. Krzakala, and J. Kurchan, Phys. Rev. Lett. **103**, 025701 (2009).

[110] G. Parisi and F. Zamponi, Rev. Mod. Phys. **82**, 789 (2010).

[111] D. J. Ashton and J. P. Garrahan, Euro. Phys. J. E **30**, 303 (2009).

[112] K. Kim, K. Miyazaki, and S. Saito, Euro. Phys. Lett. **88**, 36002 (2009).

[113] W. Kob, S. Roldán-Vargas, and L. Berthier, Nature Phys. **8**, 164 (2012).

[114] R. L. Jack and L. Berthier, Phys. Rev. E **85**, 021120 (2012).

[115] S. Karmakar, E. Lerner, and I. Procaccia, Physica A **391**, 1001 (2012).

[116] L. Berthier and W. Kob, Phys. Rev. E **85**, 011102 (2012).

[117] G. M. Hocky, T. E. Markland, and D. R. Reichman, Phys. Rev. Let. **108**, 225506 (2012).

[118] P. Charbonneau and G. Tarjus, Phys. Rev. E **87**, 042305 (2013).

[119] W. Kob and L. Berthier, Phys. Rev. Lett. **110**, 245702 (2013).

[120] R. L. Jack and C. J. Fullerton, Phys. Rev. E **88**, 042304 (2013).

[121] P. Scheidler, W. Kob, and K. Binder, Europhys. Lett. **59**, 701 (2002).

[122] K. Kim, Euro. Phys. Lett. **61**, 790 (2003).

[123] W. Kob, S. Roldan-Vargas, and L. Berthier, Physics Procedia **34**, 70 (2012).

[124] W. Kob and D. Coslovich, arXiv:1403.3519 (2014).

[125] J. D. Stevenson, J. Schmalian, and P. G. Wolynes, Nature Phys. **2**, 268 (2006).

[126] L. Berthier, G. Biroli, J. P. Bouchaud, W. Kob, K. Miyazaki, and D. R. Reichman, J. Chem. Phys. **126**, 184503 (2007).

[127] K. Kim, S. Saito, K. Miyazaki, G. Biroli, and D. R. Reichman, J. Phys. Chem. B **117**, 13259 (2013).

[128] L. Berthier, G. Biroli, D. Coslovich, W. Kob, and C. Toninelli, Phys. Rev. E **86**, 031502 (2012).

[129] E. Flenner and G. Szamel, J. Chem. Phys. **138**, 12A523 (2013).

[130] W. Kob and H. C. Andersen, Phys. Rev. E **51**, 4626 (1995).

[131] L. Berthier and G. Tarjus, Phys. Rev. E **82**, 031502 (2010).

[132] L. Berthier and T. A. Witten, Europhys. Lett. **86**, 10001 (2009).

[133] E. Flenner, H. Staley, and G. Szamel, Phys. Rev. Lett. **112**, 097801 (2014).

[134] P. Scheidler, W. Kob, and K. Binder, J. Phys. Chem. B **108**, 6673 (2004).

[135] D. Coslovich and W. Kob, to be published (2014).

[136] E. Flenner and G. Szamel, Nature Phys. **8**, 696 (2012).

[137] W. Kob, S. Roldán-Vargas, and L. Berthier, Nature Phys. **8**, 697 (2012).

[138] L. Berthier, G. Biroli, J.-P. Bouchaud, L. Cipelletti, D. El Masri, D. L'Hôte, F. Ladieu, and M. Pierno, Science **310**, 1797 (2005).

[139] A. Widmer-Cooper and P. Harrowell, J. Non-Cryst. Solids **352**, 5098 (2006).

[140] D. Coslovich and G. Pastore, Europhys. Lett. **75**, 784 (2006).

[141] F. C. Frank, Proc. R. Soc. Lond., A **215**, 43 (1952).

[142] P. J. Steinhardt, D. R. Nelson, and M. Ronchetti, Phys. Rev. Lett. **47**, 1297 (1981).

[143] D. R. Nelson, *Defects and geometry in condensed matter physics* (Cambridge University Press, 2002).

[144] D. Kivelson, S. A. Kivelson, X. Zhao, Z. Nussinov, and G. Tarjus, Physica A **219**, 27 (1995).

[145] D. Coslovich and G. Pastore, J. Chem. Phys. **127** (2007).

[146] J. Ding, Y.-Q. Cheng, H. Sheng, and E. Ma, Phys. Rev. B **85**, 060201 (2012).

[147] H. Tanaka, T. Kawasaki, H. Shintani, and K. Watanabe, Nat Mater **9**, 324331 (2010).

[148] A. Malins, J. Eggers, C. P. Royall, S. R. Williams, and H. Tanaka, J. Chem. Phys. **138**, 12A535 (2013).

[149] B. Charbonneau, P. Charbonneau, and G. Tarjus, Phys. Rev. Lett. **108**, 035701 (2012).

[150] G. Biroli, S. Karmakar, and I. Procaccia, Phys. Rev. Lett. **111**, 165701 (2013).

[151] S. Karmakar, C. Dasgupta, and S. Sastry, Annu. Rev. Condens. Matter Phys **5** (2014).

[152] P. Ronhovde, S. Chakrabarty, D. Hu, M. Sahu, K. Sahu, K. Kelton, N. Mauro, and Z. Nussinov, Eur. Phys. J. E **34**, 1 (2011).

[153] F. Sausset and D. Levine, Phys. Rev. Lett. **107**, 045501 (2011).

[154] C. Sammut and G. I. Webb, *Encyclopedia of machine learning* (Springer-Verlag, 2011).

[155] H. Tanaka, Eur. Phys. J. E **35**, 1 (2012).

[156] J. S. Langer, Phys. Rev. E **88**, 012122 (2013).

[157] W. Kob, S. Roldán-Vargas, and L. Berthier, Nature Phys. **8**, 164 (2011).

[158] T. B. Schrder, S. Sastry, J. C. Dyre, and S. C. Glotzer, J. Chem. Phys. **112**, 98349840 (2000).

[159] A. Ikeda and K. Miyazaki, Phys. Rev. Lett. **106**, 015701 (2011).

[160] L. Berthier and R. L. Jack, Phys. Rev. E **76**, 041509 (2007).

[161] S. Franz, G. Parisi, F. Ricci-Tersenghi, and T. Rizzo, Eur. Phys. J. E **34**, 1 (2011).

[162] C. S. OHern, S. A. Langer, A. J. Liu, and S. R. Nagel, Phys. Rev. Lett. **88**, 075507 (2002).

[163] F. H. Stillinger, J. Chem. Phys. **65**, 39683974 (1976).

[164] A. Lang, C. N. Likos, M. Watzlawek, and H. Lowen, J. Phys.: Condens. Matter **12**, 50875108 (2000).

[165] M. Tanemura, Y. Hiwatari, H. Matsuda, T. Ogawa, N. Ogita, and A. Ueda, Prog. Theor. Phys. **58**, 1079 (1977).

[166] G. Biroli and J.-P. Bouchaud, J. Phys: Cond. Mat. **19**, 205101 (2007).

[167] J. D. Eaves and D. R. Reichman, Proc. Natl. Acad. Sci. **106**, 15171 (2009).

[168] P. Charbonneau, A. Ikeda, J. A. van Meel, and K. Miyazaki, Phys. Rev. E **81**, 040501 (2010).

[169] B. Charbonneau, P. Charbonneau, Y. Jin, G. Parisi, and F. Zamponi, J. Chem. Phys. **139**, 164502 (2013).

[170] K. Kim and S. Saito, J. Chem. Phys. **138**, 12A506 (2013).

[171] S. F. Swallen, K. L. Kearns, M. K. Mapes, Y. S. Kim, R. J. McMahon, M. D. Ediger, T. Wu, L. Yu, and S. Satija, Science **315**, 353 (2007).

[172] S. S. Dalal and M. D. Ediger, J. Phys. Chem. Lett. **3**, 1229 (2012).

[173] M. D. Ediger and P. Harrowell, J. Chem. Phys. **137**, 080901 (2012).

[174] J. D. Stevenson and P. G. Wolynes, J. Chem. Phys. **129**, 234514 (2008).

[175] S. Léonard and P. Harrowell, J. Chem. Phys. **133**, 244502 (2010).

[176] S. Singh, M. Ediger, and J. J. de Pablo, Nature Mater. **12**, 139 (2013).

[177] I. Lyubimov, M. D. Ediger, and J. J. de Pablo, J. Chem. Phys. **139**, 144505 (2013).

[178] R. L. Jack, L. O. Hedges, J. P. Garrahan, and D. Chandler, Phys. Rev. Lett. **107**, 275702 (2011).

[179] T. Speck, A. Malins, and C. P. Royall, Phys. Rev. Lett. **109**, 195703 (2012).

[180] G. M. Hocky and D. R. Reichman, J. Chem. Phys. **138**, 12A537 (2013).

[181] S. Chakrabarty, S. Karmakar, and C. Dasgupta, arXiv:1404.2701 (2014).

[182] K. Dawson, L. A. Kopff, L. Zhu, R. J. McMahon, L. Yu, R. Richert, and M. Ediger, J. Chem. Phys. **136**, 094505 (2012).

[183] A. Sepúlveda, M. Tylinski, A. Giuseppi-Elie, R. Richert, and M. D. Ediger, to be published (2014).

[184] A. Sepúlveda, S. F. Swallen, L. A. Kopff, R. J. McMahon, and M. Ediger, J. Chem. Phys. **137**, 204508 (2012).

[185] A. Sepúlveda, S. F. Swallen, and M. D. Ediger, J. Chem. Phys. **138**, 12A517 (2013).

[186] G. J. Martyna, M. L. Klein, and M. Tuckerman, J. Chem. Phys. **97**, 2635 (1992).